The CAFE experiment:
A joint seismic and MT investigation of the Cascadia subduction system

By

R Shane McGary

B.S., Texas A&M University, 2007

Submitted in partial fulfillment of the requirements for the degree of

Doctor of Philosophy

at the

MASSACHUSETTS INSTITUTE OF TECHNOLOGY

and the

WOODS HOLE OCEANOGRAPHIC INSTITUTION

February, 2013

Signature of Author

Joint Program in Geophysics
Massachusetts Institute of Technology
And Woods Hole Oceanographic Institution
(date of final thesis submission)

Certified by

Rob L. Evans
Thesis Supervisor

Accepted by

Rob L. Evans
Chair, Joint Committee for Geology & Geophysics
Woods Hole Oceanographic Institution

Abstract

In this thesis we present results from inversion of data using dense arrays of collocated seismic and magnetotelluric stations located in the Cascadia subduction zone region of central Washington. In the migrated seismic section, we clearly image the top of the slab and oceanic Moho, as well as a velocity increase corresponding to the eclogitization of the hydrated upper crust. A deeper velocity increase is interpreted as the eclogitization of metastable gabbros, assisted by fluids released from the dehydration of upper mantle chlorite. A low velocity feature interpreted as a fluid/melt phase is present above this transition. The serpentinized wedge and continental Moho are also imaged. The magnetotelluric image further constrains the fluid/melt features, showing a rising conductive feature that forms a column up to a conductor indicative of a magma chamber feeding Mt. Rainier. This feature also explains the disruption of the continental Moho found in the migrated image. Exploration of the assumption of smoothness implicit in the standard MT inversion provides tools that enable us to generate a more accurate MT model. This final MT model clearly demonstrates the link between slab derived fluids/melting and the Mt. Rainier magma chamber.

Acknowledgements

Funding for this work was made possible by the American Society for Engineering education through a National Defense Science and Engineering Fellowship, and by the National Science Foundation through two grants for the CAFE and CAFE MT projects.

I would also like to thank Ken Creager, Geoff Abers, Phil Wannamaker, Virginia Maris, Mike Brown, and Anna Kelbert for their part in the acquisition of data,

Fred Pearce and Chin-Wu Chen for their help with the seismic migration codes,

Anne Pommier for her help with connecting conductivity to petrology,

and Jimmy Elsenbeck for his assistance with the various MT codes.

I would also like to thank the members of my thesis committee, Dan Lizarralde, Alison Malcolm, Alison Shaw, and Horst Marschall, along with the chair of my thesis defense, Juan Pablo Canales.

Special thanks to my co-advisor, Stephane Rondenay, and my primary advisor Rob Evans, without whom none of this would have been possible.

And finally, special thanks to my wife Carrie and son Ian for their continued support throughout this process.

Table of Contents

1. Introduction

Many of the natural hazards associated with subduction zones are intimately tied to the release of fluids bound within the subducting slab. Intraslab earthquakes have been linked with a process in which fluids released during the transformation of hydrated metabasalts to eclogite in the upper crust increases pore pressure, thereby reactivating pre-existing faults (Kirby et al., 1996, Hacker et al., 2003b, Preston et al., 2003). Slow slip and low frequency tremor, which have been tentatively linked with the periodicity of great megathrust earthquakes (Mazzotti and Adams, 2004), can be explained by episodic buildup and release of fluid pore pressure across plate boundaries down-dip of the locked zone (Abers et al., 2009, Audet et al., 2010). Most arc magmas are also generally believed to be generated by flux melting that occurs when dehydration reactions in the oceanic crust and uppermost mantle release fluids into the continental asthenosphere (Ulmer and Trommsdorff, 1995, Kirby et al., 1996). Finally, density increases associated with dehydration have been linked with changes in slab dip and increased stresses within the slab (Klemd et al., 2011).

While recent investigations have dramatically improved our understanding of the distribution and cycling of fluids in subduction systems, many questions remain open. Advances in the understanding of the phase transformations that occur within the subducting lithosphere (Poli and Schmidt, 2002, Hacker et al., 2003a and references within, Hacker, 2008) have given us the tools to better interpret geophysical evidence. Improvements in the thermal modeling of subduction zones such as the use of olivine rheology in the mantle wedge (van Keken et al., 2002) and decoupling at the cold nose of the wedge (Wada and Wang, 2009) have aided in the development of a consistent set of thermal models for subduction systems worldwide (Syracuse et al., 2010). Application of the phase transformations along the P-T regimes predicted by the thermal models has made it possible to predict depth dependent fluid flux for the global suite of subduction zones (van Keken et al., 2011).

Cascadia is an attractive setting for studying the fluid distribution and dynamics in subduction zones for a variety of reasons. It has been thoroughly investigated using a variety of geological and geophysical methods over a number of decades, so much is known about both the surface geology and the structure of the subsurface. As the slab is young and hot, it is expected to release a significant fraction of its fluids in the forearc, suggesting that the evidence of fluids should be more pronounced here than they would be in a cooler setting.

Finally, the connection between these fluid processes and the associated tectonic and volcanic hazards that potentially threaten a number of densely populated areas underline the importance of understanding the subduction fluid cycle in Cascadia.

For all of these reasons, the Cascadia region has been the subject of extensive geophysical work. While much of the geophysical exploration of the region has involved seismology, the magnetotelluric method has also been employed to good effect. Magnetotellurics is attractive because while it is sensitive to a completely different set of rock properties than are seismic methods (Hellfrich, 2003, Jones et al., 2009), velocity and conductivity are often correlated (Stanley et al., 1990, Jones et al., 2009), either directly or simply in the fact that at distinct geological boundaries both parameters are likely to change (Gallardo, 2007, Moorkamp et al., 2007). It is therefore tempting to utilize both types of data in our interpretations, particularly where the data profiles are collocated (Gallardo and Meju, 2007).

While much work in the past has simply been a matter of questioning whether an interpretation of one type of data is consistent with a previous interpretation of a different type, there have been several recent efforts to combine two (or more) types of data on a more fundamental level. The rationale behind joint inversion of multiple data sets is to improve resolution, diminish the influence of noise, and reduce the inherent non-uniqueness by providing additional constraints (Gallardo, 2007, Moorkamp et al.,

2007). While the values of velocity and resistivity have been compiled for a wide range of geological and physical conditions (Hacker, 2003a, Jones et al., 2009), there exists no fundamental relationship between the two physical properties (Bedrosian et al., 2007). Still, as we stated above, the two properties do tend to be reasonably well correlated in the subsurface, and several different approaches to joint inversion of seismic and electromagnetic data have been attempted. Some of the techniques utilized to date include stochastic optimization methods such as genetic algorithms (Moorkamp et al., 2007), physical property gradient methods (often combined with structural constraints) such as the cross-gradient (Gallardo, 2007, Hu et al., 2008, Gallardo and Meju, 2007), and statistical correlation methods such as cluster analysis (Bedrosian et al., 2007, Munoz et al., 2010).

None of the joint inversion methods mentioned above address this particular combination of ideas in a completely satisfactory way. They all rely in some way on the natural relationship between the distribution of the resistivity and velocity values. The distribution of resistivity values near sharp boundaries in the MT inversion is smoothed by design (which directly impacts the gradient as well), creating an artificial difference that the joint inversions would attempt to resolve as a natural phenomenon.

A different way to look at the use of multiple data sets is to attempt to use the strengths of one technique to mitigate weaknesses inherent in another. For example, the magnetotelluric technique typically employs a smoothness constraint to control the

resolution of structure to that required by the data. Of course, sharp boundaries exist in the subsurface, and these are often not well resolved by the method. This suggests that we might attempt to combine MT with a method that is well suited to illuminating sharp boundaries. Teleseismic migration is one particularly appealing candidate, involving backpropagation of a scattered wavefield to the scattering points in the subsurface (Rondenay, 2009), thereby highlighting the very boundaries we hope to resolve.

This is the approach we take in the current study, analyzing data collected at dense arrays of roughly collocated passive seismic and magnetotelluric stations. We analyze the two data sets independently, using Generalized Radon Transform (GRT) migration for the seismic data, and Non-Linear Conjugate Gradient (NLCG) inversion for the magnetotelluric data. We then perform the magnetotelluric inversion again, this time incorporating the a priori information obtained during the GRT migration into the inversion.

While there are valid reasons for searching for the smoothest resistivity model in the absence of a priori information, the presence of such information, particularly with respect to the location of sharp boundaries, warrants another approach. While inversion methods allow us to create models that fit the data as closely as desired, there is a tradeoff between resolving structure and generating false structure from noise that tips decidedly in favor of the latter as the misfit becomes small. For any reasonable

selection of misfit, there are an infinite number of solutions that fit the data equally well (Parker, 1994, Zhdanov, 1993). The selection of a specific model is necessarily a subjective process involving the incorporation of a priori information and/or assumptions about the nature of the distribution of the measured parameter in the subsurface.

The conventional way to think about such problems is as a minimization of the Tikhonov parametric functional (Tikhonov and Arsenin, 1977),

$$\mathbf{T(m)=\phi(m)+\lambda s(m)} \tag{1}$$

where **m** is a matrix representing a distribution of geophysical parameters within some space, $\mathbf{\phi(m)}$ is the misfit functional described by

$$\mathbf{\phi(m)=||Fm-d||^2} \tag{2}$$

where **d** is the observed data and **Fm** the data predicted by the model, and **s(m)** is a functional that represents assumptions or a priori information that the worker has chosen to include, with its relative importance determined by the regularization parameter $\boldsymbol{\lambda}$ (Tikhonov and Arsenin, 1977, Parker, 1994, Mehanee and Zhdanov, 2002).

Equations (1) and (2) offer at least three fundamental ways in which we might express a preference for one model over another. The first of these is simply to fix the value of the model parameter over some spatial distribution. For example, in coastal magnetotelluric surveys, it is standard practice to include in the model a fixed distribution of highly conductive cells to represent the ocean, thereby excluding all models that don't include a conductor where we know one to exist.

A second method is to include an additional parameter within the misfit functional, jointly inverting for two nominally independent data sets. The inclusion of a second set of data can improve resolution and reduce the impact of noise, thereby constraining the range of possible models (Gallardo, 2007). The set of models that explains two (or more) datasets to a given misfit is both smaller and more compelling than the set that explains one but not necessarily the other.

Finally, we can utilize the stabilizing functional **s(m)** to express preference for a given subset of models. While several stabilizing functions have been successfully used (least squares, minimum norm of the gradient, distance from an a priori model, etc.) in various geophysical applications (Smith et al., 1999, Mehanee and Zhdanov, 2002, de Groot-Hedlin and Constable, 2004), many magnetotelluric algorithms employ the minimum norm of the Laplacian, which will seek the smoothest model possible that fits the data (for a given misfit). The argument is that by seeking the smoothest model (again, for a sufficiently large misfit), only structure explicitly required by the data will

be resolved (de Groot-Hedlin and Constable, 1990). In nature, sharp geoelectric boundaries do of course exist, and smooth algorithms may not sufficiently resolve these boundaries (Smith et al., 1999, de Groot-Hedlin and Constable, 2004, Mehanee and Zhdanov, 2002).

In order to overcome these difficulties, several algorithms have been developed that allow for sharp boundaries by making different global assumptions about the distribution of the modeled parameter in the subsurface, for example by favoring models made up of layers (Smith et al., 1999, de Groot-Hedlin and Constable, 2004) or containing primarily blocky structure (Mehanee and Zhdanov, 2002). Of course, each of these global algorithms present trade-offs, and are effective largely to the extent that the underlying assumptions are accurate throughout the modeled space. While a priori knowledge regarding the location and nature of sharp discontinuities can be an extremely useful implement in resolving the associated structure (de Groot-Hedlin and Constable, 1990), its utility in resolving a sufficiently complicated subsurface is dependent on the extent to which it can be effectively applied locally.

Inversion packages such as WinGlink and Occam allow for the elimination of the penalty for roughness along presumed discontinuities (de Groot-Hedlin and Constable, 1990, Rodi and Mackie, 2001), and while this tool has been used to good effect (Matsuno et al., 2010), it is but a tentative first step in exploring the possibilities for spatially-dependent stabilizing functionals. While de Groot-Hedlin and Constable rightly point

out that one should use such tools cautiously as "incorrect placement of boundaries may produce misleading results", we must also recognize that their use is simply trading one set of assumptions for another and we should be cautious in any event.

Chapter 2 presents high resolution images from 2-D GRT migration of data collected from a dense array of 41 broadband seismometers located in a roughly east to west transect across central Washington State. We see a dipping low velocity layer that we interpret to be the descending oceanic crust, underlain by a positive velocity transition that we take to be the oceanic Moho. A fading velocity contrast suggests the transformation of hydrated basalt in the upper crust to eclogite, but also shows the retention of fluids to depths of 80 km or more. A low velocity feature above the slab is consistent with a fluid/melt phase released at depths of 80-100 km.

Previous GRT work conducted across Vancouver Island/British Columbia to the north and Oregon to the south allow us to make comparisons and investigate regional implications. Earthquake distribution combined with our results suggest that the fluid release at 80 km depth in central Washington is due to the dehydration of chlorite harzburgite in the uppermost mantle and subsequent transformation of lower crustal metastable gabbros to eclogite. The extent to which this occurs in central Washington appears to be unique for Cascadia.

Chapter 3 follows up with high resolution images generated from a non-linear conjugate gradients inversion of magnetotelluric data collected from 60 broadband and 20 long period stations along a line collocated with the seismic array. The down-going slab appears as a large resistive feature, though the surface is not very well defined. Likewise, there appear to be two rising conductive features, one rising from a depth of roughly 40 km that appears to be connected with the hydrated basalt to eclogite fluid release, and a second one starting deeper and to the east that rises upwards and seawards, collecting just below and to the west of Mt. Rainier.

The first part of Chapter 4 investigates the consequences of the standard inclusion of a smoothness parameter in the Tikhonov equation for magnetotelluric inversions. Through a series of models, we explore ways to better understand the impact of the smoothness assumption in various settings, and also methods to mitigate its impact. In the second part of Chapter 4 we apply those lessons to the Cascadia Array for Earthscope Magnetotelluric (CAFE MT) data set, incorporating the results of the seismic migration into the MT inversion sequence. We conclude by showing that the augmented model is more robust than the standard half-space models, and therefore provides stronger insight into the fluid processes of the Cascadia subduction zone in Washington.

References for Chapter 1

Abers, G.A., MacKenzie, L.S., Rondenay, S., Zhang, Z., Wech, A.G., Creager, K.C., 2009. Imaging the source region of Cascadia tremor and intermediate-depth earthquakes. Geology 37, 1119-1122.

Audet, P., Bostock, M.G., Boyarko, D.C., Brudzinski, M.R., Allen, R.M., 2010. Slab morphology in the Cascadia fore arc and its relation to episodic tremor and slip. J. Geophys. Res. 115, B00A16.

Bedrosian, P.A. et al., 2007. Lithology-derived structure classification from the joint interpretation of magnetotelluric and seismic models. Geophys. J. Int., 170, 737-748.

de Groot-Hedlin, C., and Constable, S., 1990. Occam's inversion to generate smooth, two-dimensional models from magnetotelluric data. Geophysics 55, 1613-1624.

de Groot-Hedlin, C. and Constable, S., 2004. Inversion of magnetotelluric data for 2D structure with sharp resistivity contrasts. Geophysics 69, 78-86.

Gallardo, L.A., 2007. Multiple cross-gradient joint inversion from geospectral imaging. Geophys. Res. Let., 34, L19301.

Gallardo L.A., and Meju, M.A., 2007. Joint two-dimensional cross-gradient imaging of magnetotelluric seismic traveltime data for structural and lithological classification. Geophys. J. Int, 169, 1261-1272.

Hacker, B.R., Abers, G.A., Peacock, S.M., 2003a. Subduction factory 1. Theoretical mineralogy, densities, seismic wave speeds, and H_2O contents. J. Geophys. Res. 108(B1), 2029, doi:10.1029/2001JB001127.

Hacker, B.R., Peacock, S.M., Abers, G.A., 2003b. Subduction factory 2. Are intermediate-depth earthquakes in subducting slabs linked to metamorphic dehydration reactions? J. Geophys. Res. 108(B1), 2030, doi:10.1029/2001JB001129.

Hacker, B. R., 2008. H2O subduction beyond arcs, Geochem. Geophys. Geosyst., 9, Q03001, doi:10.1029/2007GC001707.

Helffrich, George, 2003. Basic principles of electromagnetic and seismological investigation of shallow subduction zone structure. Inside the Subduction Factory, Geophysical Monograph 138, American Geophysical Union.

Hu, W. et al., 2008. Joint electromagnetic and seismic inversion using a structural constraint. Schlumberger-Doll Research.

Jones, A.G., et al., 2009. Velocity-conductivity relationshipes for mantle mineral assemblages in Archean cratonic lithosphere based on a review of laboratory data and Hashin-Shtrikman external bounds. Lithos 109, 131-143.

Kirby, S., Engdahl, E.R., Denlinger, R., 1996. Intermediate-depth intraslab earthquakes and arc volcanism as physical expressions of crustal and uppermost mantle metamorphism in subducting slabs, in Bebout, G., et al., eds., Subduction top to bottom: American Geophysical Union Geophysical Monograph 96, 195-214.

Klemd R., John, T., Scherer, E.E., Rondenay, S., Gao, J., 2011. Changes in dip of subducted slabs at depth: Petrological and geochronological evidence from HP-UHP rocks (Tianshan, NW-China). Earth Planet. Sci. Lett. 310, 9-20.

Matsuno, T., et al., 2010. Upper mantle electrical resistivity structure beneath the central Mariana subduction system, Geochem. Geophys. Geosyst., 11, Q09003, doi:10.1029/2010GC003101.

Mazzoti, S., and Adams, J., 2004. Variability of near-term probability for the next great earthquake on the Cascadia subduction zone. Bull. Seis. Soc. America, v. 94, 1954-1959.

Mehanee S. and Zhdanov, M., 2002. Two-dimensional magnetotelluric inversion of blocky geoelectrical structures. J. Geophys. Res. 107, B4.

Moorkamp, M., et al., 2007. Joint inversion of teleseismic receiver functions and magnetotelluric data using a genetic algorithm: Are seismic velocities and electrical conductivities compatible? Geophys. Res. Lett., 34, L16311.

Munoz, G., et al., 2010. Exploring the Gross Schonebeck (Germany) geothermal site using a statistical joint interpretation of magnetotelluric and seismic tomography models. Geothermics.

Parker, R.L., 1994 Geophysical Inverse Theory. Princeton University Press (BOOK)

Poli, S., Schmidt, M.W., 2002. Petrology of subducted slabs. Annu. Rev. Earth Planet. Sci. 30, 207-235.

Preston, L.A., Creager, K.C., Crosson, R.S., Brocher, T.M., Trehu, A.M., 2003. Intraslab earthquakes: Dehydration of the Cascadia Slab. Science 302, 1197-2000.

Rodi, William, and Mackie, Randall L., 2001. Nonlinear conjugate gradients algorithm for 2-D magnetotelluric inversion. Geophysics, 66, 174-187.

Rondenay, S., 2009. Upper mantle imaging with array recordings of converted and scattered teleseismic waves. Surv. Geophys. 30, 377-405.

Smith, J.T., et al., 1999. Sharp boundary inversion of 2D magnetotelluric data. Geophysical Prospecting, 47, 469-486.

Stanley, William D. et al., 1990. Deep Crustal Structure of the Cascade Range and Surrounding Regions from Seismic Refraction and Magnetotelluric Data. Journal of Geophysical Research, 95, B12, 19419-19438.

Syracuse, E.M., van Keken, P.E., Abers, G.A., 2010. The global range of subduction zone thermal models. Phys. Earth Planet. Interiors 183, 73-90.

Tikhonov, A.N., and Arsenin V.Y., 1977. Solutions of ill-posed problems, John Wiley Publishing, New York. (BOOK)

Ulmer P., Trommsdorff, V., 1995. Serpentine stability to mantle depths and subduction related magmatism. Science 268, 858-861.

van Keken, P.E., Hacker, B.R., Syracuse, E.M., and Abers, G.A., 2011. Subduction factory: 4. Depth-dependent flux of H_2O from subducting slabs worldwide. J. Geophys. Res. 116, B01401.

Wada, I., Wang, K., He, J., Hyndman, R.D., 2008. Weakening of the subduction interface and its effects on surface heat flow, slab dehydration, and mantle wedge serpentinization. J. Geophys. Res. 113, B04402.

Zhdanov, M.S., 1993. Tutorial: Regularization in Inversion Theory. Center for Wave Phenomena, Colorado School of Mines.

2. Imaging the transition of metastable gabbro to eclogite in the Cascadia subduction system

R Shane McGary (1,2), Stephane Rondenay (3), Geoffrey Abers (4), Kenneth Creager (5)

1. Massachusetts Institute of Technology
2. Woods Hole Oceanographic Institution
3. University of Bergen
4. Lamont-Doherty Earth Observatory
5. University of Washington

Abstract

In this paper we present high resolution seismic images from 2-D Generalized Radon Transform (GRT) migration of data from a dense array of broadband seismometers running west to east across central Washington State. We find a low velocity dipping layer consistent with the descending oceanic crust, as well as a roughly parallel transition to deeper high velocities representing the oceanic Moho. We clearly image a positive velocity gradient at a depth of approximately 40 km beneath the volcanic arc consistent with the continental Moho. A fading velocity contrast within the oceanic crust consistent with dehydration reactions starts at a depth of ~40 km, but low velocities within the crust persist to depths of at least 80 km and perhaps 100 km. A low velocity anomaly in the shallow mantle wedge suggests extensive serpentinization.

We are able to compare the results of this study with the previous GRT migration studies to the north and south. While the images are similar in many ways, some differences are quite striking. Specifically, the fading velocity contrast normally associated with dehydration reactions along the path towards eclogitization is less pronounced in the central Washington profile, despite presumably similar thermal profiles. Instead, much of the low velocity signature is retained to depths of more than 80 km. Additionally, we find a low velocity region above the slab at this depth, consistent with a significant fluid or melt pocket that is also not evident in the other profiles. We argue that for the central Washington line, hydrated minerals in the subducting upper mantle release fluids that accelerate the eclogitization of metastable gabbro in the lower crust, an interpretation that also might help explain the presence of volcanoes such as Mt. Rainier and Mt. Helens in the Cascades forearc.

1. Introduction

Slab derived fluids released in shallow to moderate (40-130 km) subduction zone settings play a critical role in the subduction process. The transformation of hydrated metabasalts to eclogite in the subducting oceanic crust has been linked to intraslab earthquakes (Hacker et al., 2003b), and the accompanying 12-15% increase in density may be associated with changes in slab dip (Klemd et al., 2011, Bostock et al., 2002) and increasing stresses within the slab (Kirby et al., 1996). A significant portion of the fluids released during these dehydration reactions typically make their way into the mantle wedge, lowering the melting temperature of the mantle rock and potentially resulting in partial melting and arc volcanism. The released fluids also drive hydration reactions such as

serpentinization in parts of the mantle wedge that are sufficiently cool. This reduces the mechanical strength of the boundary between the slab and wedge (Hyndman and Peacock, 2003), and can result in the creation of an aseismic region along the weakened interface as the seaward corner of the mantle wedge becomes decoupled from the descending slab (Wada et al., 2008, Furukawa, 1993).

It is generally recognized that earthquakes occurring at depths greater than 35 km in subduction settings are probably associated with a process in which internal pore pressure generated by fluids released during dehydration reactions reduces the effective normal stresses along pre-existing faults (Kirby and Wang, 2002, Hacker et al., 2003b). In Cascadia, fluid release from hydrated metabasalts during eclogitization reactions occurs at depths near ~35-45 km (Hacker et al., 2003a, van Keken et al., 2011, Bostock, 2012).

Dehydration of hydrated subducted oceanic mantle potentially provides an additional source of fluid release at moderate depths, generally occurring near the 600° C isotherm for antigorite and the 800° isotherm for chlorite (Schmidt and Poli, 1998, Ulmer and Trommsdorff, 1995) corresponding to depths of 60-70 km for the former and 85-95 km for the latter in Cascadia (van Keken et al., 2011). Serpentine rocks can form at the spreading ridge for slow-spreading and intermediate-spreading centers, and has been associated with the presence of a

well-developed axial valley (Cannat, 1993, Carbotte et al., 2006). Additionally, both the crust and upper mantle of the incoming oceanic plate can become hydrated during faulting associated with bending near the trench (Ranero et al., 2005, Key et al., 2012), or during the reactivation of spreading center derived faults (Nedimovic et al., 2008).

In this study, we employ a 2-D GRT migration of teleseismic data collected from a dense array of 41 seismometers over a period of ~27 months. We show high resolution images of the subsurface below central Washington, providing improved constraints on the dehydration and hydration reactions taking place within the Cascadia subduction zone.

2. Geological and Geophysical Background

2.1 The Cascadia Subduction System

The tectonics of the Pacific Northwest are dominated by the Cascadia subduction system. Beneath central Washington, the Juan de Fuca plate is subducting at a rate of approximately 35 mm/yr (Miller et al., 2001). The dip of the subducting plate is between 5-15° near the coast, steepening to ~ 40° after reaching a depth of 70-80 km (McCrory et al., 2006, Roth et al., 2008).

While smaller in magnitude than megathrust events, the impact of intraslab earthquakes should not be underestimated. Since 1945, there have been several events with magnitudes >5.5, including the 6.8 Nisqually earthquake in 2001 that resulted in an estimated monetary loss of more than USD two billion (Kirby and Wang, 2002). Most of these events have epicenters located between 35 and 70 km depth, with some small events reaching depths up to 100 km (Preston et al., 2003). Additionally, the Puget lowland region of central and northern Washington, which is a focus of this study, experiences a much higher incidence of these earthquakes than neighboring regions to the north and south.

The subduction zone also supports a chain of active volcanoes, extending from Mt. Meager in British Columbia to the Lassen region in California. While the majority of the Cascade volcanoes lie along the Quaternary axis, including those relevant to the previous studies in British Columbia and Oregon, two large volcanoes and two smaller vent fields lie well into the forearc, as much as 50 km to the west of the axis. One of these volcanoes, Mt. St. Helens, erupted catastrophically on May 18, 1980, resulting in 57 deaths and damages of more than USD one billion. The other, Mt. Rainier, is a primary target of this study.

2.2 Previous geophysical studies

The potential hazards and proximity to major urban centers has predictably led to extensive geophysical efforts directed towards a better understanding of the regional substructure and its dynamics. Regional P-wave tomographic studies have mapped the extent of the Juan de Fuca plate (Roth et al., 2008), and the velocity structure of the plate, megathrust, forearc crust, and upper mantle (Ramachandran et al., 2006), arguing that the intraslab earthquakes occurring at depths of 40-55 km depth are near the oceanic Moho. The descending slab has been imaged to depths of 350 km below Washington (Roth et al., 2008, Schmandt and Humphreys, 2010) but shows a weak or even non-existent signature below 160 km under much of Oregon (Schmandt and Humphreys, 2010).

Newer techniques such as ambient noise and multiple plane-wave surface wave tomography have also been used in isolation (Yang et al., 2008) or in conjunction with receiver functions (Gao et al., 2011) to map the S-velocity structure of the upper 75-150 km, with particular attention to mapping the continental Moho in the region. Receiver functions have also been utilized (Eagar et al., 2010) to map the deeper 410 and 660 km discontinuities throughout the Pacific Northwest.

Single station methods have been combined with GPS measurements to investigate episodic tremor and slip (ETS) (Rogers and Dragert, 2003, Brudzinski and Allen, 2007, 2010, Audet et al., 2010), establishing that the region can be

subdivided into three or more zones based on different recurrence intervals of these phenomena, with implications for stress buildup and megathrust earthquake periodicity.

Array migration methods have been previously employed in the region as well, including generalized radon transform (GRT) migration surveys to the north of the current study across Vancouver Island and into British Columbia (Nicholson et al., 2005), and to the south through central Oregon (Rondenay et al., 2001). A preliminary GRT study using a subset of the data used for the current work was also published (Abers et al., 2009), examining the relationship between ETS and a sharp velocity transition interpreted to be a layer of weak sediment or overpressured fault zone.

While tomographic methods are sensitive to volumetric changes in material properties, the strength of the GRT migration method is its sensitivity to abrupt velocity transitions (Rondenay, 2009), allowing it to be used effectively to constrain the boundaries along which such transitions occur, such as at the top of a subducting slab, or at the oceanic or continental Moho. Because dehydration and hydration reactions such as eclogitization, serpentinization, and serpentinite dehydration also have characteristic velocity changes associated with them (Hacker et al., 2003a), the boundaries of the regions within which these reactions

occur can also be constrained (Bostock et al., 2002), providing insight into the fluid processes taking place within the subduction setting.

3. Method

3.1 Generalized Radon Transform

In this study, we use a 2-D generalized radon transform (GRT) migration approach (Miller et al., 1987, Bostock et al., 2001) to produce a series of high-resolution seismic images across the Cascadia subduction zone. The specifics of this method have been described in detail in other papers (see, e.g. Bostock et al., 2001, Shragge et al., 2001, Rondenay et al., 2001, Rondenay, 2009), as have the associated assumptions, resolution and image robustness (Rondenay et al., 2005, Rondenay 2009), so we present here only a brief review of the main characteristics.

The principle behind migration is rooted in the idea that any point within the Earth at which scattering occurs can be identified by back-propagation to depth of the scattered wavefield recorded by a dense array of receivers at the surface, such that the transposed wavefield will highlight the sources of the seismic scattering in the subsurface. The Green's function of the scattered wavefield is

expressed as a volume integral, then simplified by assuming single scattering (Born approximation) and the high frequency ray approximation (Bostock and Rondenay, 1999). The method combines the stacking of the scattered wavefields along diffraction hyperbolae with an inversion/backprojection operator based on analogy with the generalized Radon Transform (Miller et al., 1987, Bostock et al., 2001).

In practice, the 2-D GRT inversion allows for the simultaneous treatment of five independent modes of scattering, the forward scattered PS mode, and four backscattered modes – PP, PS, SSh, and SSv. The travel paths for each of these modes are depicted in Fig. 1.

3.2 Preprocessing

Pre-processing of the data was accomplished through the application of the following series of steps (see, e.g., Rondenay et al., 2005).

1) Rotation and transformation of the waveforms into radial, transverse, and vertical components

2) Application of the inverse free surface transfer matrix to rotate the wavefield into the polarization directions of the incident P-wave and the corresponding S

waves (Sv and Sh), while suppressing the downgoing free-surface reflections (Kennett, 1991).

3) Alignment of the P traces using a multi-channel cross correlation (VanDecar and Crosson, 1990) and manual filtering to remove any excessive low frequency noise.

4) Application of eigenimage decomposition (Bostock and Sacchi, 1997, Freire and Ulrych, 1998) to identify the correlated portion of the signal, making the assumption that the correlated signal is a good estimate of the incident wavefield. The uncorrelated portion of the signal is taken to be the scattered wavefield in the direction of incident polarization.

5) Deconvolution of the estimated incident wavefield from the components of the scattered wavefield (Berkhout, 1977, Rondenay, 2005) to obtain the normalized scattered wavefield from an impulse response. A station specific damping factor (Pearce et al., 2012) was used so that damping of relatively noisy stations would not result in a loss of information at other stations

6) Recasting of the scattered wave impulse responses into the reference frame dictated by the 2-D geometry of the target structure and convolution of the resulting data sections with a phase shifting filter to recover material property perturbations (Bostick et al., 2001, Rondenay et al., 2005).

3.3 Modes

The migration of the scattered wavefield is performed for a number of different modes as described in the GRT section (3.1) and Fig. 1. The image for an individual mode is obtained by inverting scattered-wave travel times associated with that mode, subject to assumptions made about the background model (1-D isotropic background velocity model, 2-D geometry of scatterers). While single-mode images can provide important information about subsurface features, it is important to be cognizant of possible cross-contamination by other modes of scattering. This occurs because the peaks in the coda associated with other modes are interpreted as earlier or later signals, and manifest themselves as shallower or deeper versions of the actual features.

The composite images are generated by combining multiple modes into a single image. Here, the problem of cross-contamination is reduced, because the signal corresponding to real structure will sum up constructively, whereas the multiples and signals from other modes will not, leading to a real structure signal that is more focused and exhibits higher amplitudes (Fig. 1). Conversely, as the modes do not all exhibit identical resolution, composite images sometimes suffer from the inclusion of modes that are more poorly resolved.

4. Data

Our high-resolution seismic images were generated using data from a dense array of 41 three-component broadband seismometer stations, deployed along a roughly west to east profile across Washington state (Fig. 2c). This array was operational from July 2006 to September 2008, although not every station was recording for the entire time. Thirty-five of the stations were part of the Cascadia Array for Earthscope (CAFE) experiment, five were part of Earthscope's Transportable Array (TA), and the remaining station was operated by the Pacific Northwest Seismic Network (PNSN). The raw data are now publicly available from the archive for seismic data maintained by the Incorporated Research Institutions for Seismology (IRIS).

The stations were deployed along a dense, narrow band in the west to prevent image aliasing in the part of the system where the slab is shallowest (Rondenay et al., 2005, Suckale et al., 2009). As that constraint could be relaxed where the slab is deeper, the array was allowed to fan out in the east to better accommodate for other seismic methods such as tomography. For the purpose of 2-D GRT imaging, the stations were projected along a line oriented 100° from north – i.e., generally perpendicular to the geological strike of the subducting slab at this location (Abers et al., 2009) (Fig. 2a).

We selected events with a minimum magnitude of 5.7 that exhibited signal to noise ratio sufficiently high for successful alignment of the incident wavefield. Also required was an epicentral distance greater than 30° to prevent triplication from the mantle transition zone (Rondenay et al., 2001) and permit an incident plane wave assumption (Bostock et al., 2001) and less than 98° to rule out core diffracted phases. Records from the events that were stable during deconvolution were migrated, and only those reasonably free of ringing and exhibiting some sense of structure were used for the composite images. We generated migrated images for individual events using different combination of modes as well, in order to assess what each mode was contributing to the image for a given event. We removed modes that had very poor signal to noise or demonstrated excessive ringing. In all, data from sixty-three events covering a fairly comprehensive range of back-azimuth were used to generate our primary composite images (Fig. 2b). A complete list of the events used for these inversions along with a breakout of the modes used for each event can be found in the supplemental material (Supp. T. 1).

5. Results

The 2-D GRT images are presented in figure 3. The profiles show velocity perturbations relative to a background model as a function of horizontal distance (hereafter the x coordinate axis) and depth, with blue representing an increase in velocity and red a decrease. The GRT method has sensitivity to abrupt changes in velocity, which can be identified in the images as transitions from red to blue (slow to fast) or blue to red (fast to slow). A slow-to-fast transition with increasing depth is referred to as a positive discontinuity, and the opposite (fast-to-slow), a negative discontinuity.

The single mode image in figure 3a (P-velocity or $\delta\alpha/\alpha$) was produced using the backscattered PP mode. The composite image in Fig. 3b (S-velocity or $\delta\beta/\beta$) was produced by combining the inversion results for the backscattered Ps, SSv, and SSh modes along with the results for the forward scattered Ps mode (Fig 3c-f respectively, c.f., Fig 1 for definition of modes). The inclusion of the backscattered modes greatly improves resolution (Rondenay et al., 2009), and we can use the fact that each modal image focuses data that is independent from that focused by other modes to establish an effective robustness test. Accordingly, we consider a feature to be robust only when appears not only in the composite image, but in multiple individual modal images.

The most prominent feature in the composite $\delta\beta/\beta$ image (Fig. 3b) is a low velocity (red) layer (LVL) that dips towards the east. On the western (left) edge

of the image, the top of this layer is marked by a negative velocity discontinuity at a depth of 22 km, and the bottom by a positive discontinuity at a depth of 30 km. Following previous GRT migration work conducted in subduction settings, we interpret this LVL to represent the subducting oceanic crust (Rondenay et al., 2001, 2005, Nicholson et al., 2005, Abers et al., 2009).

The positive discontinuity indicates the location of the oceanic Moho, from which we can calculate a dip angle for the descending slab of ~8° between ~32 and ~42 km depth (x = 0 to ~65 km), which steepens to ~20° between ~42 and ~90 km depth (x = ~65 to ~180 km). Beyond this depth the discontinuity can no longer be traced. These values are consistent with previous estimates of slab dip based of Wadati-Benioff seismicity in the region (McCrory et al., 2006).

The LVL maintains an apparent thickness of ~7-8 km to a depth of ~35 km (x=60 km) where it appears to thicken considerably. Similar occurrences have been identified in previous work (Rondenay et al., 2001, Bostock et al., 2002, Nicholson et al., 2005), where the thickening was interpreted as serpentinization of the cold nose of the mantle wedge. In the previous studies, the apparent thickening was accompanied by the near disappearance of the low velocity crust, interpreted as the onset of eclogitization reactions within the crust. While a velocity increase occurs here for central Washington as well, the change is much more subdued, reducing the magnitude of the velocity perturbation by less than

a factor of two (i.e. from $d\beta/\beta$=~-.15 at x<90 km to $d\beta/\beta$=~-.10 at x>90 km). The diminished LVL continues at a steeper dip until it becomes indistinguishable from the background velocities at a horizontal distance of x=150-200 km and a depth of 80-95 km. Directly above where the LVL fades away completely, we find another low velocity feature, extending between depths of 65-85 km and from x=150-220. Like the persistence of the LVL to depth, this feature appears to be isolated to this part of the Cascadia subduction system

An additional robust feature observed in Fig. 3b is a positive velocity discontinuity at an average depth of ~42 km, which extends from x=180 to x=235. Again following previous work (Rondenay et al., 2001, Nicholson et al., 2005), we interpret this feature as the Moho of the overriding continental plate. The velocity contrast is not as strong here as it was in those studies and in fact was not evident at all in previous work using only part of the current data set (Abers et al., 2009). The discontinuity appears to exhibit some topography, including a concave up segment between x=180-200 followed by a concave down segment between x=200-220.

The $\delta\beta/\beta$ images are generally considered to be more robust than the $\delta\alpha/\alpha$ images due both to a more complete separation of the S-scattered waves from the incident wavefield and to the availability of multiple modes which improve volume and dip resolution (Rondenay, 2009). An examination of the $\delta\alpha/\alpha$

images is still warranted as it can provide additional and independent information. In particular, they can be used to establish the robustness of certain structures, since multiple contamination is less prevalent in the $\delta\alpha/\alpha$ images (Pearce et al., 2012). Moreover, differences between the $\delta\beta/\beta$ and $\delta\alpha/\alpha$ images can highlight regions in the subsurface where the background velocity model breaks down. If the background model is inaccurate with respect to the Vp/Vs ratio, the features will be mapped at the different depths on each image.

Our primary $\delta\alpha/\alpha$ image (Fig. 3a) exhibits many of the same features as the $\delta\beta/\beta$ image. The positive velocity transition at ~42 km in the east is present, extending from x=170 km to 210 km along the horizontal axis. The topography of this interface noted in the $\delta\beta/\beta$ image is arguably present here as well, though not as well defined. The dipping low velocity layer in the west is present, similar in location, thickness, and dip to that observed in the $\delta\beta/\beta$ image. The extension of the low velocity layer becomes difficult to trace beyond a depth of ~65 km, likely due to the limited resolution of the $\delta\alpha/\alpha$ image, which becomes increasingly limited with depth (Rondenay et al., 2005).

6. Discussion

6.1 Central Washington

6.1.1 The continental Moho

We interpret the positive velocity discontinuity at a depth of ~42 km in the eastern part of the image as the continental Moho, consistent with previous GRT migration studies (Rondenay et al., 2001, Bostock et al., 2002, Nicholson et al., 2005, Rondenay et al., 2010). In a preliminary study using a subset of this data (Abers et al., 2009), the continental Moho was not well imaged, probably due to diminished station coverage, as data from two critical stations were not recovered in time for that study due to weather conditions in the mountains.

The topography that appears along the continental Moho is consistent with isostatic compensation in response to the influence of the nearby Cascade Range, which is located directly above the concave up feature in the discontinuity. The 6 km deflection in the Moho would be consistent with a 1.1 km rise in the surface topography given a mantle density of 3300 kg/m^3 and a crustal density of 2800 kg/m^3. This 1.1 km rise is consistent with the local elevation, and is roughly a quarter of Mt. Rainier's peak height of 4.17 km.

6.1.2 The subduction system

We interpret the dipping low velocity layer extending from the western edge of the image as the subducting oceanic crust. The layer has a thickness of ~8 km and dips at slightly less than 10°, consistent with what we would expect for the oceanic crust at this location. The strong downward negative velocity gradient at the top of the layer has been interpreted to be either a weak layer of sediment or fluids in pressurized channels (Abers et al., 2009).

The positive velocity contrast at the bottom of the layer has typically been interpreted to represent the oceanic Moho (Abers et al., 2009), which can be seen reasonably clearly to a depth of more than 90 km. This velocity contrast is reduced in multiple stages, first at a depth of ~40 km, and again at a depth of ~80 km, corresponding to increases in the velocity of the subducting crust. The velocity increase at a depth of ~40 km is interpreted to reflect a material transformation in the upper crust from hydrated metabasalts to zoisite-amphibole eclogite (Helffrich, 1996, Bostock et al., 2002, Hacker et al., 2003a), along with a reduction in fluid pore pressure corresponding to a rupturing of the plate boundary seal (Audet et al., 2010, Bostock, 2012). For warm subduction zones, the eclogitization of hydrated metabasalts is largely controlled by pressure (Schmidt and Poli, 1998, Hacker et al., 2003a, Rondenay et al., 2008) and is expected to occur at depths of ~40-55 km in Cascadia (van Keken et al., 2011).

The fluids released from this eclogitization reaction migrate upward into the mantle wedge (Peacock, 1990), where they are taken up by hydration reactions resulting in the generation of several hydrous minerals such as chlorite, antigorite serpentine, talc, and brucite (Hyndman and Peacock, 2003, Ulmer and Trommsdorf, 1995). Like eclogitization, serpentinization of mantle material has seismological consequences, including a significantly lower velocity and an increase in Poisson's ratio (Bostock et al., 2002, Hyndman and Peacock, 2003). We interpret the low velocity region overlying the 40 km deep crust to be the serpentinized mantle wedge.

Our interpretation of the downgoing oceanic crust and Moho, eclogitization reaction within the oceanic crust, and serpentinized corner of the mantle wedge are consistent with identifications made during previous GRT migration studies in the Cascadia region (Rondenay et al., 2001, Nicholson et al., 2005, Abers et al., 2009). However, there are some important differences between the images from the work along other transects and the one from the current study that must be addressed.

The first of these differences relates to the retention of a significant low velocity signature in the subducting oceanic crust well beyond the eclogitization of the hydrated upper crust. This transition to zoisite amphibole eclogite is expected to raise the P-wave velocity of the crust from ~15% slower than the

underlying mantle to ~4% slower at depths starting at ~ 35 km, with a further transition at ~70 km to anhydrous eclogite which is expected to render the crustal velocity signature indistinguishable from the surrounding material (Hacker et al., 2003a). Our model shows a more subdued velocity change at ~35 km, retaining a clear contrast at the bottom of the layer to depths of 80-95 km. This contrast can be explained by the presence of a lower crustal layer of metastable gabbro (Hacker et al., 2003a, Rondenay et al., 2008), which could be as much as 5 km thick (Hacker, 2008, van Keken et al., 2011) and with a velocity as much as 12% slower than the underlying harzburgite (Hacker et al., 2003a).

The coarse-grained metastable gabbro lower crustal layer can transform directly to eclogite at pressures and temperatures that correspond to depths of ~80-90 km for Cascadia (John and Schenk, 2003, Hacker et al., 2003b), but this reaction tends to be extremely sluggish in the absence of free water (Hacker et al., 2008). A key catalyst is the introduction of water to pathways within the lower crust, therefore it is expected that dehydration of serpentine or chlorite in the harzburgite of the underlying mantle would accelerate this process (Schmidt and Poli, 1998, John and Schenk, 2003). The released fluids would access the gabbroic mass through channels created by volume reduction associated with the initiation of prograde metamorphism or alternately through stress related shearing (Bruhn et al., 2000, John and Schenk, 2003). Once initiated, the

transition from gabbro to eclogite furthers the volume reduction of the host rock, increasing the permeability and thereby enabling the infiltration of any remaining fluid (Aharonov et al., 1997, John and Schenk, 2003).

The second notable feature in the image that must be explained is the low velocity region that extends from x=170-210 and from depths of 60-80 km, which is consistent with a fluid or melt phase (Rondenay et al., 2010). The base of the feature appears to be roughly coincident with the top of the slab from depths of 75-90 km (mantle depths of 80-95 km), the same range over which the low velocity signature of the subducting crust disappears. While serpentinized peridotite in the upper mantle is only stable to depths of ~60-70 km in Cascadia (Hacker et al., 2003a, van Keken et al., 2011), chlorite bearing harzburgite is stable to temperatures approaching 800 C (Schmidt and Poli, 1998, Hacker et al., 2003a), corresponding to depths of ~80-95 km in Cascadia (Hacker et al., 2003a) with complete dehydration of the uppermost mantle by 115 km depth (van Keken et al., 2011). This suggests that chlorite rather than antigorite serpentine would have to be present in the upper mantle.

The thermal profile in Cascadia does not allow for extensive hydration of the oceanic upper mantle, but evidence of hydration has been found within the uppermost few km (Kao et al., 2008, Nedimovic et al., 2009). The velocity of chlorite harzburgite is roughly midway between that of metastable gabbro and

spinel harzburgite (Hacker et al., 2003a), so a relatively thin and localized hydrated upper mantle would blend into the low velocity crustal signature. This would imply that the extended low velocity layer imaged to depths of 80-95 km is a combination of a ~4 km thick metastable gabbro layer underlain by layer of chlorite harzburgite, also a few km thick.

Figure 5a shows the location of earthquake hypocenters occurring within 25 km of the projection line for our survey. Most of the hypocenters that appear to be associated with the descending slab are in locations consistent with what we would expect for the eclogitization of hydrated basalts in the upper crust (Hacker et al., 2003b). A few of the larger, deeper ones between x=110 and 150 km more likely represent dehydration of serpentine in the upper mantle (Hacker et al., 2003a, Kao et al., 2008). The systematic biases which affect hypocenter location tend to make them appear as much as 25 km farther from the ocean than they actually are (Syracuse and Abers, 2009), so all of these hypocenters may well be located somewhere within the mantle of the descending slab. There is a cluster of small earthquakes that do not fit this profile, at depths of 88-100 km and x=200-225 km, that are located directly below the low velocity fluid/melt feature. As the transition of metastable gabbro to eclogite is expected to be aseismic (John and Schenk, 2003), these hypocenters likely represent dehydration reactions in

the oceanic mantle, with depths that are consistent with the dehydration of chlorite.

The introduction of hydration alteration into the uppermost mantle can occur in a number of ways. Serpentinized mantle rocks have been found in oceanic lithosphere at slow and intermediate spreading ridges (Cannat, 1993, Carbotte et al., 2006), but the narrow axial valley at the Juan de Fuca ridge rules out this possibility for Cascadia (Canales et al., 2005, Carbotte et al., 2006). Likewise, hydration of the lower crust and upper mantle has been shown to occur during bend related faulting at the trench in Central America (Ranero et al., 2005, Key et al., 2012), but the shallow dip angle of ~7.5 degrees at the trench (McCrory et al., 2006) and a ~2 km thick sediment load that provides both a hydraulic barrier and thermal blanket (Divens et al., retrieved, 2012, Spinelli et al., 2004) make this scenario unlikely for Cascadia.

There is substantial evidence that some hydration of the lower crust and uppermost mantle does occur in Cascadia. Analysis of the magnitude 6.7 Nisqually earthquake also suggests hydration extending as much as 10 km into the mantle (Kao et al., 2008), and seismic reflection studies have found faulting and hydration up to 200 km seaward of the trench, in zones of potential plate weakness associated with propagator wakes (Nedimovic et al., 2009). The hydration of these faults appears to be largely restricted to lower crustal levels,

but in some cases, the faults have penetrated the Moho (Nedimovic et al., 2009). While serpentinization is normally the most important hydration mechanism associated with peridotites, the stability zone for serpentine is expected to extend no more than a few km into the mantle (Ulmer and Trommsdorf, 1995, Hyndman and Wang, 1995, Nedimovic et al., 2009). The widest of these propagator wake regions in Cascadia is coincident with the deep seismicity in the eastern part of our profile.

6.2 Implications for regional tectonics

In GRT imaging, the projection line azimuth must be chosen to be as close to perpendicular to the 2-D strike of the structure as possible, which for subduction zones is parallel to the direction of slab dip. When the steepest dip is in the direction of slab motion, we can think of the slab in cross-section as a progression through time, such that the condition of the slab at some depth z2 is a consequence of the reaction we image at a shallower depth z1. When the direction of steepest dip and slab motion differ significantly, the projection line cuts across the direction of slab motion and complicates this perception (Fig. 4).

Figure 5b-g show our study area in map view broken up into three corridors, with the region of our migrated image from x=0 to 50 km falling into the X

corridor, that from x=50 to 180 km into the Y corridor, and the eastern section from x=180 km into the Z corridor. The corridors have azimuths of 30 degrees north of east (40 degrees north of our projection line), consistent with the direction of relative plate motion (Fluck et al., 1997, Miller et al., 2001). The location of the boundaries for these corridors was directed by changes in the distribution of earthquake epicenters, which are also shown in the figures. The same biases regarding epicenter location (Syracuse and Abers, 2009) apply here as they did for figure 5a, but corrections for these biases would not undermine our general conclusions.

The segment of our projection line that crosses the Y corridor passes directly over the large concentration of events associated with dehydration reactions at depths of 38-70 km (Fig. 5d-f). These events densely populate the Y corridor and extend to some degree northward, but are almost completely absent within the Z corridor. Conversely, all of the events that occur at depths of greater than 70 km for this region fall within the Z corridor (Fig. 5g).

The previous GRT migration work done to the north (Nicholson et al., 2005) and south (Rondenay et al., 2001) provide a convenient framework within which we can make certain assertions regarding regional along-strike variation. Figure 6a depicts a regional map with three transects representing the projection lines from three different GRT migration experiments. The A-A' transect (Fig. 6b)

runs across the southeastern end of Vancouver Island and into southwest British Columbia (Nicholson et al., 2005). The C-C′ transect (Fig. 6d) is from a similar study conducted across central Oregon (Rondenay et al., 2001). The B-B′ transect (Fig. 6c) across central Washington state shows the projection line for the current experiment. The X, Y, and Z corridors are also included on the map, in addition to a Vancouver Island (VI) corridor which includes the A-A′ transect, and an Oregon (OR) corridor which brackets the C-C′ transect. The T corridor bridges the gap between Z and OR.

The three migrated images share a number of similarities in terms of general structure, but also show some striking differences. The degree of disappearance of the low velocity layer at a depth of 40-45 km is very pronounced in A-A′ (more than 80% of the original contrast), a bit less so in C-C′ (60%), and significantly more subdued in B-B′ (30%), suggesting that the metastable gabbro layer identified in central Washington is not equally present along-strike. The low velocity fluid/melt feature above the slab from x=160 to x=220 is also clearly present only in central Washington, so the deep, concentrated release of fluids from the upper mantle is probably a local feature as well, a conclusion supported by the distribution of earthquake hypocenters.

While several parameters vary along-strike in Cascadia (see Table 2), including subduction rate (Miller et al., 2001), plate age (Davis and Hyndman,

1989), and sedimentation (Divins et al., retrieved 2012), one of the parameters that correlate best with seismic activity is slab dip (Fig 6a). Because the slab dip is shallow for the VI, X, and Y corridors to depths of 30 km, the megathrust seismological locked and transitions zones extend eastward, the latter on to land (Fluck et al., 1997). The shallow earthquakes (33-38 km depth, Fig. 5b) near the coast correlate very well with the megathrust transition zone, and the vast majority of the intraslab activity takes place along these corridors.

The deeper earthquakes occur within the Z corridor, where a significant change in dip is accommodated. From a depth of 70 km to 110km, the dip increases within the corridor as much as 8° over a corridor-perpendicular distance of less than 50 km (McCrory et al., 2006, also see Fig. 6a and Table 2). The relationship between the earthquakes and the change in dip is perhaps less clear.

One possibility is that the change in dip is simply a result of deformation caused by the simple geometric constraints imposed by the curvature of the subduction zone (Creager and Boyd, 1991). While stresses associated with the changes could connect otherwise isolated pockets of fluid (Mibe et al., 2003, Bruhn et al., 2000) and the valley like topography formed by the changes in dip could channel fluids over a short horizontal profile, the presence of fluids would

not be required. Likewise, this interpretation would not explain differences in the Z corridor seaward of the change in dip.

Conversely, the changes in dip could be a result of the densification of the slab (Klemd et al., 2011) due to the fluid release from chlorite harzburgite in the upper mantle and subsequent triggering of the eclogitization reaction in the lower crust. This would require a fundamental difference in the incoming slab within the Z-corridor that could enable sufficient hydration of the upper mantle, such as zones of weakness associated with propagator wakes (Nedimovic et al., 2009).

The largest of these propagator wake zones includes the segment of the Z corridor imaged by this study (Fig. 6a), and also serves to delineate three very different regions of the Cascadia subduction zone. To the north, the dip of the plate is shallow, intraslab seismic activity is dense, and the 127 quaternary volcanic vents are tightly concentrated around the five major volcanoes (Mt. Meager is off the map to the north)(Hildreth, 2007). To the south, the plate dips more steeply, seismic activity is sparse, and more than 2000 quaternary vents form a near continuous array from Bumping Lake to the east of Mt. Rainier to very near the California border (Hildreth, 2007).

While most of the volcanism in the Cascades lies along the quaternary axis, there are four volcanic features within the forearc; three of them (Mt. Rainier, Mt.

St. Helens, and the Portland vent fields) lie within the wake propagator zone, and the fourth (Indian Head vent field) just along its southern edge.

Another possibility is that the changes in dip are connected to both ideas, with the weaknesses inherent in the wake propagator zone and the slab densification selecting the Z corridor for accommodation of the geometric constraints imposed by the curvature of the subduction zone.

7. Conclusion

In this study, we present a high resolution seismic cross section of the Cascadia subduction setting across central Washington State. We see an ~8 km thick low velocity layer descending from the west that we interpret as the oceanic crust, underlain by a sharp velocity transition that we take to be the oceanic Moho. A velocity reduction within the slab crust at a depth of ~35-45 km is consistent with the transformation of hydrated metabasalts in the upper crust to eclogite, and the low velocity nose in the mantle wedge is characteristic of serpentinite formed in the continental mantle by fluids rising from the slab during the eclogitization process. We also image a positive velocity transition at a depth of ~42 km in the east that we interpret to represent the continental Moho.

The transition of the low velocity oceanic crust due to the eclogitization of the hydrated basalts is more subdued than expected, suggesting that a layer of metastable gabbro is present in the lower crust. A velocity increase within the crust starting at ~80 km depth, and a overlying low velocity feature consistent with a pocket of released fluid or melt suggests the dehydration of chlorite in the upper mantle.

The region imaged by our profile at this depth appears to be unique for Cascadia, as it corresponds to the accommodation of a significant along-strike change in dip, a set of small earthquakes at a depth of 88-100 km, and the landward extension of a wake propagator zone. The interplay between these features could have important implications for the volcanic and seismic expressions of the Cascadia subduction system.

References for Chapter 2

Abers, G.A., MacKenzie, L.S., Rondenay, S., Zhang, Z., Wech, A.G., Creager, K.C., 2009. Imaging the source region of Cascadia tremor and intermediate-depth earthquakes. Geology 37, 1119-1122.

Adams, J., 1990. Paleoseismicity of the Cascadia subduction zone: Evidence from turbidites off the Oregon-Washington margin. Tectonics 9, 569-583.

Atwater, B.F., Tuttle, M.P., Schweig, E.S, Rubin, C.M, Yamaguchi, D.K., Hemphill-Haley, E., 2004. Earthquake recurrence inferred from paleoseismology. Dev. in Quat. Sci. 1, 331-348.

Audet, P., Bostock, M.G., Christensen, N.I., Peacock, S.M., 2009. Seismic evidence for overpressurized subducted oceanic crust and megathrust fault sealing. Nature, 457, 76-78.

Audet, P., Bostock, M.G., Boyarko, D.C., Brudzinski, M.R., Allen, R.M., 2010. Slab morphology in the Cascadia fore arc and its relation to episodic tremor and slip. J. Geophys. Res. 115, B00A16.

Berkhout, A.J., 1977. Least-squares inverse filtering and wavelet deconvolution. Geophysics 42, 1369-1383.

Bostock M.G., Rondenay, S., Shragge, J., 2001. Multiparameter two-dimensional inversion of scattered teleseismic body waves. 1. Theory for oblique incidence. J. Geophys. Res. 106, 30771-30782.

Bostock M.G., Hyndman, R.D., Rondenay, S., Peacock, S.M., 2002. An inverted continental Moho and serpentinization of the forearc mantle. Nature 417, 536-538.

Bostock M.G., Rondenay S., 1999. Migration of scattered teleseismic body waves. Geophys. J. Int. 137, 732-746.

Bostock, M.G., Sacchi, M.D., 1997. Deconvolution of teleseismic recordings for mantle structure. Geophys. J. Int. 129, 143-152.

Brudzinski, M.R., Allen, R.M., 2007. Segmentation in episodic tremor and slip all along Cascadia. Geology 35, 907-910.

Bruhn, D., Groebner, N., Kohlstedt, D.L., 2000. An interconnected network of core-forming melts produced by shear deformation. Nature 403, 883-886.

Canales, J.P., Detrick, R.S., Carbotte, S.M., Kent, G.M., Diebold, J.B., Harding, A., Babcock, J., Nedimovic, M.R., van Ark, E., 2005. Upper crustal structure and axial topography at intermediate spreading ridges: Seismic constraints from the southern Juan de Fuca ridge. J. Geophys. Res. 110, B12104.

Cannat, M., 1993. Emplacement of mantle rocks in the seafloor at mid-ocean ridges. J. Geophys. Res. 98, 4163-4172.

Carbotte, S.M., Detrick, R.S., Harding, A., Canales, J.P., Babcock, J., Van Ark, E., Nedimovic, M., Diebold, J., 2006. Rift topography linked to magmatism at the intermediate spreading Juan de Fuca ridge. Geology 34, 209-212.

Chadwick, J., Perfit, M., Ridley, I., Jonasson, I., Kamenov, G. et al., 2005. Magmatic effects of the Cobb hot spot on the Juan de Fuca ridge. J. Geophys. Res. 110, B03101.

Creager, K.C., Boyd, T.M., 1991. The geometry of Aleutian subduction: Three-dimensional kinematic flow model. J Geophys. Res. 96, 2293-2307.

Davis, E.E., Hyndman R.D., 1989. Accretion and recent deformation of sediments along the northern Cascadia subduction zone. Geol. Soc. of Am. Bull. 101, 1465-1480.

Divins, D.L., retrieved 2012. NGDC total sediment thickness of the world's oceans and marginal seas. http://www.ngdc.noaa.goc/mgg/sedthick/sedthick.html.

Eagar K.C., Fouch, M.J., James, D.E., 2010. Receiver function imaging of upper mantle complexity beneath the Pacific Northwest, United States. Earth Planet. Sci. Lett. 297, 141-153.

Fluck, P., Hyndman, R.D., Wang, K., 1997. Three-dimensional dislocation model for great earthquakes of the Cascadia subduction zone. J. Geophys. Res. 102, 20539-20550.

Friere, S.L.M, Ulrych, T.J., 1998. Application of singular value decomposition to vertical seismic profiling. Geophys. 53, 778-785.

Furukawa, Y., 1993. Depth of the decoupling plate interface and thermal structure under arcs. J. Geophys. Res. 98, 20005-20013.

Gao H., Humphreys E.D., Yao, H., van der Hilst, R.D., 2011. Crust and lithosphere structure of the northwestern U.S. with ambient noise tomography: Terrane accretion and Cascade arc development. Earth Planet. Sci. Lett. 304, 202-211.

Hacker, B.R., Abers, G.A., Peacock, S.M., 2003a. Subduction factory 1. Theoretical mineralogy, densities, seismic wave speeds, and H_2O contents. J. Geophys. Res. 108(B1), 2029, doi:10.1029/2001JB001127.

Hacker, B.R., Peacock, S.M., Abers, G.A., 2003b. Subduction factory 2. Are intermediate-depth earthquakes in subducting slabs linked to metamorphic dehydration reactions? J. Geophys. Res. 108(B1), 2030, doi:10.1029/2001JB001129.

Hattori, K.H., Guillot, S., 2003. Volcanic fronts form as a consequence of serpentine dehydration in the forearc mantle wedge. Geology 31, 525-528.

Helffrich, G., 1996. Subducted lithospheric slab velocity structure: Observations and mineralogical inferences, in Bebout, G., et al., eds., Subduction top to bottom: American Geophysical Union Geophysical Monograph 96, 215-222.

Hyndman, R.D., 1988. Dipping seismic reflectors, electrically conductive zones, and trapped water in the crust over a subducting plate. J. Geophys. Res. 93, 13391-13405.

Hyndman, R.D., Peacock, S.M., 2003. Serpentinization of the forearc mantle. Earth. Planet. Sci. Lett. 212, 417-432.

John T., Schenk, V., 2003. Partial eclogitization of gabbroic rocks in a late Precambrian subduction zone (Zambia): prograde metamorphism triggered by fluid infiltration. Contrib. Mineral Petrol. 146, 174-191.

Kao, H., Wang., K., Chen, R. –Y., Wada, I., He, J., Malone, S.D., 2008. Identifying the rupture plane of the 2001 Nisqually, Washington earthquake. Bull. Seis. Soc. Am., 98, 1546-1558.

Key, K., Constable, S., Matsuno, T., Evans, R.L., Myer, D., 2012. Electromagnetic detection of plate hydration due to bending faults at the Middle America Trench. Earth Planet. Sci. Lett. 351-352, 45-53.

Kawakatsu, H., Watada, S., 2007. Seismic evidence for deep-water transportation in the mantle. Science 316, 1468-1471.

Kennett, B.L.M., 1991. The removal of free surface interactions from three-component seismograms. Geophys. J. Int. 104, 153-163.

Kirby, S.H., Wang, K., 2002. Introduction to a global systems approach to Cascadia slab processes and associated earthquake hazards. The Cascadia Subduction Zone and Related Subduction Systems (BOOK)

Kirby, S., Engdahl, E.R., Denlinger, R., 1996. Intermediate-depth intraslab earthquakes and arc volcanism as physical expressions of crustal and uppermost mantle metamorphism in subducting slabs, in Bebout, G., et al., eds., Subduction top to bottom: American Geophysical Union Geophysical Monograph 96, 195-214.

Klemd R., John, T., Scherer, E.E., Rondenay, S., Gao, J., 2011. Changes in dip of subducted slabs at depth: Petrological and geochronological evidence from HP-UHP rocks (Tianshan, NW-China). Earth Planet. Sci. Lett. 310, 9-20.

McCrory, P.A., Blair, J.L, Oppenheimer, D.H., Walter, S.R., 2006. Depth to the Juan de Fuca slab beneath the Cascadia subduction margin- A 3-D model for sorting earthquakes. U.S. Geological Survey data series 91.

Mibe, K., Yoshino, T., Ono, S., Yasuda, A., Fujii, T., 2003. Connectivity of aqueous fluid in eclogite and its implications for fluid migration in the Earth's interior. J. Geophys. Res. 108(B6), 2295, doi:10.1029/2002JB001960.

Miller, M.M, Johnson, D.J., Rubin, C.M., Dragert, H., Wang, K., Qamar, A., Goldfinger, C., 2001. GPS-determination of along-strike variation in Cascadia margin kinematics: Implications for relative plate motion, subduction zone coupling, and permanent deformation. Tectonics 20, 161-176.

Miller, D., Oristaglio, M., Beylkin, G., 1987. A new slant on seismic imaging: Migration and internal geometry. Geophysics 52, 943-964.

Nedimovic, M., Bohnenstiehl, D., Carbotte, S., Canalas, J.P., Dziak, R., 2009. Faulting and hydration of the Juan de Fuca plate system. Earth Planet. Sci. Lett. 284, 94-102.

Nelson, A.R., Atwater, B.F., Bobrowsky, P.T., Bradley, L.-A., Clague, J.J. et al., 1995. Radiocarbon evidence for extensive plate-boundary rupture about 300 years ago at the Cascadia subduction zone. Nature 378, 371-374.

Nelson, A.R., Kelsey, H.M., Witter R.C., 2006. Great earthquakes of variable magnitude at the Cascadia subduction zone. Quaternary Research 65, 354-365.

Nicholson T., Bostock, M., Cassidy, J.F., 2005. New constraints on subduction zone structure in northern Cascadia. Geophys, J. Int. 161, 849-859.

Peacock, S.M., 1990. Fluid processes in subduction zones. Science 248, 329-337.

Pearce F.D., Rondenay, S., Sachpazi, M., Charalampakis, M., Royden, L.H., 2012 (submitted). Seismic investigation of the transition from continental to oceanic subduction along the western Hellenic subduction zone.

Poli, S., Schmidt, M.W., 2002. Petrology of subducted slabs. Annu. Rev. Earth Planet. Sci. 30, 207-235.

Preston, L.A., Creager, K.C., Crosson, R.S., Brocher, T.M., Trehu, A.M., 2003. Intraslab earthquakes: Dehydration of the Cascadia Slab. Science 302, 1197-2000.

Ramachandran K., Hyndman, R.D., Brocher, T.M., 2006. Regional P wave velocity structure of the northern Cascadia subduction zone. J.Geophys. Res. 111, B12301.

Ranero, C.R., Villasenor, A., Phipps-Morgan, J., Weinrebe, W., 2005. Relationship between bend-faulting at trenches and intermediate-depth seismicity. Geochem. Geophys. Geosyst. 6(12), 1-25.

Rogers, G.C., 1998. Earthquakes and earthquake hazards in the Vancouver areal. Bull. Geol. Surv. Can., 525, 17-25.

Rogers G., Dragert H., 2003. Episodic tremor and slip on the Cascadia subduction zone: The chatter of silent slip. Science 300, 1942-1943.

Rondenay, S., Bostock, M.G., Shragge, J., 2001. Multiparameter two-dimensional inversion of scattered teleseismic body waves. 3. Application to the Cascadia 1993 data set. J. Geophys. Res. 106, 30795-30807.

Rondenay, S., Bostock, M.G., Fischer, K.M., 2005. Multichannel inversion of scattered teleseismic body waves: practical considerations and applicability. Geophys. Monograph 157, 187-203.

Rondenay, S., Abers, G.A., van Keken, P.E., 2008. Seismic imaging of subduction zone metamorphism. Geology 36, 275-278.

Rondenay, S., 2009. Upper mantle imaging with array recordings of converted and scattered teleseismic waves. Surv. Geophys. 30, 377-405.

Rondenay, S., Montesi, L.G.J., Abers, G.A., 2010. New geophysical insight into the origin of the Denali volcanic gap. Geophys. J. Int. 182, 613-630.

Roth, J.B., Fouch, M.J., James, D.E., Carlson, R.W., 2008. Three-dimensional seismic velocity structure of the northwestern United States. Geophys. Res. Lett. 35, L15304.

Satake K., Shimazaki, K., Tsuji, Y. Ueda, K., 1996. Time and size of a giant earthquake in Cascadia inferred from Japanese tsunami records of January 1700. Nature 379, 246-249.

Schmandt, B., Humphreys, E., 2010. Complex subduction and small-scale convection revealed by body-wave tomography of the western United States upper mantle. Earth Planet. Sci. Lett. 297, 435-445.

Shragge J., Bostock, M.G., Rondenay, S., 2001. Multiparameter two-dimensional inversion of scattered teleseismic body waves. 2. Numerical examples. J. Geophys. Res. 106, 30783-30793.

Spinelli, G.A., Giambalvo, E.R., Fisher, A.T., 2004. Sediment permeability, distribution, and influence on fluxes in oceanic basement. Hydrogeology of the Oceanic Lithosphere, eds. Davis E.E. and Elderfield, H., Cambridge University Press.

Suckale J., Rondenay, S., Sachpazi, M., Charalampakis, M., Hosa, A., Royden, L.H., 2009. High-resolution seismic imaging of the western Hellenic subduction zone using teleseismic scattered waves. Geophys. J. Int. 178, 775-791.

Syracuse, E.M., van Keken, P.E., Abers, G.A., 2010. The global range of subduction zone thermal models. Phys. Earth Planet. Interiors 183, 73-90.

Syracuse, E.M., Abers, G.A., 2009. Systematic biases in subduction zone hypocenters. Geophys. Res. Lett. 36, L10303.

Ulmer P., Trommsdorff, V., 1995. Serpentine stability to mantle depths and subduction related magmatism. Science 268, 858-861.

Van Decar, J.C., Crosson, R.S., 1990. Determination of teleseismic relative phase arrival times using multi-channel cross-correlation and least squares. Bull. Seismol. Soc. Am. 80, 150-159.

van Keken, P.E., Hacker, B.R., Syracuse, E.M., and Abers, G.A., 2011. Subduction factory: 4. Depth-dependent flux of H_2O from subducting slabs worldwide. J. Geophys. Res. 116, B01401.

Wada, I., Wang, K., He, J., Hyndman, R.D., 2008. Weakening of the subduction interface and its effects on surface heat flow, slab dehydration, and mantle wedge serpentinization. J. Geophys. Res. 113, B04402.

Wheat, C.G, Mottl, M.J., 1994. Hydrothermal circulation, Juan de Fuca ridge eastern flank: Factors controlling basement water composition. J. Geophys. Res. 99, 3067-3080.

Yang, Y-J., Ritzwoler, M.H., Lin, F.-C, Moschetti, M.P., Shapiro, N.M., 2008. Structure of the crust and uppermost mantle beneath the western United States revealed by ambient noise and earthquake tomography. J. Geophys. Res. 113, B12310.

FIGURES

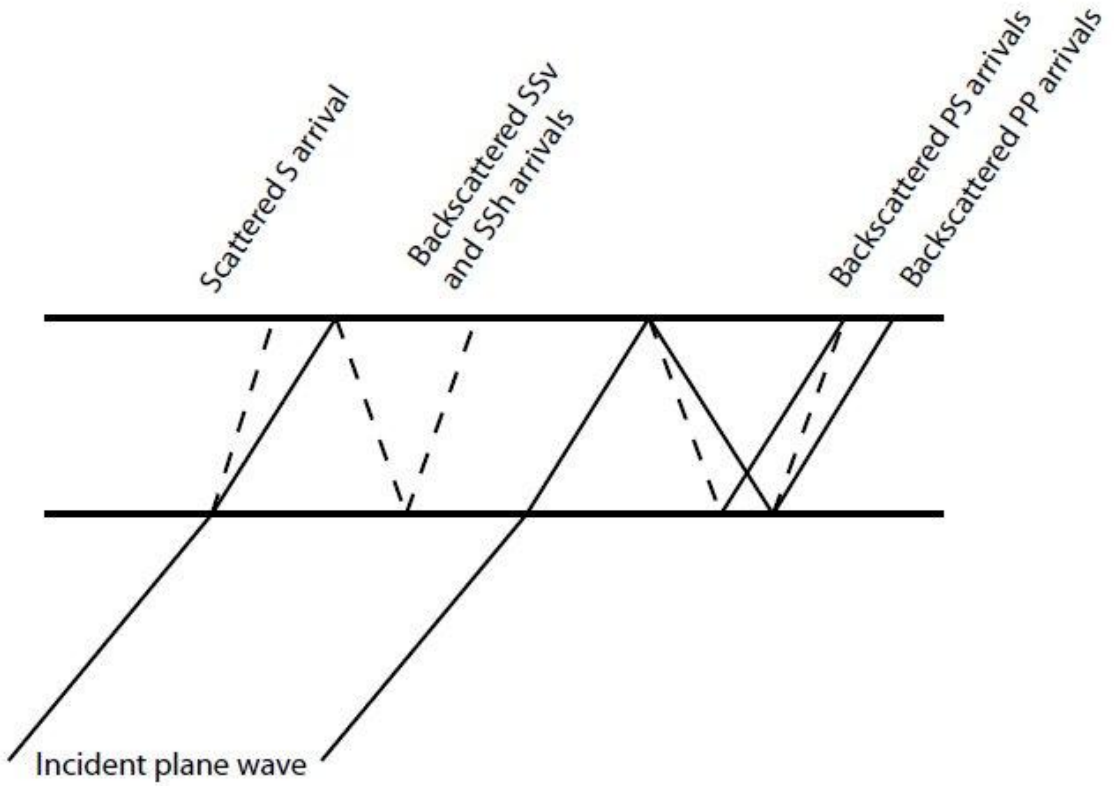

Figure 1: A simple illustration of the modes used for the migrated sections in this paper. The incident plane P-wave encounters a scattering contact in the subsurface, such that the energy of the transmitted wave is divided into P wave components (solid lines) and S wave components (dashed lines). The $\delta\alpha/\alpha$ (P-wave) sections show the backscattered PP mode in isolation, whereas the $\delta\beta/\beta$ (S-wave) sections show composite images that incorporate the forward PS, and backscattered PS, SSv, and SSh modes. The SSv and SSh modes differ only in polarization, with the SSv being the component of the wave polarized in the vertical, and SSv being the component polarized in the horizontal.

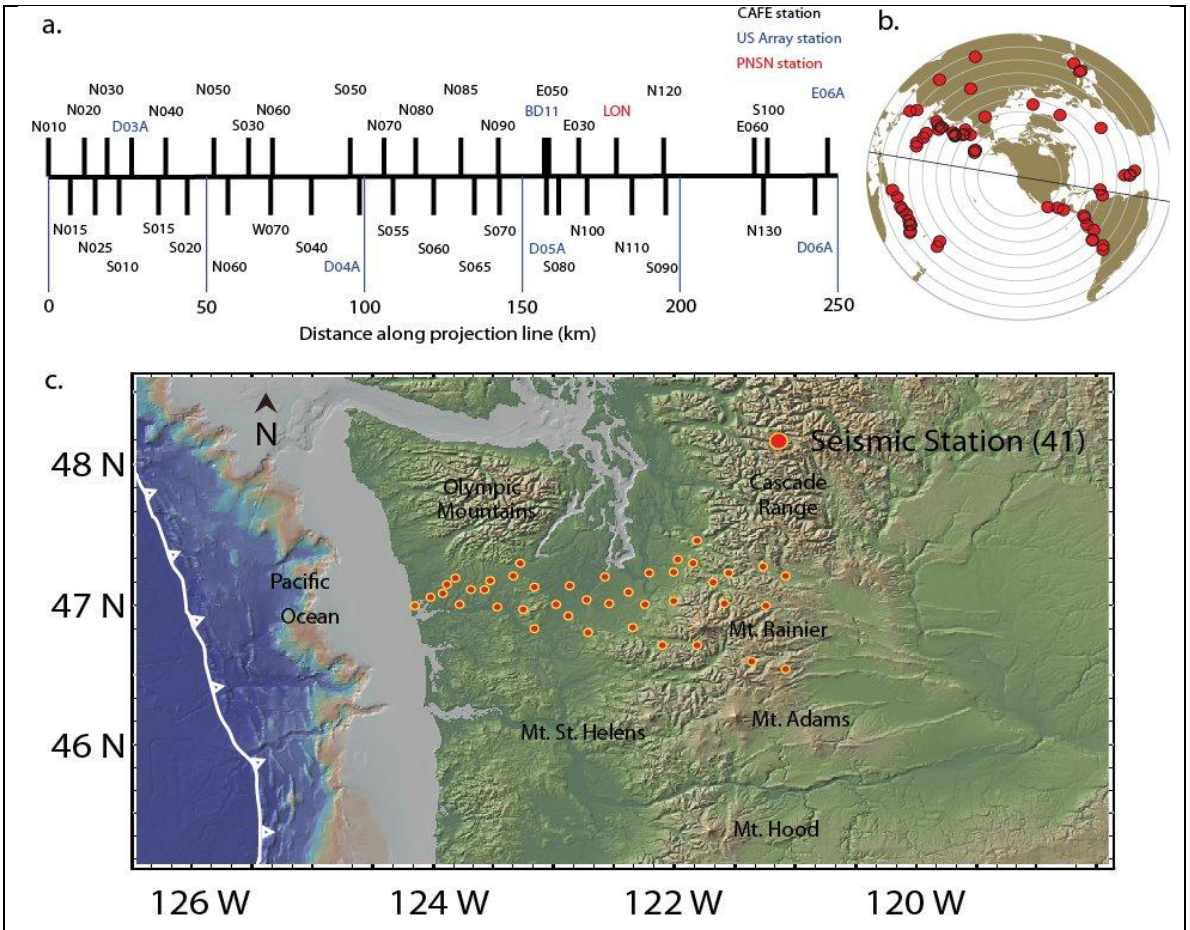

Figure 2: Data: The bottom of this figure shows the regional map of Washington state for the CAFE line, with the location of the 41 stations plotted. The names for the specific station and their position along the selected projection line of 100° east of north is given in the above left, color coded to denote affiliation. The 63 events used to generate our primary migrated sections are plotted on the hemispherical map in the upper right.

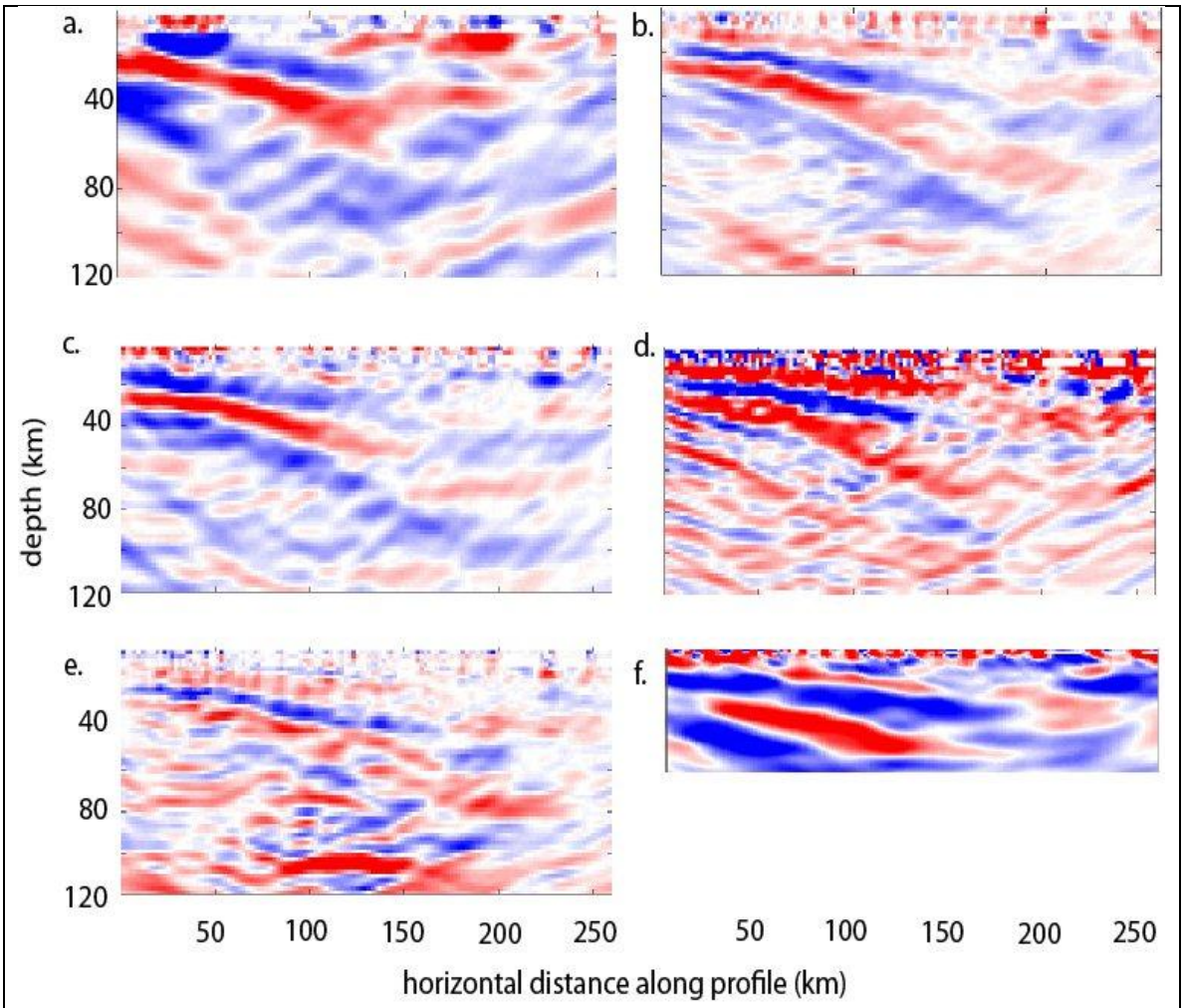

Figure 3: Raw sections for the CAFE line migration. Figure 3a is the primary $\delta\alpha/\alpha$ image for the set, and figure 3b is the primary composite $\delta\beta/\beta$ image, composed of the backscattered PS (figure 3c), the backscattered SSv (figure 3d), the backscattered SSh (figure 3e), and the forward scattered PS (figure 3f) modes.

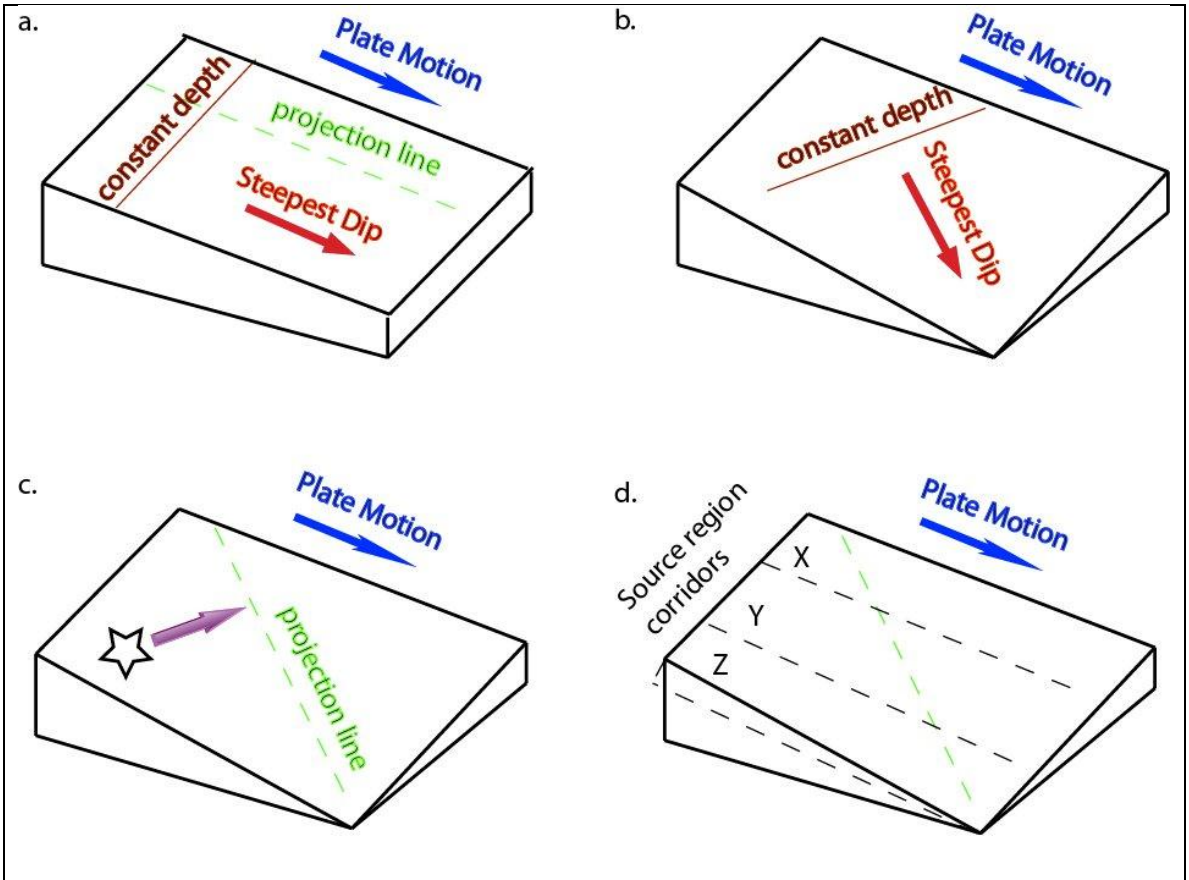

Figure 4: A comparison of the consequences of differences between the direction of the projection line (which is associated with steepest dip) and the direction of plate motion. A migrated section that follows a projection line that differs from the direction of plate motion is sampling different source regions across its length.

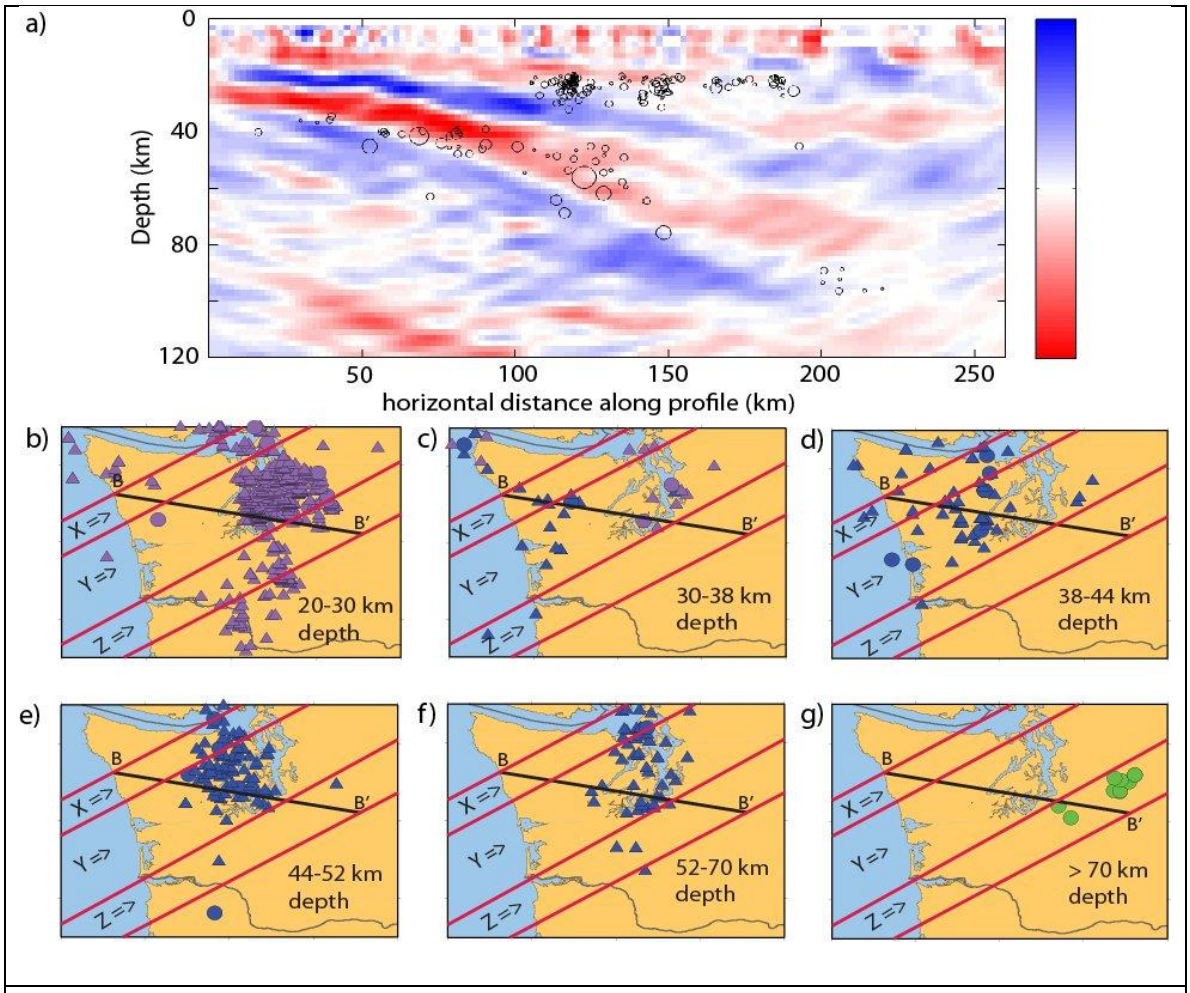

Figure 5: Earthquake distribution: Figure 5a shows the distribution of earthquakes across the migrated image, including earthquakes occurring between 1970-2012 within 25 km to either side of the projection line. The size of the circles corresponds to the magnitude of the earthquakes, with the smallest representing magnitudes between 1.0 and 2.0, and the largest showing the location of the 2001 6.8 magnitude Nisqually earthquake. Figures 5b-5g show the earthquake locations in map view for a selection of depths, and also the choice of corridors to understand the distribution of earthquakes in the context of direction of plate motion. All earthquake hypocenter locations courtesy of IRIS seismiquery.

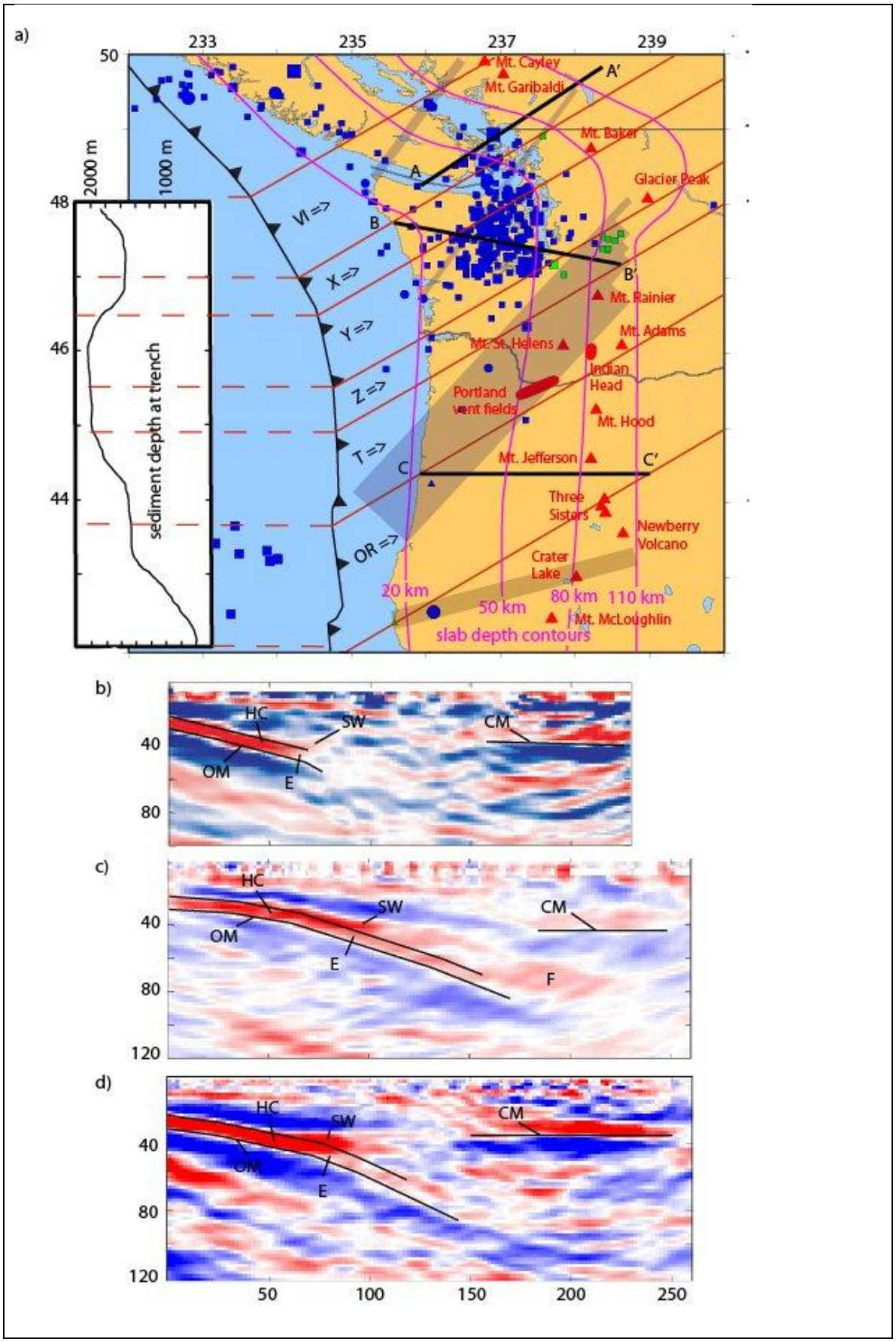
a)
233
235
237
239
50
48
46
44
2000 m
1000 m
sediment depth at trench
VI =>
X =>
Y =>
Z =>
T =>
OR =>
Mt. Cayley
Mt. Garibaldi
A
A'
Mt. Baker
Glacier Peak
B
B'
Mt. Rainier
Mt. Adams
Mt. St. Helens
Indian Head
Portland vent fields
Mt. Hood
Mt. Jefferson
C
C'
Three Sisters
Newberry Volcano
Crater Lake
20 km
50 km
80 km
110 km
Mt. McLoughlin
slab depth contours
b)
HC
SW
CM
OM
E
40
80
c)
HC
SW
CM
OM
E
F
40
80
120
d)
HC
SW
CM
OM
E
40
80
120
50
100
150
200
250

Figure 6: Regional interpretation: Figure 6a shows a map of the region containing three GRT migration studies. The northernmost, A-A', is from a study done by Nicholson et al., 2005. The southernmost, C-C', is from a study done by Rondenay et al., 2001. The CAFE line, B-B' reflects the work done for this current experiment. The map includes the selection of corridors for the entire region, extending from the trench, and a plot of sediment thickness at the trench (Divens et al., retrieved 2010). It also shows slab depth contour lines for 20, 50, 80, and 110 km depths (McCrory et al., 2006). Earthquakes shallower than 70 km depth are shown as blue symbols, and those greater than 70 km are shown as green symbols (Iris Seismiquery, 2012). Red triangles mark the location of volcanoes. Wake propagator zones are included as shaded regions (Nedimovic et al., 2007). Figure 6b-6d show the migrated sections for A-A', B-B', and C-C' respectively. HC=hydrated crust, OM= oceanic Moho, SW = serpentinized wedge, E= eclogitization reaction, CM= continental Moho, F= fluid/melt phase

TABLES

Background velocity model			
Depth(km)	Vp	Vs	Density
0-1	5.4	3.09	2.6
1-4	5.4	3.09	2.6
4-9	6.38	3.65	2.6
9-16	6.59	3.77	2.8
16-20	6.73	3.85	3.1
20-25	6.86	3.92	3.1
25-41	6.96	3.98	3.1
41-71	7.8	4.46	3.5
71-300	7.8	4.46	3.5

Table 1: The background velocity model used for the final migrated section for the CAFE line.

	Rate of subduction (a)	Sediment depth at trench (b)	Plate age at trench (c)	Earthquakes 20-30 km depth (d)	Earthquakes 30-44 km depth (d)	Earthquakes 44-70 km depth (d)	Earthquakes >70 km depth (d)	Initial subduction angle (trench to 10km depth) (e)	Subduction angle prior to eclogitization (10-30 km depth) (e)	Subduction angle after eclogitization (50-70 km depth) (e)
VI	36.9 mm/a	1600-1800 m (south of Nitenat fan)	5-7 Ma	Some	Some 35-38 km depth (transition zone near coast) more inland	few	1 near border at 73.3 km depth	7.1 ☒	10.2 ☒	21.8 ☒
XY	34.3 mm/a	1800-2000 m (Astoria Fan)	7-8 Ma	Some in X Many in Y	Same as VI	many	none	7.5 ☒	8.5 ☒	20.5 ☒
Z	34.3 mm/a	2000 m (Astoria Fan)	8 Ma	Some Skewed west vs. XY	Essentially none	Essentially none	2 at 72-76 and cluster of 8 at >88 km depth	10.1 ☒	8.7 ☒	22.1 ☒
T	32.1 mm/a	1500-1800 m	8.5 Ma	Some Skewed more west (follows slab depth 45-50 km)	none	Essentially none	none	11.0 ☒	9.6 ☒	18.0 ☒
OR	30.9 mm/a	600-1400 m	8.5-9 Ma	Only on T border	none	Essentially none	none	10.1 ☒	9.7☒	15.8 ☒

(a) Miller et al., 2001
(b) Divins et al., retrieved 2012, Fluck et al., 1997
(c) Davis and Hyndman, 1989
(d) IRIS seismiquery
(e) McCrory et al., 2006

Table 2: A selection of parameters related to along-strike variation in the Cascadia subduction system

Supplemental Table 1: This table shows the events used and modes used for each event in generating the primary images. The events are in the year-Julian date-time format used for IRIS seismiquery. Modes designated '1' were used in the composite images, while modes designated '0' were not. The last column gives the quadrant for the backazimuth of a given event.

EVENT	S	PP	PS	SSv	SSh	Quadrant
'20062192218'	'0'	'1'	'1'	'1'	'1'	III
'20062231430'	'1'	'0'	'1'	'1'	'1'	II
'20062291111'	'0'	'1'	'1'	'1'	'0'	IV
'20062291520'	'1'	'1'	'1'	'1'	'1'	IV
'20062362150'	'0'	'1'	'1'	'0'	'1'	IV
'20062441018'	'0'	'1'	'1'	'1'	'0'	III
'20062710622'	'1'	'0'	'0'	'1'	'0'	III
'20062721308'	'1'	'1'	'0'	'1'	'1'	II
'20062731750'	'0'	'1'	'1'	'1'	'1'	IV
'20062761803'	'0'	'1'	'0'	'1'	'0'	III
'20062900125'	'0'	'1'	'1'	'1'	'0'	III
'20062962117'	'0'	'1'	'1'	'1'	'1'	IV
'20063191114'	'0'	'1'	'1'	'1'	'1'	IV
'20063411910'	'1'	'1'	'1'	'1'	'1'	IV
'20070130423'	'1'	'1'	'1'	'1'	'1'	IV
'20070302137'	'0'	'1'	'1'	'1'	'1'	IV
'20070770211'	'1'	'0'	'0'	'1'	'1'	II
'20070950356'	'1'	'1'	'1'	'1'	'1'	I
'20071502022'	'0'	'0'	'0'	'1'	'0'	IV
'20071641929'	'1'	'1'	'1'	'1'	'1'	II
'20071960927'	'0'	'0'	'0'	'1'	'0'	III
'20071970113'	'0'	'1'	'1'	'1'	'1'	IV
'20071971417'	'1'	'1'	'1'	'1'	'1'	IV
'20072272022'	'1'	'0'	'0'	'1'	'0'	IV
'20072280516'	'1'	'1'	'1'	'1'	'1'	II
'20072280839'	'1'	'1'	'1'	'1'	'1'	III
'20072300252'	'1'	'1'	'1'	'1'	'1'	II
'20072322242'	'1'	'1'	'1'	'1'	'1'	I
'20072461614'	'0'	'1'	'1'	'1'	'1'	IV
'20072491751'	'0'	'0'	'1'	'1'	'0'	IV
'20072530149'	'1'	'1'	'1'	'1'	'1'	II

'20072711338'	'0'	'1'	'1'	'1'	'1'	IV
'20073200313'	'1'	'1'	'1'	'1'	'1'	II
'20073331900'	'1'	'1'	'1'	'1'	'0'	I/II
'20073500809'	'0'	'1'	'0'	'1'	'1'	II
'20073530930'	'1'	'1'	'1'	'0'	'1'	IV
'20080351701'	'1'	'1'	'0'	'0'	'1'	II
'20080390938'	'1'	'1'	'0'	'1'	'0'	I
'20080431250'	'1'	'0'	'1'	'1'	'0'	II
'20080451009'	'0'	'1'	'0'	'0'	'1'	I
'20080520246'	'1'	'0'	'0'	'1'	'0'	I
'20080580654'	'0'	'1'	'1'	'0'	'1'	IV
'20080630931'	'0'	'1'	'1'	'1'	'1'	IV
'20080802232'	'1'	'1'	'1'	'1'	'1'	IV
'20080822124'	'0'	'0'	'0'	'1'	'0'	IV
'20081001246'	'1'	'0'	'1'	'1'	'0'	III
'20081330628'	'1'	'1'	'1'	'1'	'1'	IV
'20081441935'	'1'	'1'	'0'	'1'	'1'	I
'20081501546'	'1'	'1'	'1'	'1'	'1'	I
'20081530157'	'0'	'0'	'1'	'0'	'0'	IV
'20081551620'	'0'	'1'	'1'	'1'	'1'	III
'20081601225'	'0'	'1'	'0'	'1'	'0'	I
'20081652343'	'0'	'0'	'0'	'1'	'1'	IV
'20081742356'	'1'	'1'	'1'	'1'	'0′	IV
'20081782119'	'1'	'1'	'0'	'1'	'0'	III
'20081870212'	'1'	'1'	'1'	'1'	'1'	IV
'20081970326'	'1'	'1'	'1'	'1'	'1'	I
'20082010239'	'0'	'1'	'1'	'1'	'1'	IV
'20082010927'	'1'	'1'	'1'	'1'	'0'	III
'20082051526'	'1'	'1'	'1'	'1'	'1'	IV
'20082392100'	'1'	'1'	'1'	'1'	'1'	II
'20082400135'	'1'	'1'	'1'	'1'	'0'	IV
'20082521852'	'1'	'1'	'1'	'1'	'1'	III
'20082541308'	'1'	'1'	'0'	'1'	'1'	I

3. Magnetotelluric imaging of the Cascadia subduction system beneath central Washington

Abstract

In this chapter we present images from the inversion of magnetotelluric data acquired from a dense line of 60 broadband and 20 long period instruments installed in central Washington. We image a dipping resistive feature in the west consistent with the subducting oceanic slab. We also image two conductors that are consistent with the release of fluids from the top of the slab, one at a depth of ~ 40 km and the other at a depth of 80-90 km. The deeper conductor is very conductive, indicating the presence of substantial fluid and/or melt, and rises in a column to another conductive feature that we interpret to be a magma chamber associated with Mt. Rainier. The root of Mt. Rainier shows up as a resistive feature that extends into the Western Cascades, giving way to a well known conductive feature beneath the High Cascades. A comparison of the model with the seismic image from Chapter 2 shows that the rising conductor is associated with the disruption of the continental Moho, and that the source of the conductor at 80 km depth is coincident with the low velocity feature in the migrated seismic image that we interpreted as fluids or melt. While the image is consistent with the seismic image and provides substantial new information on its own, an assessment of the model itself suggests ways in which it might be improved, a challenge taken up in the final chapter.

1. Introduction

Many of the natural hazards associated with subduction zones are intimately tied to the release of fluids bound within the subducting slab. Intraslab earthquakes have been linked with a process in which fluids released during the transformation of hydrated metabasalts to eclogite in the upper crust increases pore pressure, thereby reactivating pre-existing faults (Kirby et al., 1996, Hacker et al., 2003b, Preston et al., 2003). Slow slip and low frequency tremor, which have been tentatively linked with the periodicity of great megathrust earthquakes (Mazzotti and Adams, 2004), can be explained by episodic buildup and release of fluid pore pressure across plate boundaries down-dip of the locked zone (Abers et al., 2009, Audet et al., 2010). Most arc magmas are also generally believed to be generated by flux melting that occurs when dehydration reactions in the oceanic crust and uppermost mantle release fluids into the continental asthenosphere (Ulmer and Trommsdorff, 1995, Kirby et al., 1996). Finally, density increases associated with dehydration have been linked with changes in slab dip and increased stresses within the slab (Klemd et al., 2011).

Magnetotellurics (MT) is an attractive method to apply to subduction settings because MT is particularly sensitive to electrically conductive fluid phases and melt, and can therefore be used to constrain the location of fluids released during dehydration reactions. Fluids associated with dehydration reaction in both the

forearc and backarc have been detected using MT in several subduction zones, including Costa Rica (Worzewski et al., 2011, Brasse et al., 2009) and Cascadia to the north (Soyer and Unsworth, 2006) and south (Wannamaker et al., 1989, Evans et al., submitted) of the present study.

Beneath central Washington, the Juan de Fuca plate is subducting at a rate of approximately 35 mm/yr, at an angle 20-35 degrees north of east (Fluck et al., 1997, Miller et al., 2001). The dip of the subducting plate is approximately 10 degrees near the coast, steepening to roughly 40 degrees by the time it passes the Cascade Range (McCrory et al., 2006, Roth et al., 2008). As the subducting plate is only 8-9 Mya at the trench, it is expected to release much of its fluid budget in the forearc. The hydrated metabasalt of the upper crust will eclogitize at a depth of approximately 40 km in Cascadia (Hacker et al., 2003b), although structural and mineral heterogeneities will spread this out over a range of depths (Kirby et al., 2006). Hydrated mantle phases such as serpentine and chlorite will remain stable to depths of more than 90 km in Cascadia (Hacker, 2003b) and have been implicated in arc magma generation (Hattori and Guillot, 2003).

Although consisting of fewer than 30 high peaks, the Cascade Range numbers more than 2300 Quaternary vents, distributed in such a way as to suggest segmentation along-strike (Hildreth, 2007). The most abrupt along-strike transition occurs in central Washington, just to the north of Mt. Rainier and is

bisected by our MT station profile (Fig 1.) To the north of our line there is a gap of 120 km to the Glacier Peak vent cluster, which marks the southern end of the

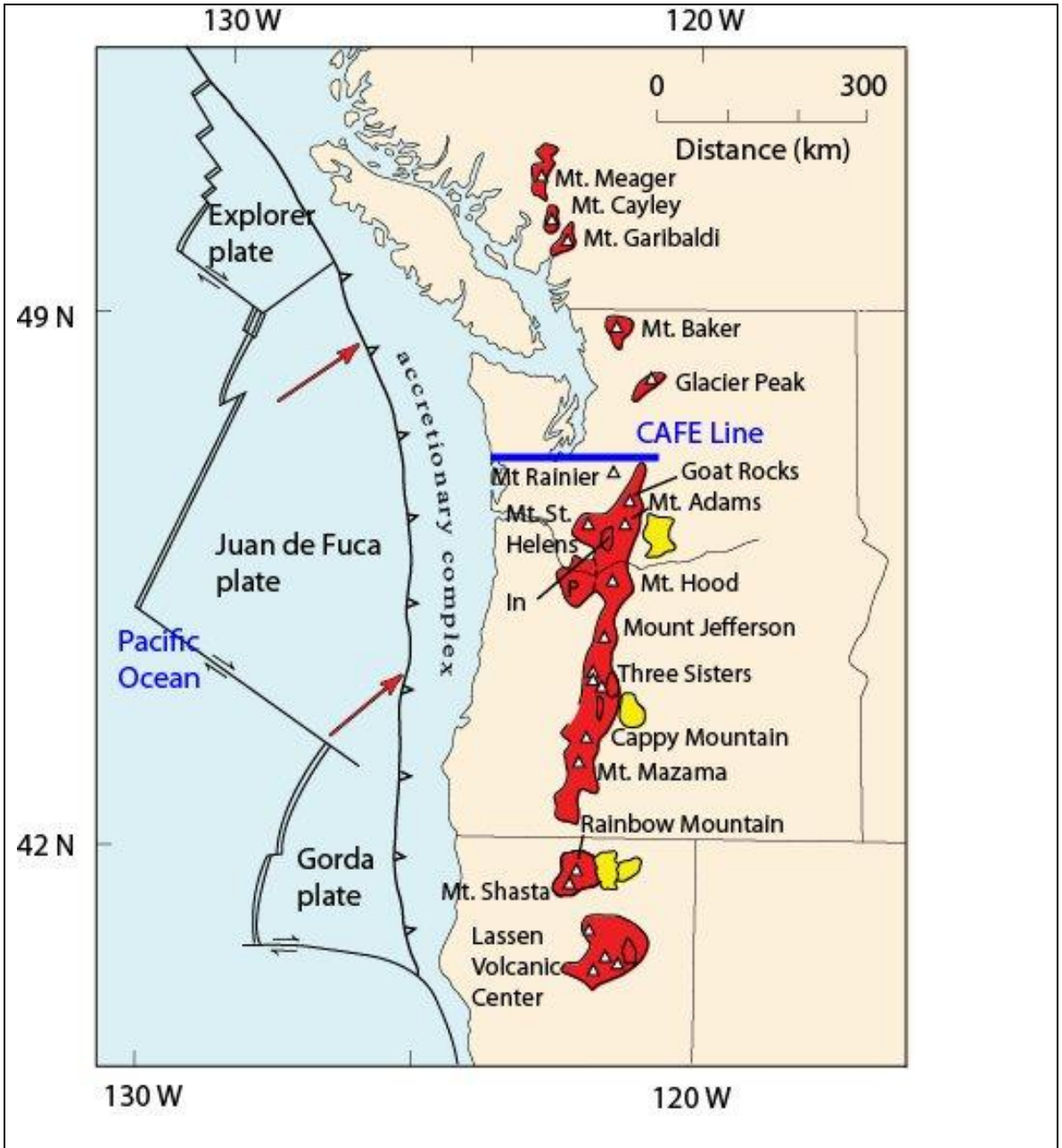

Fig 1: Regional map showing the CAFE MT line for the present study in relation to the Cascadia volcanic arc. Red indicates regions where forearc and arc vents are found, and back arc vent regions are indicated in yellow. P is the Portland vent field, and In the Indian Heaven vent field. (Adapted from Hildreth, 2007)

Garibaldi Volcanic Belt (GVB). The GVB consists of 127 Quaternary vents clustered around five tall stratovolcanoes (Hildreth, 2007) extending in a line roughly 30 degrees west of north. In contrast, an array of more than 150 Quaternary vents with no gaps greater than 10 km between them extends roughly 10 degrees west of south for 170 km to Mt. Hood (Hildreth, 2007). While most of the volcanic activity takes place in the approximately linear axial volcanic belt, the region of our study and to the immediate south of our line is notable for a significant presence of forearc volcanism, which is not found elsewhere in Cascadia (Hildreth, 2007). This includes Mt. Rainier and Mt. St. Helens in addition to the Indian Heaven and Portland vent fields.

The CAFE MT experiment consisted of a dense linear array of 60 wideband and 20 long-period magnetotelluric instruments extending approximately 280 km from the Washington State coast north of Grays Harbor, passing to the south of Puget Sound and Tacoma, within the northern boundary of Mt. Rainier National Park, and ending about 25 km east of Ellensburg (Fig.2). The wideband stations were spaced at distances of 5 km or less, and the target spacing for the long-period stations was 15 km. The CAFE MT experiment was designed to be collocated with the earlier CAFE dense array of passive seismic stations (Fig. 2) in order to utilize constraints from migrated images obtained during that phase (Abers et al., 2009, McGary et al., submitted).

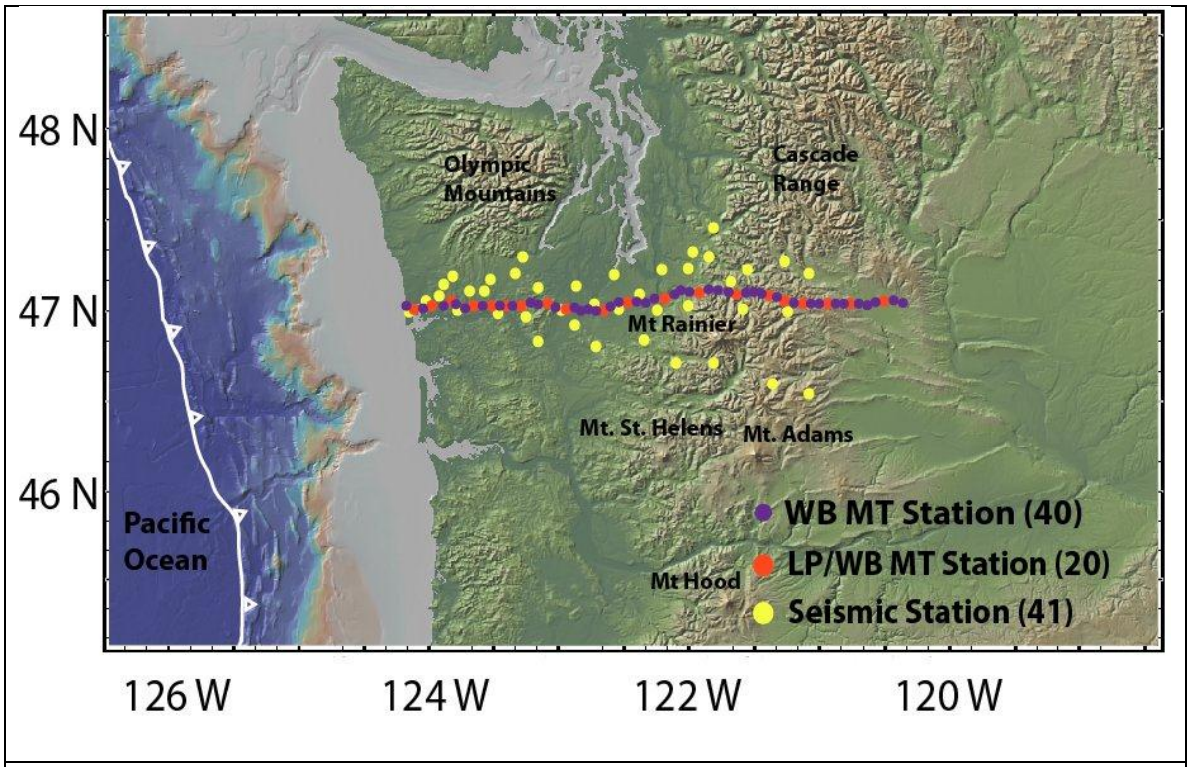

Fig 2: Map showing the location of the stations for the CAFE MT and seismic studies.

2. Fluids in subduction settings

The composition of a subducting slab can be idealized into four distinct layers. The upper crust consists of hydrated, fine-grained pillow basalts and sheeted dikes, underlain by a locally hydrated, coarse-grained, low porosity gabbroic lower crust. Below this we find a locally hydrated harzburgite/dunite uppermost mantle, and below that, an essentially anhydrous lower mantle layer of roughly lherzolite composition. The extent to which the lower crust and upper mantle

are locally hydrated can vary dramatically depending on the conditions under which they were formed and transported to the subduction zone. This is particularly true with respect to faulting history, as faults can provide pathways for fluids to infiltrate these layers.

There are a number of reactions that occur within a subduction system that allow for the release of fluids from the descending slab. The first of these is the conversion of hydrated metabasalts in the upper crust to eclogite. This reaction is largely controlled by pressure in warm subduction settings (Preston et al., 2003, Rondenay et al., 2008), and occurs at depths starting at ~40-45 km for Cascadia. The fine grained basalts at the top of the crust eclogitize first, followed by the progressively more coarse sheeted gabbroic dikes below, so that the reaction actually occurs over a range of depths. A contribution from eclogitization of locally hydrated lower crust is possible here as well, extending the depth range further.

A second dehydration reaction that occurs within the subduction setting involves the release of fluids from serpentinized materials, including talc, brucite, serpentine, and chlorite. While talc and brucite are not stable at depth in Cascadia, the dehydration of serpentine is controlled largely by temperature, and occurs between 600-650^{o}C (Preston et al., 2003, Hattori and Guillot, 2003, Audet et al., 2010), while chlorite harzburgite is stable to temperatures approaching

800°C (Hacker et al., 2003a). Within the Cascadia subduction system, this generally corresponds to depths of 80-95 km (Hacker et al, 2003).

The introduction of serpentinized material to such depths in the subduction system can occur in a variety of ways. The antigorite serpentine and chlorite that form at the bottom of the mantle wedge can be dragged to depth by the movement of the subducting slab (Hattori and Guillot, 2003, Kawakatsu and Watada., 2007), but the thermal profile for Cascadia excludes this possibility (van Keken et al., 2011). Serpentinized mantle rocks have also been identified in oceanic lithosphere at slow and intermediate rate spreading ridges, but only in regions where the axial valleys are well developed (Cannat, 1993), a condition that is not met for the southern Juan de Fuca ridge (Canales et al., 2005, Carbotte et al., 2006).

For Cascadia, any hydration of mantle rocks is likely the result of fluid intrusion that occurs due to the reactivation of the normal faults formed at the spreading center. These faults have been shown to reactivate and provide fluid transport pathways into the lower crust and uppermost mantle during bending at the trench (Ranero et al., 2005, Key et al., 2012), but for Cascadia, the shallow dip angle (McCrory et al., 2006) and the hydraulic barrier presented by the thick sediment layer at the trench (Divens et al., retrieved, 2012) are formidable obstacles to hydration in this manner. Hydrated mantle rocks have been

identified in Cascadia as a consequence of reactivation of faults within potential weak zones corresponding to wake propagation (Nedimovic et al, 2009), and have been implicated as the cause of the 2001 magnitude 6.8 Nisqually earthquake (Kao et al., 2008).

The coarse grained, non-porous gabbros of the lower crust may also transform directly to eclogite, a reaction which can occur at depths of 85 to 110 km for Cascadia (John and Schenk, 2003), but this reaction tends to be very sluggish in the absence of free water (Hacker et al., 2003b). A key catalyst is fluid access to pathways within the lower crust, therefore it is expected that dehydration reactions of serpentine and chlorite in the underlying upper mantle would accelerate this process (John and Schenk, 2003).

Fluids released during these hydration reactions migrate upwards into the overlying mantle wedge, where their presence lowers the melting temperature of the mantle rock potentially leading to flux melting. The combination of the thermal conditions and the presence of fluids are thought to control the formation and distribution of arc volcanism (Grove et al., 2009).

3. Data and Processing

Time series data from 20 long-period and 60 wideband MT instruments were collected for the CAFE MT experiment. The long-period data were collected using NIMS instruments with each station in place for typically three weeks. The wideband data were collected by Quantec Geoscience Inc. using Phoenix Geosystems instrumentation, with a typical recording interval of 15 hours for each site. The 280 km long array through central Washington was designed to be roughly collocated with the earlier CAFE passive seismic experiment.

The time series data from each long-period station was visually inspected for breaks, trends, and signal to noise ratio, then windowed with data from two separate magnetic remote reference sites. One remote reference for each station was selected from distant CAFE MT stations, and the second concatenated from Earthscope/US Array stations in Nevada and California that were operated concomitantly. The minimum distance between the primary station and the second remote was greater than 500 km, giving confidence that the noise between the stations was not likely to be correlated to any significant degree. Dual remote references were also used for the wideband data, with one remote reference located approximately 30 km east of Mt. Rainier, and a distant remote reference located at Buena Vista Valley, Nevada.

The long-period time series data were processed into impedance tensors using the robust bounded influence BIRRP algorithm (Chave and Thompson, 2003,

2004). The wideband data were processed following the procedure of Egbert and Booker (1996). The long-period transfer functions provided useful data from 10 seconds up to several thousand seconds, and the wideband from less than one second up to several hundred seconds. The data were collected during a low solar cycle, and were also affected by local noise, particularly near the cities of Olympia and Tacoma, so the period range of the useful data was not as long as it might have been otherwise. Samples of both the long-period and wideband transfer functions are shown below (Fig. 3). For the inversions, these data were supplemented with transfer functions from four stations that were part of the Earthscope US Array in Washington.

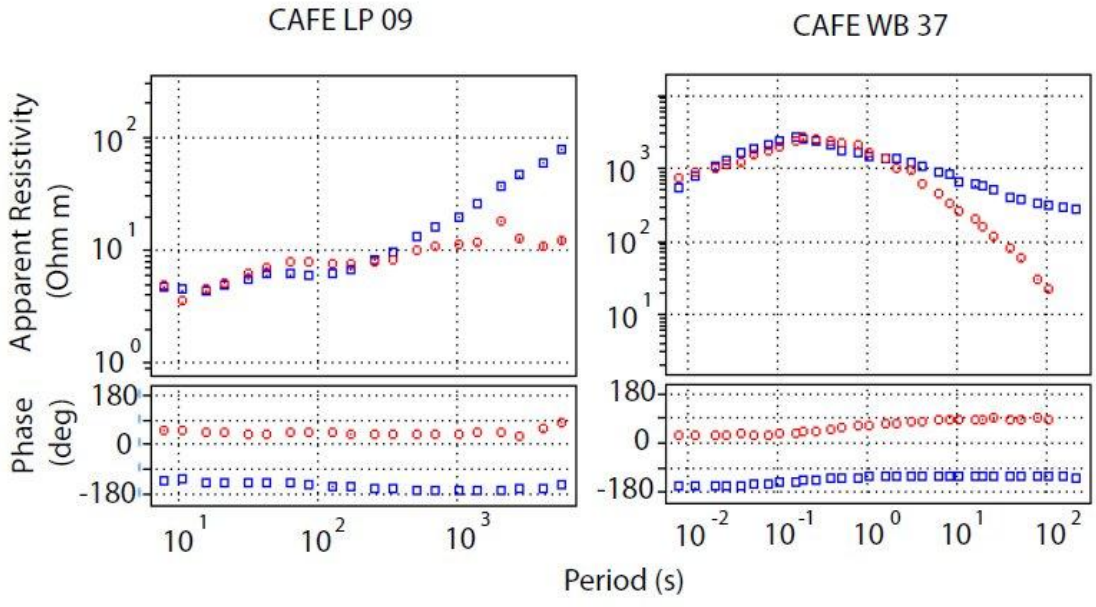

Fig 3: Sample transfer functions for a long period station (LP 09) and a wide band station (WB07)

After correcting the data for declination, dimensionality and regional strike direction were evaluated for the data in a variety of ways, including phase tensor analysis (Caldwell et al., 2004), Bahr skew analysis (Simpson and Bahr, 2005), and multisite, multifrequency Groom-Bailey tensor decomposition using the Strike software package (McNeice and Jones, 2001, Groom and Bailey, 1989). The phase tensor ellipses (Fig. 4) show a consistent pattern for periods between 20 and 2000 seconds, with a near north-south strike for stations west of Mt. Rainier, shifting to a slightly clockwise strike to the east of Mt. Rainier, with a more pronounced clockwise change for stations towards the eastern end of the profile. This is consistent with previous strike analysis conducted on a set of Earthscope LP stations along a line at roughly 46.5 N (Patro and Egbert, 2008).

Bahr (phase-sensitive) skew analysis provides a justification for a 2-D analysis of the data between the same periods, with exceptions beneath stations LP-32 and LP-36 (immediately west of Mt. Rainier) for periods greater than 400 seconds, and beneath stations LP-44 (just east of Mt. Rainier) and LP-54 (in a river valley just north of Ellensburg) for periods less than 150 seconds. It has been shown that while we can consider these exceptions as exhibiting 3-D characteristics, we cannot assume that the rest of the data can be considered 2-D based strictly on phase-sensitive skew analysis (Ledo et al., 2002).

The Groom-Bailey decomposition technique separates from the impedance tensor determinable matrices representing twist, shear, and anisotropy, leaving only distortion elements that affect both the amplitude and phase of the electric

Fig 4: A map of the Pacific Northwest showing the CAFE long period stations as blue circles. The ellipses show the average direction of the phase tensor-ellipse for periods between 100 and 1340 seconds. (Caldwell et al., 2004).

field, and performs statistical analysis of the validity of the assumption of galvanic distortion (Groom and Bailey, 1989, Jones, 2012). The Strike algorithm (McNeice and Jones, 2001) is an extension to this decomposition that allows

determination of a best fitting strike direction for multiple sites and over multiple frequencies. For the CAFE long-period data, a regional strike direction of seven degrees west of north provided the best chi-squared fit for the long-period data for periods of 100-1350 seconds, within confidence intervals when stations LP-32 and LP-36 were excluded. A strike direction of due north also produced an acceptable fit, and was used in the inversions (i.e. the data were decomposed but not rotated using the Strike algorithm). The strike angles for the entire set of decomposed transfer functions are displayed in the form of a rose diagram (Fig. 5).

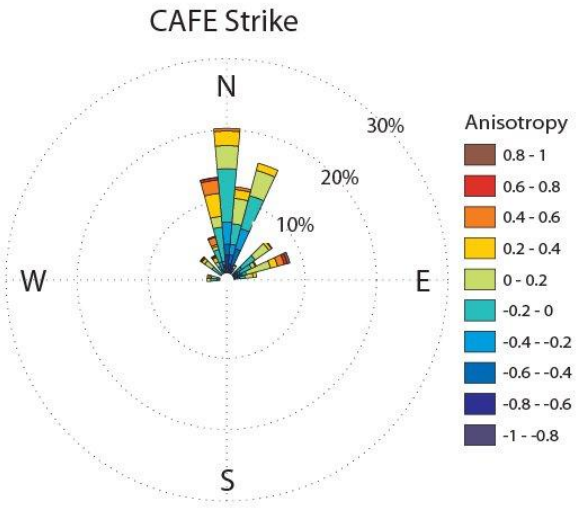

Fig 5: Rose diagram showing overall strike directions with the color code reflecting the degree of anisotropy as determined using the STRIKE algorithm for the CAFE data set (McNeice and Jones, 2001).

4. Modeling

Our 2-D inversion model assumes a primary strike direction of due north, consistent with the decomposition efforts described in the previous section. To generate our regularized 2-D models of resistivity structure, we used the non-linear conjugate gradient inversion algorithm WinGLink (Rodi and Mackie, 2001). The inversions were run starting with a half-space of 100 Ωm, except for the ocean, which was fixed at 0.33 Ωm with an extent defined by local bathymetry. The inversion mesh consisted of 116 rows and 234 columns. The row height was very fine near the surface, increasing gradually with depth, while the column width was maintained to be generally uniform as allowed by the station spacing.

The inversion process is iterative and attempts to minimize a Tikhonov objective function, which can be expressed as:

$$\Psi(m) = (d - F(m))^T V^{-1} (d-F(m))+\lambda m^T L^T Lm \quad (1)$$

where F(m) is the forward modeling function and d the data vector (with each d_i representing the log apparent resistivity or phase for a given polarization, observations site, and frequency), V is a matrix that represents the variance of the

error vector, and λ is the (generally global) regularization parameter that balances the misfit term with the smoothness term L^TLm, which for our inversions is defined by the integral of the square of the Laplacian. In the WinGLink implementation of the inversion code, the tradeoff between smoothness and misfit is defined by the value τ (instead of λ), and the optimal value is determined by plotting rms misfit against model roughness. For our inversions a τ value of 3.3 was deemed to be optimal. Two other parameters, α and β, define the relationship of the smoothness parameter in the vertical as compared to the horizontal, and the way in which the smoothness changes with depth respectively. A range of values from 0.8 to 1.8 for α and 1.0 to 2.0 for β were evaluated, with final selected values of α=1.5 and β=1.7. While small changes in α and β have been shown to produce striking differences in structure in some cases (Matsuno et al., 2011), the changes that we saw in structure while varying these parameters was quite minimal.

Transfer functions for a 2-D MT inversion consist of impedance and phase information over a range of frequencies, for two perpendicular modes, the transverse magnetic (TM) and transverse electric (TE). We can additionally utilize the tipper function, which relates the horizontal magnetic field information to the vertical magnetic field. The relationship between these parameters can be expressed as in equation 1,

$$\begin{bmatrix} E_x \\ E_y \\ B_z \end{bmatrix} = \begin{bmatrix} Z_{xx} & Z_{xy} \\ Z_{yx} & Z_{yy} \\ T_{zx} & T_{zy} \end{bmatrix} \begin{bmatrix} B_x \\ B_y \end{bmatrix} \quad (2)$$

where E_x and E_y are the two perpendicular horizontal components of the electric field, and B_x, B_y, and B_z are the two perpendicular horizontal components and the vertical component of the magnetic field. The Z components represent the complex impedences (apparent resistivity and phase) with the caveat that Z_{xy} and Z_{yx} are zero with the correct rotation of x and y for an ideal two dimensional subsurface. The components of the tipper function are shown as T_{zx} and T_{zy}.

We generated models that inverted both the TM and TE modes, with error floors of 5% and 15% respectively, and a set of models using only the TM mode, which has been shown to be less influenced by, and therefore more robust to the effects of 3D structure (Wannamaker et al., 1989). The tipper function was included in both sets of inversions.

We also evaluated the extent to which the primary structures in our models were supported and/or required by the data. This was done in a number of ways, such as assessing how the structures were affected by parameter modifications such as changes to the variables controlling global smoothness (i.e.

τ, α, and β described above), and comparing the resulting models to the data pseudo sections to give us a better understanding of how data from each station might be affecting the inversion.

Additionally, manual editing techniques were utilized. This involved removing or altering a feature in the resultant model and then allowing the inversion process to seek a solution optimally close to this altered model. If the feature was restored by the inversion, it was taken to be required by the data. If the inversion was able to achieve a misfit comparable to the original misfit without restoring the feature, the structure in question was determined to be allowed but not required by the data.

Finally, in order to assess the inverted image as a whole, we generated a set of synthetic station data from the inverted images, and then performed a series of inversions using the synthetic data and starting from our 100 Ωm half-space model with fixed resistivity for water. We should expect that if the inverted image were completely correct, the inversion of the synthetic data would faithfully reproduce the image, whereas variations between the images can provide important information regarding the limitations of the inversion. This idea will be discussed in more detail in section 6.

5. Results

Figures 6a (top) and 6b (bottom) show our primary inversion models. The image in figure 6a was generated using only the TM mode along with the tipper, while the image in figure 6b also included the TE mode in the inversion. The

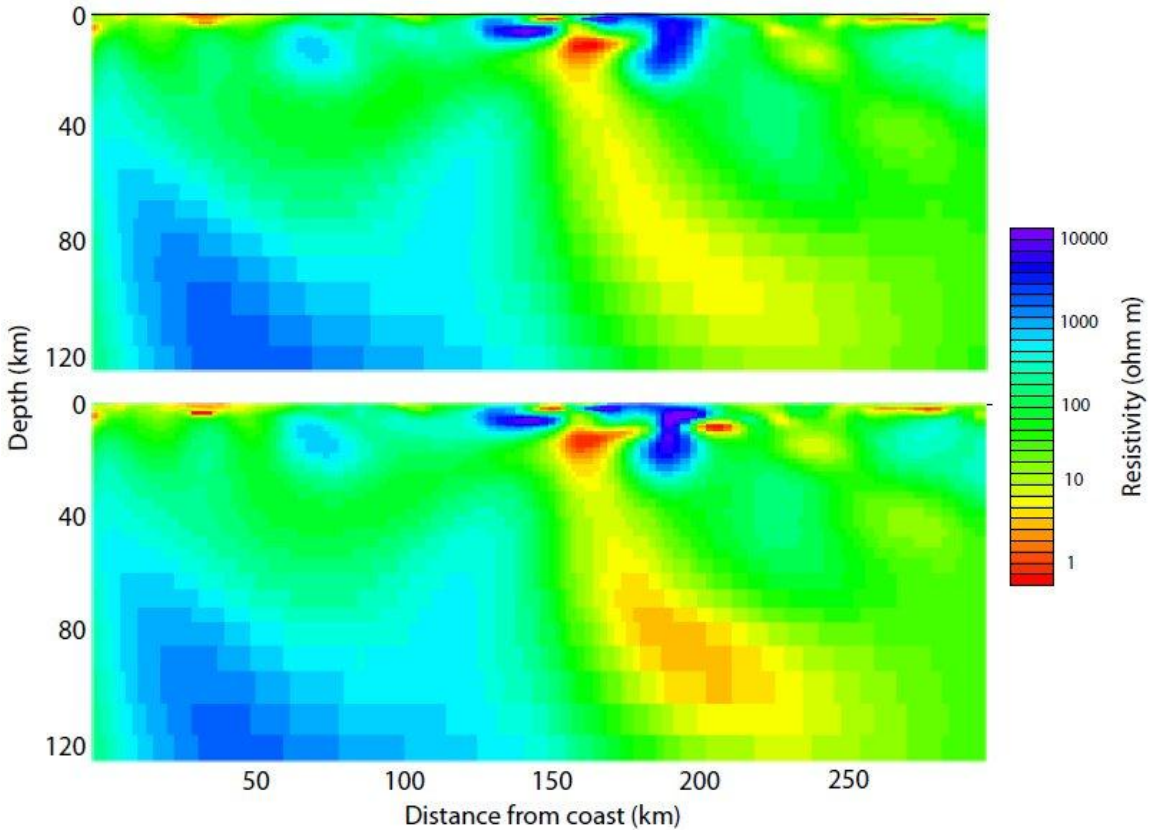

Figure 6: This figure shows the primary inversion images for the CAFE data. The top image was generated using just the TM mode and the tipper function data, while the bottom image included the TE mode data

two inversions produce images that are very similar, a conclusion supported by generating pseudo-sections from each of the inversion models, and differencing them to see the contrast. Differences in the apparent resistivities in the models

never exceeded 10%, and differences in the phases remained less than 2° everywhere. Despite this similarity, the rms misfit for the TM/TE/tipper model is 3.03, significantly higher than that for the TM/tipper model at 1.96. This suggests that both inverted images were driven primarily by the TM and tipper data.

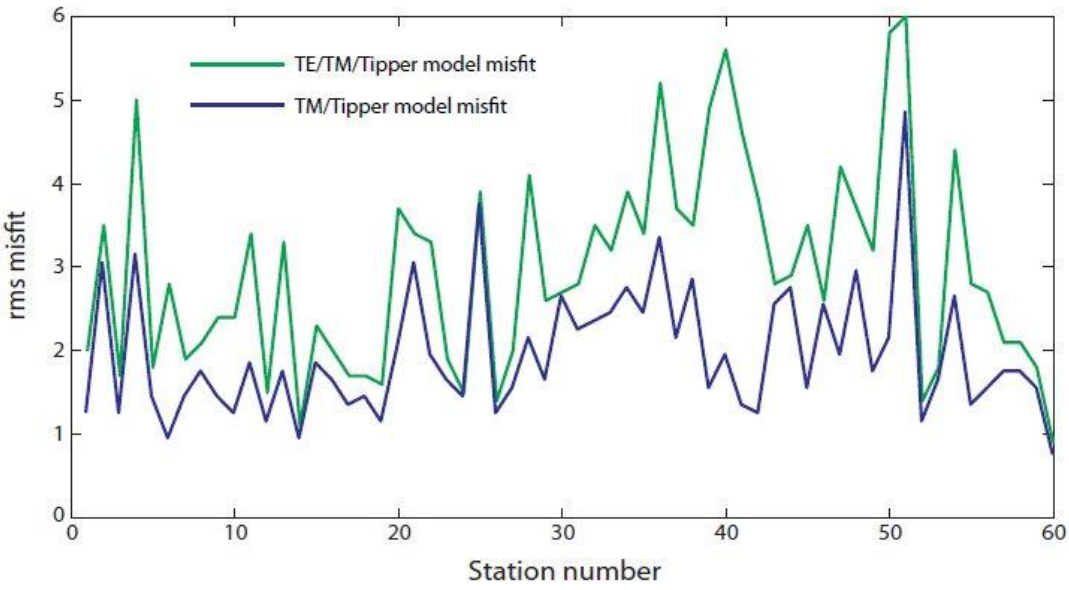

Figure 7: The rms misfit for each of the inversion models is plotted for each station. The TM mode/tipper model misfit is plotted in blue, and the misfit for the model including the TE mode is plotted in green.

Figure 7 shows plots of rms misfit value by station for each of the inversion models. For the most part, the shapes of the plots are similar, with the rms misfit values staying fairly close between models (though they are consistently higher for the TM/TE/tipper inversion). The clear exceptions to this are between stations 6-10, corresponding to the western part of the Willapa Valley, and between stations 36 and 42, corresponding to the vicinity of Mt. Rainier, where

the increasing misfit of the TM/TE/tipper inversion is contrasted by a steady or decreasing misfit for the TM/tipper only inversion. While it might be tempting to invoke 3D effects, this is not consistent with the Bahr skew and strike analyses. This discrepancy has more to do with our standard choice of a globally smooth halfspace model, which will be examined in detail in Chapter 4. For the time being we will set this aside, and continue with our interpretation of the TM/TE/tipper inversion model.

Shallow features

There are three shallow conductors in the inversion cross-sections (Fig. 8) that correspond to sediment basins along the transect. The first (A1) occurs in the Willapa Valley, between the coastal Grays Harbor region and the uplifted Black Hills. The second (A2) corresponds with the quaternary glacial deposits (Schuster, 2007) in the forearc basin, and the third (A3) with the quaternary sediments in the backarc basin. These shallow conductors are typical of those previously found during MT work in other subduction settings (Soyer and Unsworth, 2006, Brasse et al., 2009, Evans et al., submitted).

A highly resistive crust (B) measuring several hundreds to a few thousand Ωm underlies Rainier National Park, consistent with the presence of the dry

pyroxene-andesite-dacite complex that makes up most of the volcanic basement (Simpson and Bahr, 2005, Hildreth, 2007). Resistivities in the Western Cascades

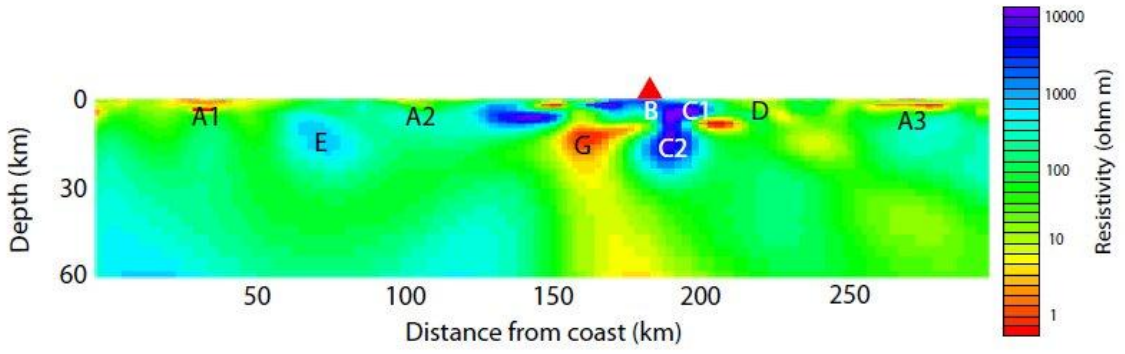

Figure 8: The upper 60 km of the conductivity structure for the CAFE line. The red triangle marks the location of Mt. Rainier just to the south of the profile. A1-A3 mark conductors associated with sedimentary basins. B, C1, and C2 are resistive features associated with Mt. Rainier and the Western Cascades. D is a conductive feature beneath the High Cascades. The resistor E is associated with the crustal forearc, and we interpret the strong conductor G as a magma chamber feeding Mt. Rainier.

(C1) are also in the thousands of Ωm , but drop off quickly into the High Cascades (D), where they range from roughly 10-100 Ωm. This transition in resistivity from the Western Cascades to the High Cascades has been shown to extend much of the length of the Cascade Range (Jiracek and Curtis, 1989, Wannamaker et al., 1989, Patro and Egbert, 2008), and is thought to indicate the presence of interconnected fluids (Wannamaker et al., 1989). This conductive feature dips towards the east, and appears to extend potentially all of the way to

the upper mantle, an observation that has also been previously reported (Patro and Egbert, 2008). Referred to as the Southwest Washington Cascades Conductor (SWCC), it is described as an upper crustal conductive anomaly just west of the Cascades, and it has been suggested that the deeper parts of this conductor may have a distinct cause such as fluids associated with subduction and arc magmatism (Patro and Egbert, 2008).

The crust in the forearc region (E) is generally quite resistive, from several hundred to more than a thousand Ωm, not quite as resistive as might be expected for a tectonically inactive upper crust (Nesbitt, 1993, Gough, 1986), but consistent with what has been observed in other subduction settings (Brasse et al., 2009). In Costa Rica, this discrepancy was attributed to fluid input derived from dehydration of the downgoing slab, and this conclusion is very strongly supported in the current case as well. We will examine this in more detail when we consider the inversion image within the context of previous passive seismic work in section 5.2.

The most striking feature within the crust is the strong conductor (G) located at depths from around 10 km roughly below Mt. Rainier. While much of the volcanic rock that makes up Mt. Rainier is pyroxene-andecite-dacite, inclusions of more basaltic andesite are common and most likely represents the main parent magma in the crustal reservoir (Hildreth, 2007). These samples typically give an

SiO2 content of ~55%wt and Na2O content of ~3.5%wt (Stockstill et al., 2002). Assuming a typical water contribution of ~4%wt and a temperature of 1275 K consistent with the solidus for this magma, we would expect a resistivity of ~0.7 Ωm for a pure melt at 15 km depth (Pommier and LeTrong, 2007). The lowest resistivities in the model are ~0.85 Ωm, suggesting substantial pockets of high melt fractions (close to 100%). The specific distribution of conductivities within the anomaly is consistent with the existence of two pockets, a primary pocket to the west of Mt. Rainier at a depth of 15 km, and a secondary source at 10 km depth more directly beneath the volcano. The mixed and zoned eruptive history of Mt. Rainier has led others to argue for such multi-level reservoirs (Venezky and Rutherford, 1997, Stockstill et al., 2002). The primary reservoir clearly appears to be connected to a source in the mantle; we will consider this in more detail in section 5.2.

To the east of this conductor, the resistor underlying the Western Cascades can be seen to extend to or be connected to another resistive feature (C2) that extends to depths of 25 km. The resistivity of this feature is on the order of a few thousand Ωm, consistent with either tectonically inactive upper crust (Nesbitt, 1993, Gough, 1986) or intruded, cool, mafic igneous rock (Simpson and Bahr, 2005).

Deeper features

Previous work has shown that MT data is not always particularly sensitive to the structure within a subducting slab, sometimes showing a varying resistive feature that roughly coincides with the top of the slab (Soyer and Unsworth, 2005, Evans et al., submitted), and sometimes returning no commensurate resistive region at all (Matsuno et al., 2011). The unconstrained model in this study is an intermediate case, where a resistive feature is present (H in figure 9b), but does not strictly coincide with the top of the slab, and is also thicker than would be expected based on simple thermal considerations. This result is similar to those seen previously in Central America (Brasse et al., 2009), and the resistivity of more than 1000 Ωm is consistent with that expected for the slab (Bedrosian, 2007). We will explore some of the variables that affect the limitations of MT as regards defining the top of the resistive slab in Chapter 4, as well as some methods for minimizing these limitations, but for the time being we will use the results from the collocated passive seismic experiment (see Fig. 2 for stations) in Chapter 2 to constrain the location of the descending oceanic slab.

Figure 9a (top) shows the image generated using GRT migration of passive seismic data, as well as the interpretation of that image discussed in Chapter 2. Figure 9b (bottom) shows the TM/TE/tipper magnetotelluric inversion image

from Fig. 5b, but with the seismic interpretation superimposed to provide a framework for the discussion of the processes illuminated by the distribution of conductivities.

Starting at a depth of approximately 40 km and intersecting roughly with the top of the descending slab, we find the corner of a v-shaped conductor (F) with a resistivity consistently around 80 Ωm. This is similar to, though slightly more resistive than, features found at similar depths in other subduction zone studies (Brasse et al., 2011, Evans et al., submitted), where it has been interpreted as migrating fluids that have been released from the subducting oceanic crust. This interpretation is also strongly supported by the seismic work, as a velocity increase in the crust suggests a fluid release due to the transition of hydrated metabasalts to eclogite at this location.

The 80 Ωm resistivity is consistent with a 0.4%wt of saline fluids (consistent with seawater) given good connectivity (Pommier and LeTrong, 2007), with a tradeoff between higher fluid content and poorer connectivity also yielding acceptable results. The westward extension of the conductor follows the top of the slab for ~20 km before rising directly upward, apparently connecting with the eastern edge of the Willapa Bay sediments conductor. The eastern extension rises approximately 20 km over a horizontal distance of 40 km, and possibly

continuing along that path to eventually connect with the conductor (G) that we have interpreted as the magma chamber below Mt. Rainier.

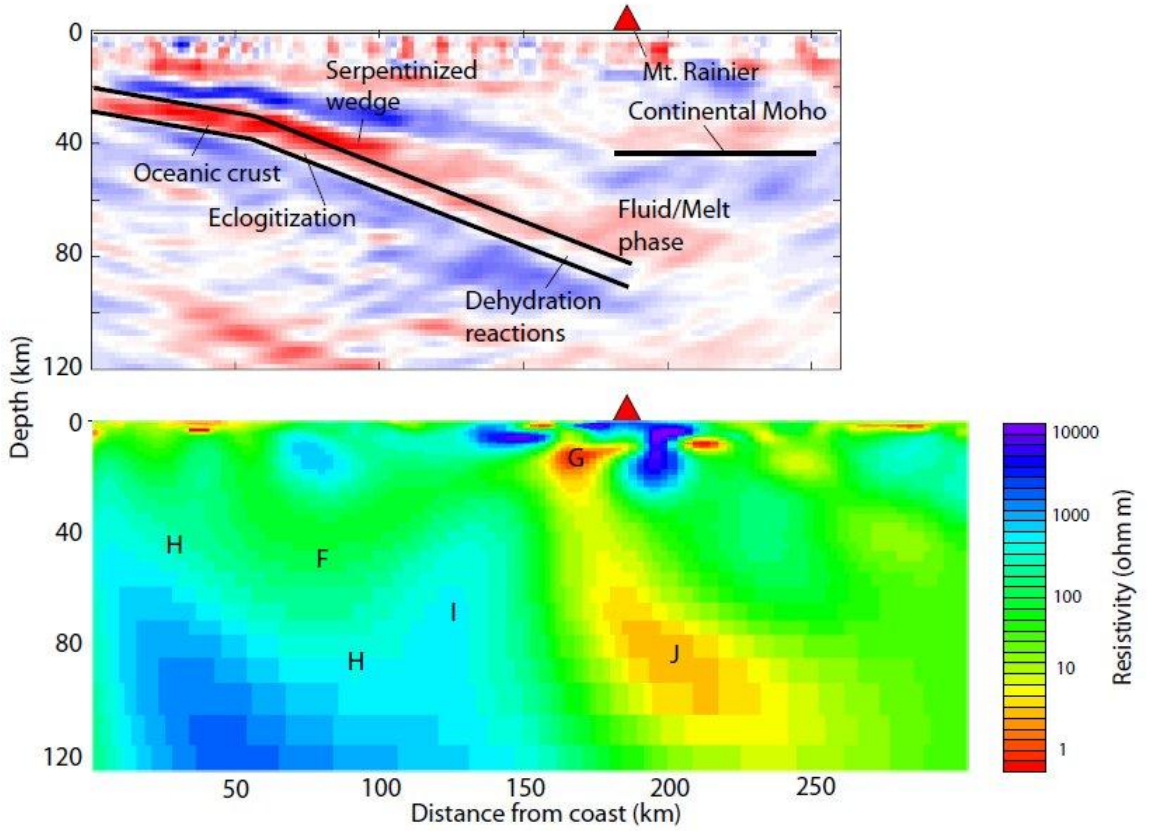

Figure 9: Figure 9a (top) shows the migrated passive seismic image from Chapter 2, including the interpretation. The MT model is shown in figure 9b (bottom). The resistors H and I are associated with the subducting slab and the cold nose of the mantle wedge, respectively. The conductive feature F shows the release of fluids from eclogitization of the upper crust, and the strong conductor J the fluids most likely with a component of flux melting associated with the deep fluid release.

Following the slab crust down to a depth of ~50 km, we encounter a feature (I) with a resistivity between 300-500 Ωm. Similar features have been encountered

in earlier subduction zone MT studies (Soyer and Unsworth, 2005, Brasse et al., 2009). The conductivities are consistent with either mantle minerals or antigorite serpentine with a well connected fluid phase of less that 1%wt (Reynard et al., 2001, Pommier and LeTrong, 2007), but also with dry peridotite at the temperatures expected in the wedge. This is consistent with the seismic image, as this resistor corresponds to the section of mantle wedge that does not get significant fluid input from slab dehydration.

Following the top of the slab to a depth of ~80 km, we encounter a large and rather intense conductor (J), with resistivities as low as 2 Ωm. The bottom of this conductor appears to coincide with the top of the slab and connect with the shallow conductor (G) that we interpreted as a magma chamber. The implication is that this conductor represents melt caused by flux melting as a consequence of fluid release from a depth of 80-100 km, and that this melt provides the source for the magma chamber that supplies Mt. Rainier. A basaltic andesite magma of the type inferred to be the source magma for Mt. Rainier (Stockstill et al., 2002, Hildreth, 2007), at a temperature of 1300 K and pressure of 2.4 MPa would have a resistivity as low as 0.6 Ωm for a pure melt with a 4%wt water content (Pommier and LeTrong, 2007), which is consistent with the most conductive area of the feature, and suggests partial melting in the upward extension that feeds the crustal magma chamber. The most conductive zones of the anomaly are also

coincident with the low velocity region in the seismic image that we interpreted as a fluid melt phase based on independent seismic, hypocenter, and petrological evidence in Chapter 2. The conductive feature appears to be entirely consistent with the interpretation in that chapter, specifically that the dehydration of serpentine and chlorite harzburgite in the upper mantle releases substantial fluid, triggering a chain reaction which transforms the metastable gabbros in the lower crust into eclogite. The released fluids migrate into the overlying continental mantle, leading to flux melting and the formation of a significant magma source. This magma source feeds the crustal level chamber or chambers that in turn provide source magma for Mt. Rainier. The evidence from the three seismic lines and the hypocenter locations of deep earthquakes (addressed in detail in Chapter 2) suggest that this mechanism is not ubiquitous along the strike of the Cascades. This is not unexpected, however, as Mt. Rainier is a forearc volcano some 50 km to the west of the active Cascade arc, meaning that our interpretation would be supported should similar features be discovered in the vicinity of Mt. St. Helens, the only other major forearc volcano in the Cascades.

6. Assessment of the model

Each of the key features discussed in section 5 were subject to a number of sensitivity tests in order to determine if, within the context of the remaining structures, they were required by the data. This was done by removing or changing a feature and then allowing the inversion code to seek a solution optimally close to this altered model. If the solution was unable to achieve a similar or better misfit or if the feature was simply restored by the inversion, we concluded that the original feature is required by the data.

We also generated a set of synthetic data from our final model, and then performed a series of inversions using the synthetic data in place of the real processed data. The inversions were produced using the same basic 100 Ωm halfspace with a 0.33 Ωm ocean determined by bathymetry that we used for the original models. If our original model were a completely correct representation of the subsurface, we should expect that the inverted image using the synthetic data would faithfully reproduce the original model. Of course, the model will never be perfect, and in this case we had reason to suspect places where the reproduction would highlight flaws given the mismatch between the rms misfits for the TM/tipper and TM/TE/tipper inversions.

The model generated from the synthetic data is compared to the original inversion model in figure 10, and at a glance it is clear that all of the primary features of the original model are reproduced. This gives us confidence that our model is, at least in general, largely correct. Despite this, there are some clear differences between this model and our primary model.

First, the conductor that we interpreted as the magma chamber beneath Mt. Rainier is much less defined in the synthetic reproduction. The implication is that details in the structure of a conductive feature can be lost during the inversion process. This suggests that the actual distribution of the conductor in the subsurface might be more complicated than that in our model, an idea that we will explore in more detail in Chapter 4.

The conductor below the High Cascades, while still present in the synthetic model, shows not only a loss of detail, but the evidence for the connection between this conductor and the conductive mantle to the east is much less convincing.

The V-shaped conductor in the west that we interpreted as fluids released during the eclogitization of the hydrated basalts in the upper crust has also lost its shape, smearing out along a horizontal line at a depth of ~50 km. The shape of the underlying resistive feature has also been altered. We would expect that

the actual conductivity structure of fluids being released from the upper crust of a slab to be represented by a conductor rising from the top of a strong resistive

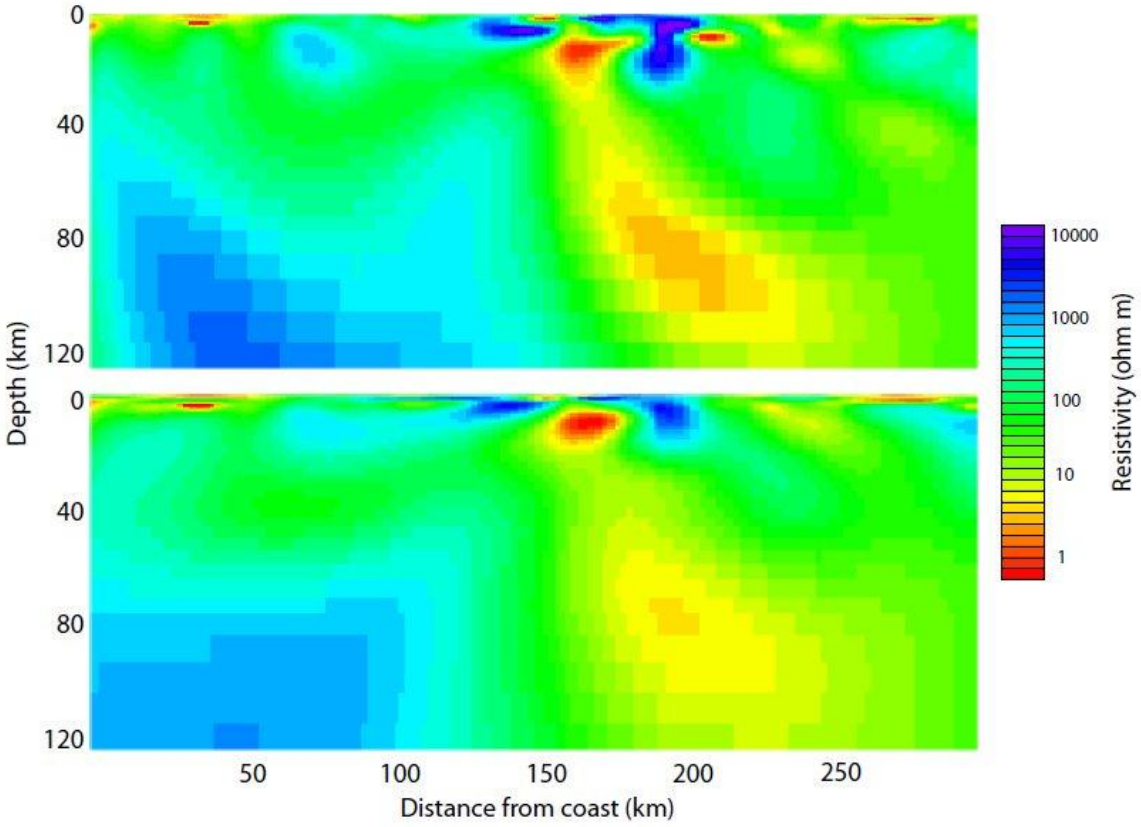

Figure 10: This figure compares the original inversion model (top) with the model using synthetic data (bottom). The synthetic data is generated using the original inversion model as the forward model.

feature, and while the inversion is consistent with this, the location of the interface is not clearly identified in the inversion.

Finally, the large conductor that we interpret as the fluid release from serpentinization at ~ 80-100 km depth is both more compact and less intense in the model generated from synthetic data. It is also worth noting that in this

model, the resistor to the west that would represent the slab material has retreated from the conductor. This is another situation where we would expect a strong conductor and a resistor to be essentially in contact, and again the inversion does not clearly identify the location of the expected interface. Instead, the smoothness parameter forces the resistor and conductor to separate, and in releasing the contrast, weakens the intensity of both features. We also notice that the most intense region of the conductor in both inversions is centrally located within the conductor, when we would expect to find it closer to the top of the subducting slab.

In Chapter 4, we will examine the mechanisms underlying each of these phenomena, and also look for ways to apply this information within the inversion process to more faithfully reproduce the underlying conductivity structure. In the end, we will generate an inversion model that is a better fit to the data, particularly for the trouble spots corresponding to stations 6-10 and 36-42, show that this model is more robust, and improve our understanding of the subduction system beneath Central Washington.

7. Conclusion

We have generated 2-D resistivity models of the Cascadia subduction zone structure beneath central Washington State using electric and magnetic field data collected along a dense profile of 60 wideband and 20 long period magnetotelluric stations. The resulting images show a conductive feature near the slab at a depth of ~40 km that is consistent with a fluid release due to eclogitization reactions in the upper crust that have also been detected by a collocated seismic study. A second, more intense conductive feature is identified near the slab at a depth of ~80 km, consistent with a fluid/melt phase associated with the dehydration of chlorite and serpentine in the upper mantle and the transition of metastable gabbros to eclogite in the lower crust of the descending slab. This conductor extends upward to depths of less than 30 km, where it connects with an intense conductor that is consistent with a magma chamber below a strong resistive feature consistent with the location of Mt. Rainier.

High resistivities are found beneath the Western Cascades, dropping off quickly beneath the more recently active High Cascades to the east. Three additional shallow conductive features correspond with sedimentary basins along the transect.

While sensitivity tests and comparison with previous seismic work give us confidence in the robustness and accuracy of the primary features in the model, we also have ample evidence to suggest that some of the details might be better

resolved. These issues will be addressed from both a theoretical and practical standpoint in the following chapter.

References for Chapter 3

Abers, G.A., MacKenzie, L.S., Rondenay, S., Zhang, Z., Wech, A.G., Creager, K.C., 2009. Imaging the source region of Cascadia tremor and intermediate-depth earthquakes. Geology 37, 1119-1122.

Audet, P., Bostock, M.G., Boyarko, D.C., Brudzinski, M.R., Allen, R.M., 2010. Slab morphology in the Cascadia fore arc and its relation to episodic tremor and slip. J. Geophys. Res. 115, B00A16.

Bedrosian, P.A., 2007. MT+, Integrating magnetotellurics to determine Earth structure, physical state, and processes. Surv. Geophys., DOI 10.1007/s10712-007-9019-6.

Brasse, H., Kapinos, G., Mutschard, L., Alvarado, G.E., Worzewski, T., Jegen, M., 2009. Deep electrical resistivity structure of northwestern Costa Rica. Geophys. Res. Lett., v. 36, L02310, doi:10.1029/2008GL036397.

Canales, J.P., Detrick, R.S., Carbotte, S.M., Kent, G.M., Diebold, J.B., Harding, A., Babcock, J., Nedimovic, M.R., van Ark, E, 2005. Upper crustal structure and axial topography at intermediate spreading ridges: Seismic constraints from the southern Juan de Fuca Ridge. J. Geophys. Res., v.110, B12104, doi:10.1029/2005JB003630.

Cannat, M., 1993. Emplacement of mantle rocks in the seafloor at mid-ocean ridges. J. Geophys. Res. 98, 4163-4172.

Carbotte, S.M., Detrick, R.S., Harding, A., Canales, J.P., Babcock, J., Van Ark, E., Nedimovic, M., Diebold, J., 2006. Rift topography linked to magmatism at the intermediate spreading Juan de Fuca ridge. Geology 34, 209-212.

Caldwell, T.G., Bibby, H.M., Brown, C., 2004. The magnetotelluric phase tensor. Geophys. J. Int., 158, 457-469.

Chave, A.D., and Thompson, D.J., 2004. Bounded influence magnetotelluric response function estimation. Geophys. J. Int., 988-1006.

Egbert, G.D., 1997. Robust multiple station magnetotelluric data processing. Geophys. J. Int., 130, 475-496.

Evans, R.L., Wannamaker, P., McGary, R.S., Elsenbeck, J., submitted 2012. Electrical structure of the Central Cascadia subduction zone: The EMSLAB Lincoln line revisited.

Fluck, P., Hyndman, R.D., Wang, K., 1997. Three-dimensional dislocation model for great earthquakes of the Cascadia subduction zone. J. Geophys. Res. 102, 20539-20550.

Gough, D.I., 1986. Seismic reflectors, conductivity, water and stress in the continental crust. Nature, v. 323, 143-144.

Groom, R.W., and Bailey, R.C., 1989. Decomposition of magnetotelluric impedance tensors in the presence of local three-dimensional galvanic distortion. J. Geophys. Res., 94, 1913-1925.

Grove, T.L., Till, C.B., Lev, E., Chatterjee, N., Medard, E, 2009. Kinematic variables and water transport control the formation and location of arc volcanoes. Nature, 459, 694-697.

Hacker, B.R., Abers, G.A., Peacock, S.M., 2003a. Subduction factory 1. Theoretical mineralogy, densities, seismic wave speeds, and H_2O contents. J. Geophys. Res. 108(B1), 2029, doi:10.1029/2001JB001127.

Hacker, B.R., Peacock, S.M., Abers, G.A., 2003b. Subduction factory 2. Are intermediate-depth earthquakes in subducting slabs linked to metamorphic dehydration reactions? J. Geophys. Res. 108(B1), 2030, doi:10.1029/2001JB001129.

Hattori, K.H., Guillot, S., 2003. Volcanic fronts form as a consequence of serpentine dehydration in the forearc mantle wedge. Geology 31, 525-528.

Hildreth, W., 2007. Quaternary magmatism in the Cascades- Geologic perspectives, USGS professional paper 1744.

Jiracek, G.R., Curtis, J.H., Ramiriz, J., Martinez, M., Romo, J., 1989. Two-dimensional magnetotelluric inversion of the EMSLAB Lincoln line, J. Geoph. Res., 94, 14,145-14,151.

John T., Schenk, V., 2003. Partial eclogitization of gabbroic rocks in a late Precambrian subduction zone (Zambia): prograde metamorphism triggered by fluid infiltration. Contrib. Mineral Petrol. 146, 174-191.

Jones, A.G. 2012. Distortion decomposition of the magnetotelluric impedance tensors from a one-dimensional anisotropic Earth.
Geophys. J. Int., 189, 268-284, doi: 10.1111/j.1365-246X.2012.05362.x.

Kao, H., Wang., K., Chen, R. –Y., Wada, I., He, J., Malone, S.D., 2008. Identifying the rupture plane of the 2001 Nisqually, Washington earthquake. Bull. Seis. Soc. Am., 98, 1546-1558.

Kawakatsu, H., Watada, S., 2007. Seismic evidence for deep-water transportation in the mantle. Science 316, 1468-1471.

Key, K., Constable, S., Matsuno, T., Evans, R.L., Myer, D., 2012. Electromagnetic evidence for plate hydration due to bending faults at the Middle America Trench, Earth and Planet. Sci. Letts., 351-352, 45-53.

Kirby, S., Engdahl, E.R., Denlinger, R., 1996. Intermediate-depth intraslab earthquakes and arc volcanism as physical expressions of crustal and uppermost mantle metamorphism in subducting slabs, in Bebout, G., et al., eds., Subduction top to bottom: American Geophysical Union Geophysical Monograph 96, 195-214.

Klemd R., John, T., Scherer, E.E., Rondenay, S., Gao, J., 2011. Changes in dip of subducted slabs at depth: Petrological and geochronological evidence from HP-UHP rocks (Tianshan, NW-China). Earth Planet. Sci. Lett. 310, 9-20.

Ledo, J., Queralt, P., Marti, A., Jones, A., 2002. Two-dimensional interpretation of three-dimensional magnetotelluric data: an example of limitations and resolution, Geophys. J. Int., 150, 127-139.

Matsuno, T., et al., 2010. Upper mantle electrical resistivity structure beneath the central Mariana subduction system, Geochem. Geophys. Geosyst., 11, Q09003, doi:10.1029/2010GC003101.

Mazzoti, S., and Adams, J., 2004. Variability of near-term probability for the next great earthquake on the Cascadia subduction zone. Bull. Seis. Soc. America, v. 94, 1954-1959.

McCrory, P.A., Blair, J.L, Oppenheimer, D.H., Walter, S.R., 2006. Depth to the Juan de Fuca slab beneath the Cascadia subduction margin- A 3-D model for sorting earthquakes. U.S. Geological Survey data series 91.

McGary, R.S., Rondenay S., Abers, G., submitted 2012. Imaging the transition of metastable gabbro to eclogite.

McNeice, G.W., and Jones, A.G., 2001. Multisite, multifrequency tensor decompositions of magnetotelluric data. Geophysics, 66, 158-173, 2001.

Miller, M.M, Johnson, D.J., Rubin, C.M., Dragert, H., Wang, K., Qamar, A., Goldfinger, C., 2001. GPS-determination of along-strike variation in Cascadia margin kinematics: Implications for relative plate motion, subduction zone coupling, and permanent deformation. Tectonics 20, 161-176.

Nedimovic, M., Bohnenstiehl, D., Carbotte, S., Canalas, J.P., Dziak, R., 2009. Faulting and hydration of the Juan de Fuca plate system. Earth Planet. Sci. Lett. 284, 94-102.

Nesbitt, B.E., 1993. Electrical resistivities of crustal fluids. J. Geophys. Res., 98, 4301-4310.

Patro, P.K., and Egbert, G.D., 2008. Regionala conductivity structure of Cascadia: Preliminary results from 3D inversion of USArray transportable array magnetotelluric data. Geophys. Res. Lett., v35, L20311.

Pommier A. and LeTrong E., 2011. "SIGMELTS": A web-portal for electrical conductivity calculations in geosciences. Computers and Geosciences, doi:10.1016/j.cageo.2011.01.002.

Preston, L.A., Creager, K.C., Crosson, R.S., Brocher, T.M., Trehu, A.M., 2003. Intraslab earthquakes: Dehydration of the Cascadia Slab. Science 302, 1197-2000.

Ranero, C.R., Villasenor, A., Phipps-Morgan, J., Weinrebe, W., 2005. Relationship between bend-faulting at trenches and intermediate-depth seismicity. Geochem. Geophys. Geosyst. 6(12), 1-25.

Reynard, B., Mibe, K., Van de Moortele, B., 2011. Electrical conductivity of the serpentinized mantle and fluid flow in subduction zones. Earth Planet. Sci. Lett. 307, 387-394.

Rodi, W., and Mackie, R. L., 2001. Nonlinear conjugate gradients algorithm for 2-D magnetotelluric inversion. Geophysics, 66, 174-187.

Rondenay, S., Abers, G.A., van Keken, P.E., 2008. Seismic imaging of subduction zone metamorphism. Geology 36, 275-278.

Roth, J.B., Fouch, M.J., James, D.E., Carlson, R.W., 2008. Three-dimensional seismic velocity structure of the northwestern United States. Geophys. Res. Lett. 35, L15304.

Schuster J.E., 2007. Geologic map of Washington State (MAP), Washington State Department of Natural Resources

Simpson F., and Bahr, K., 2005. Practical Magnetotellurics (BOOK). Cambridge University Press.

Soyer, W., and Unsworth, M., 2006. Deep electrical structure of the northern Cascadia (British Columbia, Canada) subduction zone: Implications for the distribution of fluids, Geology, v. 34, 53-56.

Stockstill, K.R., Vogel, T.A., Sisson, T.W., 2002. Origin and emplacement of the andesite of Burroughs Mountain, a zoned, large-volume lava flow at Mount Rainier, Washington, USA. J. Volcanology and Geothermal Res., 119, 275-296.

Ulmer P., Trommsdorff, V., 1995. Serpentine stability to mantle depths and subduction related magmatism. Science 268, 858-861.

van Keken, P.E., Hacker, B.R., Syracuse, E.M., and Abers, G.A., 2011. Subduction factory: 4. Depth-dependent flux of H_2O from subducting slabs worldwide. J. Geophys. Res. 116, B01401.

Venezky, D.Y., and Rutherford, M.J., 1997. Pre-eruption conditions and timing of dacite-andesite magma mixing in the 2.2 ka eruption at Mount Rainier. J. Geophys. Res., v 102, 20068-20086.

Wannamaker P.E., Booker, J.R., Jones, A.G., Chave, A.D., Filloux, J.H., Waff, H.S., Law, L.K., 1989. Resistivity cross section through the Juan de Fuca subduction system and its tectonic implications, J. Geophs. Res., 94, 14127-14144.

Worzewski, T., Jegen, M., Kopp, H., Brasse, H., Castillo, W.T., 2011. Magnetotelluric image of the fluid cycle in the Costa Rican subduction zone. Nature Geoscience, 4, 108-111.

4. Building a better MT model: An investigation into the influence of the assumption of smoothness in magnetotelluric inversion, and application to the Cascadia subduction system in central Washington

Abstract

In this chapter we begin by exploring the assumption of smoothness built into to standard magnetotelluric modeling, and the ramifications of making that assumption. Through a series of models, we show that this assumption can make it difficult to resolve sharp gradients in resistivity. We demonstrate that when such features occur in the true model, that tell-tale signs in the inversion model such the retreat of the resistive feature give us insight into the nature of the true model, and that by using a combination of imposed features and tear zones, where we collapse the smoothness assumption locally, we can find a more accurate inverted model. We also show that the assumption of smoothness inhibits our ability to resolve the complexity of a complicated conductive feature, and again, we show that the imposition of a tear zone can help with this. We apply the lessons of the chapter to the CAFE data in order to generate a model that more clearly shows the nature of the conductive features in the subduction zone, particularly that the fluid and melt phase rises directly from the slab at depths of 80-95 km, consistent with the depths for dehydration of chlorite serpentine and the eclogitization of metastable basalts. Assessment of this augmented model demonstrates that it is more robust than the model derived in Chapter 3.

1. Overview

Geophysical models are never entirely correct. Measurements of geophysical data are inevitably inexact, and station coverage woefully incomplete. Issues of sensitivity and resolution place boundaries on what is detectable, and simplifying assumptions are built into the inversion mathematics. While inversion methods allow us to create models that fit the data as closely as desired, there is a tradeoff between resolving real structure and generating false structure from noise that tips decidedly in favor of the latter as the misfit becomes small. For any reasonable selection of misfit, there are an infinite number of solutions that fit the model equally well (Parker, 1994).

The selection of a specific model is necessarily a subjective process involving the incorporation of a priori information and/or assumptions about the nature of the distribution of the measured parameter in the subsurface. This subjectivity demands that we approach each model critically, understanding the assumptions that inhabit each one, and how they affect the model. We need to be able to evaluate the accuracy of a given model, and consider ways in which the model might be improved. In MT, the non-linear relationship between the data and the model often makes it more difficult to carry out these evaluations, but a fairly standard set of methods has arisen

that MT practitioners utilize to evaluate the robustness of a given feature and test the resolution of the model, and measure the sensitivity of the model to perturbations.

Non-linearity also implies that even were the data error-free, it would not be possible for the model parameters to be equally well determined, requiring careful study of the sensitivity of the data (e.g., Schwalenberg et al., 2002). Pseudo-sections, which show a profile of apparent resistivity and phase interpolated over both period and distance, are a useful tool for exploring data sensitivity. Software packages such as WinGLink allow for model response derived synthetic pseudo-sections, which can then be differenced from pseudo-section generated from the data. The resulting residual pseudo-sections highlight regions for which the forward model does not closely reproduce the data. Some examples of this are included in Appendix 2a.

It has also been possible to use the elements of the sensitivity matrix directly as a measure of how small model distortions affect the data (Schwalenberg et al., 2002, Baba et al., 2006), but as this is a strictly linear approach it only has value in very close proximity to the derived model. Furthermore, full calculation of this sparse matrix at every step is very computer-intensive and for modern inversion methods such as non-linear conjugate gradients the sensitivity matrix is only considered within matrix-

vector products, and neither fully calculated nor retained at every step (Rodi and Mackie, 2001).

One of the most important tools used by MT investigators to explore a given model is manual editing of the model, which can be implemented in either a forward or inverse sense. As a forward modeling tool, manual editing serves to explore the range of models that are allowed by the data by varying different parameters such as resistivity or extent of a feature in a systematic way and observing the effect on the misfit between the data and model. For example, in a subduction zone setting with a robust volcanic front, we might suspect a conductive fluid release from the slab beneath the volcanic arc, even if it is not apparent from the initial inversion model. We can decrease the resistivity in the region above the slab until the misfit becomes worse, thereby establishing a limit for the lowest resistivity allowed by the data. This has been done in Oregon to show that a highly conductive feature is allowed (but not required) by the data (Evans et al., submitted), and in Costa Rica, reducing the resistivity was shown to even slightly improve the fit between the data and model (Worzewski et al., 2010).

This method can also be used to find the allowable extent of a given feature. In southern Tibet, the shallowest allowable bottom of a poorly constrained conductor was located by imposing a resistive halfspace at depth,

and raising the depth of the halfspace until the misfit worsened, enabling the investigators to constrain a maximum value for resistivity as well (Li et al., 2003). Beneath the East Pacific Rise, the depth to a conductive layer and the lateral extent of a conductive plume feature were constrained conjunctively by evaluating the misfit while varying these parameters (Baba et al., 2006). While widely used and undeniably useful, these forward modeling tools are limited by the non-linearity of MT in that they do not account for the inductive coupling between features.

As an inversion tool, conductive and resistive features can be removed from a model, and the inversion re-run, either without constraints or seeking a model near the starting model. If the feature recurs during the inversion or the fit is not reacquired, then the feature is taken to be required by the data. If the feature does not recur or comes back in an altered sense, and the fit is reacquired, we obtain information about the range of models that the data will accept. Extensive application of this method to key features of an MT model is standard practice; one rather detailed example can be found in a study of the structure of the lithosphere in NE Botswana (Miensopust et al., 2011).

This method can also be applied to incorporate a priori information into an inversion sequence. A feature can be built into the starting model and fixed,

as is standard practice when an ocean is present in a model, or built into the starting model and allowed to evolve with the inversion. In the latter case, the idea is to constrain the starting "neighborhood" to give the inversion a better opportunity to operate nearer the global minimum. For example, it is well known that MT can be rather insensitive to the resistivity of a highly resistive and extensive feature such as a subducting slab, so by including a resistive feature in the presumed location of the slab, it is possible to constrain the inversion sequence to search for solutions that include that feature. This can illuminate other model features that might otherwise have remained undetected or poorly constrained (Brasse et al., 2009, Matsuno et al., 2010, Evans et al., submitted).

The combination of manual editing and re-inversion provides a powerful and non-linear technique for exploring the range of acceptable models, but it does nothing to challenge the assumptions inherent in the inversion itself. In this chapter we will examine potential consequences of the assumption of smoothness that is built into the inversion process, and explore some techniques that can be utilized to recognize and mitigate some of those consequences. Finally, we will apply those lessons to the data from Chapter 3, with the objective of producing a demonstrably more accurate MT inversion model.

All of the models in this chapter were generated using the WinGLink MT software package (Rodi and Mackie, 2001). To standardize the models and maximize the applicability to the CAFE MT data set, the same parameters were used for all of the inversions unless otherwise noted. The profiles are all 300 km long with 60 stations arranged at roughly 5 km distance, and the inversion grids are all 76 rows by 196 columns, with row width increasing with depth. All inversions solve for the smoothest model using the uniform grid Laplacian operator. Error floors are set to five percent for the TM mode and ten percent for the TE mode, and the tipper data is included. The parameters α and β, which define the relationship of the smoothness parameter in the vertical as compared to the horizontal, and the way in which the smoothness changes with depth respectively, are set to 1.5 and 1.7 respectively, and the regularization parameter τ is equal to 3.3.

2. Theoretical underpinnings

The general 2-D MT inverse problem can be thought of in terms of attempting to solve for **m** in the equation

$$\mathbf{d} = F(\mathbf{m}) + \mathbf{e} \qquad \textbf{(1)}$$

where the components of the N-dimensional column vector **d** represent the observed magnetic and electric fields (in the form of amplitude and phase of apparent resistivity for a given station, period, and polarization) and the components of the M-dimensional column vector **m** represent the resistivity of the individual elements in model space. F is the transformation from model space to data space required by Maxwell's equations, and the components of the N-dimensional column vector **e** represent the data errors.

Unfortunately, solving equation (1) for **m** turns out to be impossible for a number of reasons, the first of which is that the chances of a solution actually existing is almost certain to be zero, especially if the column vector $\mathbf{e} \neq 0$. The standard approach would be to move away from the idea of an exact solution, and instead to redefine solution to mean an **m** for which F(**m**) matches **d** as closely as possible in some pre-defined way. This is done by posing the problem as an optimization problem, where an objective function is minimized subject to various constraints.

$$\Psi(\mathbf{m}) = (\mathbf{d} - F(\mathbf{m}))^T \; V \; (\mathbf{d} - F(\mathbf{m})) \qquad \textbf{(2)}$$

In a least squares approach, such as that shown in equation (2), the objective function Ψ is defined as the squared L_2 norm of the residual vector, subject to a positive-definite weighting matrix **V,** which is typically related to the variance of the error vector.

This brings us to our second difficulty, namely that in order to ensure the existence of a least squares solution to a real geological problem, we must either make the size of **m** very large by using a dense sampling grid, or define the solution set so broadly as to not be useful. In either case we ensure that any solution that exists is not unique, and so the least squares problem becomes ill-posed and unstable. For inverse problems involving large model spaces, the standard approach is to introduce a stabilizing term that favors some models over others by penalizing some pre-defined property that is deemed to be undesirable. While several stabilizing functions have been successfully used in various geophysical applications, many magnetotelluric algorithms employ the minimum norm of the Laplacian, which will seek the smoothest model possible that fits the data. The argument is that by seeking the smoothest model (for a given misfit), only structure explicitly required by the data will be resolved (de Groot-Hedlin and Constable, 1990). In practice, this stabilizing function rules out many geologically incomprehensible mathematical solutions and forces the algorithm to seek solutions that search

for structures with coherent regional features. The regularized solution that is used to generate all of the models in this study is given in equation (3) below

$$\Psi(\mathbf{m}) = (\mathbf{d} - F(\mathbf{m}))^T \; V \; (\mathbf{d} - F(\mathbf{m})) + \lambda \mathbf{m}^T \mathbf{L}^T \mathbf{L} \mathbf{m} \qquad \textbf{(3)}$$

where the matrix **L** is a simple, second-difference operator such that **Lm** approximates the log of resistivity for a uniform grid of model blocks (Rodi and Mackie, 2001). The regularization parameter λ is a positive number that determines globally the weight given to the stabilizing functional. The selection of λ is chosen so as to balance model roughness with data misfit. It is generally chosen either with a specific target misfit or at such a place on the misfit vs. roughness curve that increasing λ results in a small increase in model roughness relative to the decrease in misfit, and decreasing it results in a small decrease in misfit relative to the increase in roughness.

Finally, the non-linearity of the problem requires that the solution (the minimization of the objective function Ψ) be approached iteratively. The non-linear conjugate gradient (NLCG) method used in this study is a modification of the steepest descent method, where the search direction in an N-dimensional topography is defined as the direction along which the value

of the objective function decreases most rapidly and proceeds until it is minimized along that line. At that point, it searches for the direction of maximum decrease again. For NLCG, the search direction is a linear combination of the line of steepest descent and the previous search direction. Going "downhill" along these planes not only helps to avoid small local minima (Zhdanov, 1993), but greatly reduces the calculation effort by retaining directional information from previous iterations within each new search direction.

3. A closer look at the stabilizing functional

The effect of the stabilizing functional shown in equation (3) is to penalize models in which the conductivity changes sharply. Not only does this stabilize the inversion and allow us to find a "best" model for a given misfit, but it prevents an entire class of geologically unsound models in which anomalous conductivities that are purely artifacts of the inversion process populate model space. While this is clearly desirable, it is also true that sharp boundaries do exist in nature, and smooth algorithms may not sufficiently resolve these boundaries.

In order to address these difficulties, several algorithms have been developed that allow for sharp boundaries by making different global assumptions about the distribution of the modeled parameter in the subsurface, for example by favoring models made up of layers (Smith et al., 1999, de Groot-Hedlin and Constable, 2004) or containing primarily blocky structure (Mehanee and Zhdanov, 2002). Of course, each of these global algorithms present trade-offs, and are effective largely to the extent that the underlying assumptions are accurate throughout the modeled space. While a priori knowledge regarding the location and nature of sharp discontinuities can be an extremely useful implement in resolving the associated structure, its utility in resolving features in a sufficiently complicated subsurface is dependent on the extent to which it can be effectively applied locally.

Inversion packages such as WinGLink (Rodi and Mackie, 2001) and Occam (de Groot-Hedlin and Constable 1990) allow for the elimination of the penalty for roughness along presumed discontinuities, and while this tool has recently been used to good effect (Matsuno et al., 2010, Miensopust et al., 2011, Evans et al., submitted), we are cautioned that incorrect placement of such boundaries may produce misleading results (de Groot-Hedlin and Constable, 1990). While this is certainly true, we must also recognize that the use of such tools is simply a matter of trading one set of assumptions for

another and we should be cautious in any event. We should also be asking to what extent the assumption of smoothness can return misleading results.

Figure 1 shows the results of an experiment designed to provide one answer to that question. The forward model (fig 1a) is a 100 Ωm halfspace in which a 10,000 Ωm resistive block and a 1 Ωm conductive block are placed in contact with one another from depths of 60-115 km. Each block is 60 km wide. The forward response to this conductivity profile was generated and saved as synthetic data to an array of 60 stations located at roughly 5 km intervals at the surface.

We then generated inversions from the synthetic data using the WinGLink software package. Instead of using a halfspace starting model however, we used a perfect copy of the forward model, such that initially, the (F(**m**)-**d)** term was equal to zero. Without the stabilizing functional, the objective function would also have been equal to zero, and the inversion would have stopped immediately with the correct solution. With the stabilizing functional, despite the fact that the misfit for the first iteration was zero, the objective function was not minimized and the inversion proceeded. The implication is that the differences between the forward/starting model (Fig 1a) and the inversion model (Fig. 1b) can be entirely attributed to the effect of the smoothing stabilizing functional on the inversion.

The conductor has for the most part been retained in the correct location, with an accurate resistivity of 1Ωm near the center. The corner detail of the original feature have been lost, as has its uniformity, as the intensity of the conductive feature in the inversion grades out in roughly concentric circles.

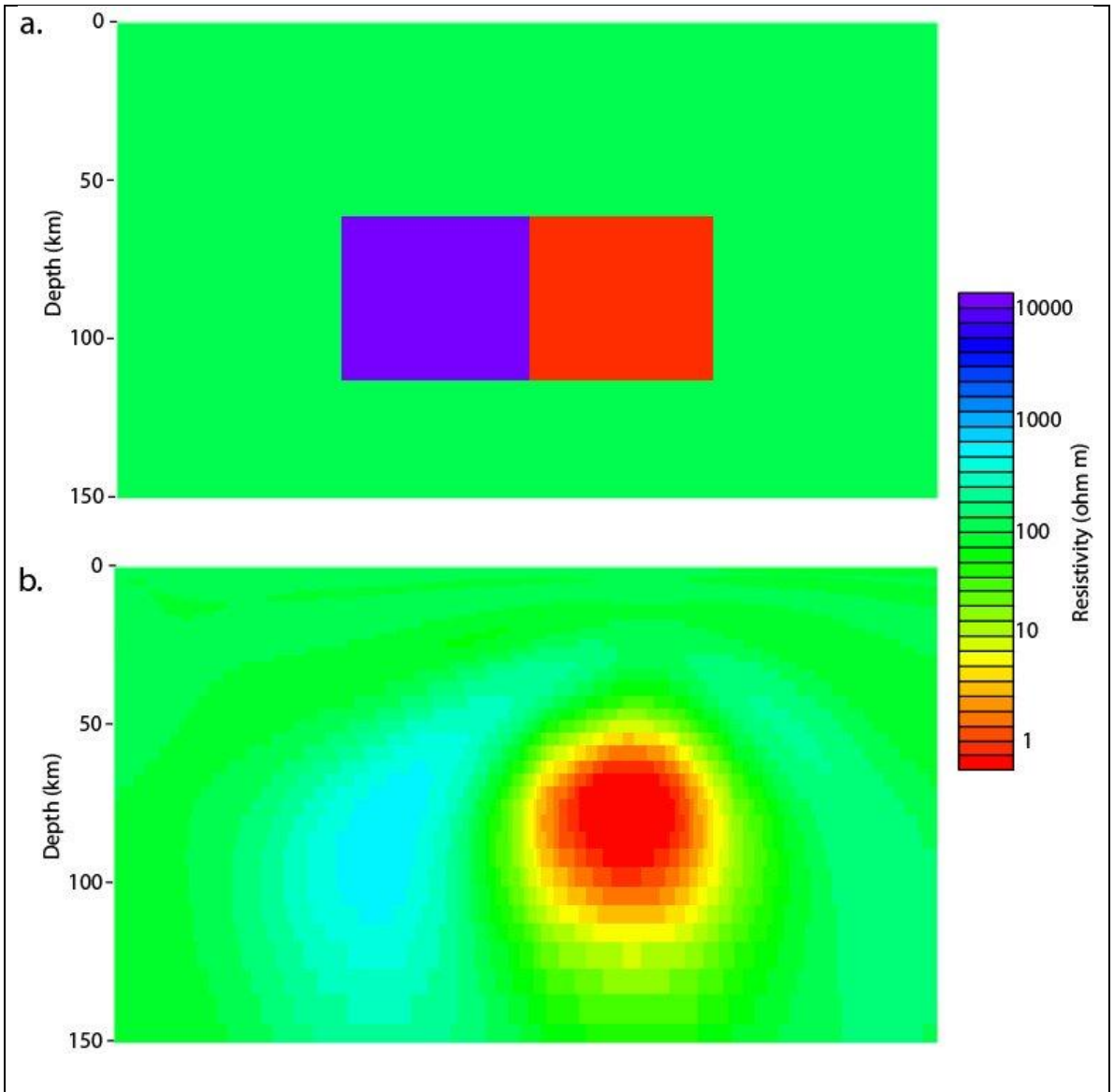

Figure 1: Inversion model demonstrating the effect of a smoothing stabilizing functional for a simple two block model. Figure 1a shows the forward model, which was also used as the starting model, and Figure 1b shows the inversion.

The resistive block has fared less well, with the highest resistivity more than a full order of magnitude too low at 600 Ωm and displaced nearly 15 km from the original center, fully 55 km from the most conductive value of 1 Ωm despite sharing a common boundary in the forward and starting models. The resistor appears stretched out in the vertical, wrapping around the conductive structure at a nearly constant distance, and a phantom resistor of 150-200 Ωm has appeared on the opposite side of the conductor.

None of this is intended to suggest that the incorporation of the smoothing stabilizing functional is misguided in any way. In the absence of a priori information, it has been the most effective way to stabilize the objective function and ensure that features in the inversion are required by the data. The starting model in our example was specifically selected to highlight the limitations of a smooth model assumption, and a general interpretation of the final image would still provide good insights into the conductivity structure of the subsurface. Instead, we strive to develop a better understanding of the tradeoffs inherent in this assumption, and to explore methods that we can employ to improve the final model, particularly as they apply to a subduction setting.

4. Exploration

In this section, we explore the effects of incorporating a priori information into the inversion of synthetic data generated from known models. We looked at more than 200 full inversions from dozens of models ranging in complexity from simple layers and blocks to simulated subduction zone models. Two techniques proved to be particularly useful both to improve the accuracy of the inversion models, and to provide additional information about the subsurface to assist interpretation.

The first of these is to impose high resistivity in the initial models at locations where it would be expected, such as the location of a subducting slab, but leaving the feature free to evolve with the model. Conceptually, the idea is to start the inversion in a topographical neighborhood that is closer to the global minimum for the objective function than the neighborhood representing a simple halfspace. In practice, the presence of the resistor tends to help illuminate nearby conductors. Additionally, as smoothness is imposed on the inversion, the boundary of an imposed resistor will appear to retreat from a nearby conductor in order to minimize model roughness; the extent of this retreat is positively correlated to the intensity and proximity of the conductor. Conversely, the imposition of a conductive feature in starting models did not seem to improve the inversion.

The second technique was the imposition of a zone in which the smoothness constraint was collapsed locally, hereafter referred to as a tear zone. These tear zones were primarily imposed in places where we suspected a rapid change in conductivity, such as at the top of a subducting slab where dehydration reactions are occurring and fluids are being released. Tear zones also proved useful in illuminating the structure of a conductor, as the imposed smoothness tends to obfuscate detail and ensure that the most conductive region appears near the center.

We did not succeed in developing any method that works in every situation; presumably the non-linear nature of MT precludes this possibility. What we have instead are a set of tools that can be used first to develop an intuition about a given problem, and then to work towards an improved inversion model. Finally, we can evaluate the models and demonstrate which of them likely most accurately reflects the conductivity structure of the subsurface.

The first set of inversion models is shown in figure 2. The forward model (fig. 2a) includes a 9000 Ωm dipping resistive layer intended to represent a slab, with two relatively thin 3 Ωm conductors at the top of the slab that correspond with where we might expect fluids released during dehydration reactions to occur. A 0.33 Ωm conductive feature representing the ocean is also present in the upper

left corner of the model. This conductor is locked in for all of the inverted models just as would be for an inversion of real data in a coastal MT study.

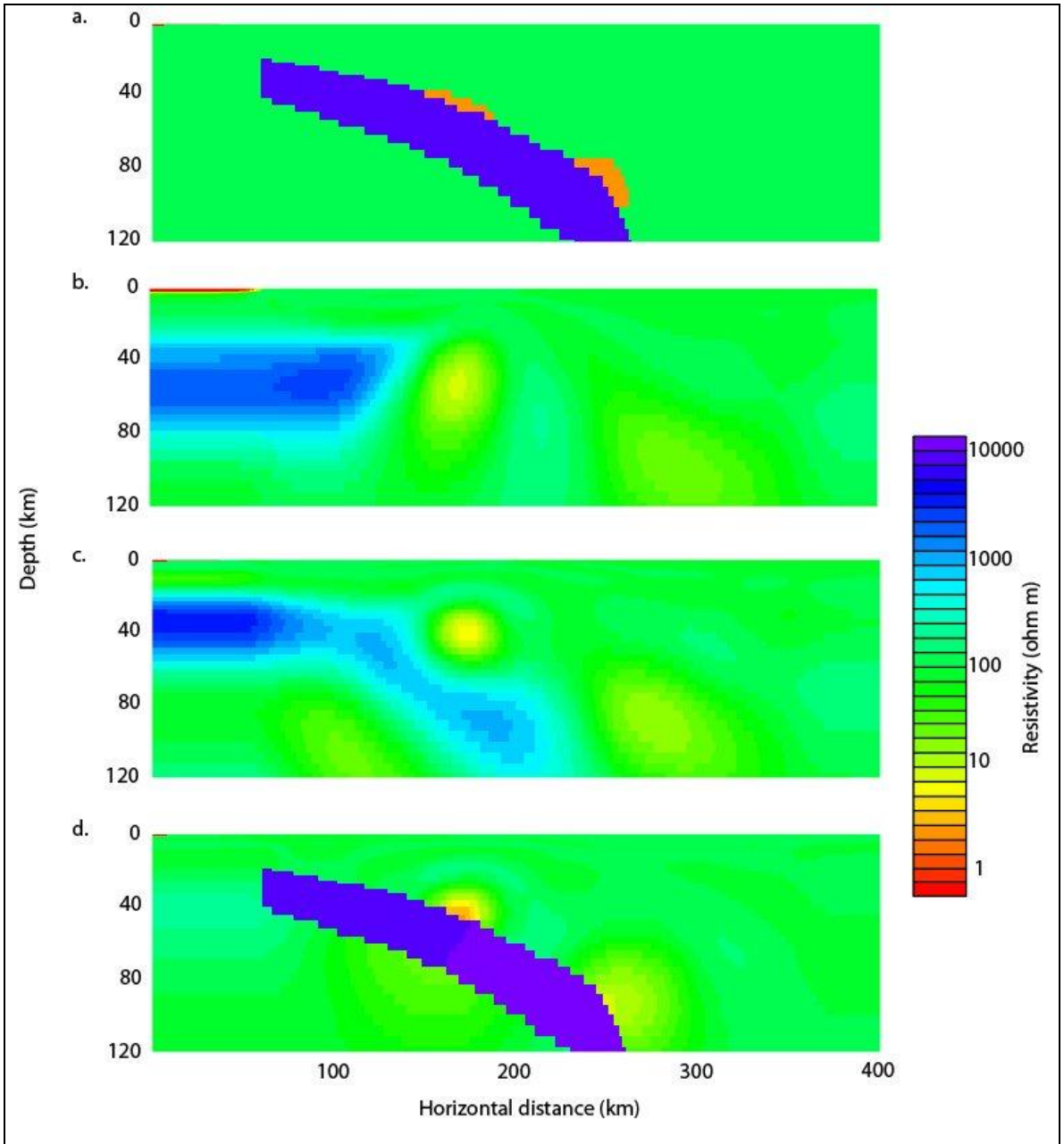

Figure 2: Inversion model for a subducting slab with thin conductors at depths corresponding to fluid release from dehydration reactions for Cascadia. Fig. 2a shows the forward model. Fig. 2b shows the inversion model from a halfspace. Fig. 2c shows the inversion model with the resistive slab imposed into the starting model. Fig. 2d shows the inversion model with the imposed resistive slab and a tear zone incorporated into the slab.

The halfspace inversion model (fig. 2b) suffers from some of the same limitations that we observed in the two block model. Both conductors are resolved in essentially their correct locations, but much of the detail of their shapes has not been captured. The dipping resistive layer is essentially non-existent downstream of the shallow conductor. This smoothing away of the resistive feature also results in overestimating the resistivity of the two conductors; the lowest resistivity in the shallow conductor is 10 Ωm and in the deeper conductor 24 Ωm.

Figure 2c shows the model for the inversion in which the starting model included the dipping resistor. While the inversion misfit tends not to be terribly sensitive to changes to the resistive feature, the inclusion of the resistor in the starting model helps to illuminate the details of the overlying conductors. The location of both conductors can now clearly be seen to be at the top of the dipping resistor. Additionally, both are better resolved in space and suffer from less smearing. Their resistivities are also approaching their correct values, with the resistivity of the shallow conductor at 7 Ωm and that of the deep conductor 17 Ωm. The dipping resistive feature is also still present in the model, but with a highest resistivity of only 1000 Ωm. Additionally, it has retreated away from the conductors just as we saw for the two block model; we have come to recognize

this as a reliable indicator that the distance between the conductors and resistor in the starting model (or by extension the real subsurface) is not very large.

Our final inversion model for this series is shown in figure 2d. For this inversion, we imposed the dipping resistor in place, and also placed a tear zone covering the resistor, encouraging the inversion to seek solutions where the conductivity can change abruptly at its edges. This model has a very high level of accuracy. The shallow conductor is located in the correct place at the top of the slab, with a resistivity of as little as 3 Ωm. The deeper conductor is also correctly located, with resistivities down to 10 Ωm.

The imposition of the tear zone at the upper boundary of the dipping resistor changes the assumption implicit in the inversion from seeking models with smooth transitions to those with sharp boundaries. From forward models for which the conductors share a boundary with the dipping resistor, this leads towards improved accuracy in the inversion, but we should also explore models in which the boundary is not shared to understand what potential the imposition of a tear zone has to lead us astray.

The series of inversions in figure 3 is designed to help answer this question. The forward model (fig. 3a) consists of a 9000 Ωm dipping resistive feature and 0.33 Ωm ocean identical to those in the previous example. There is also a pair of

3 Ωm conductors, but in this case, they have been separated from the dipping resistor.

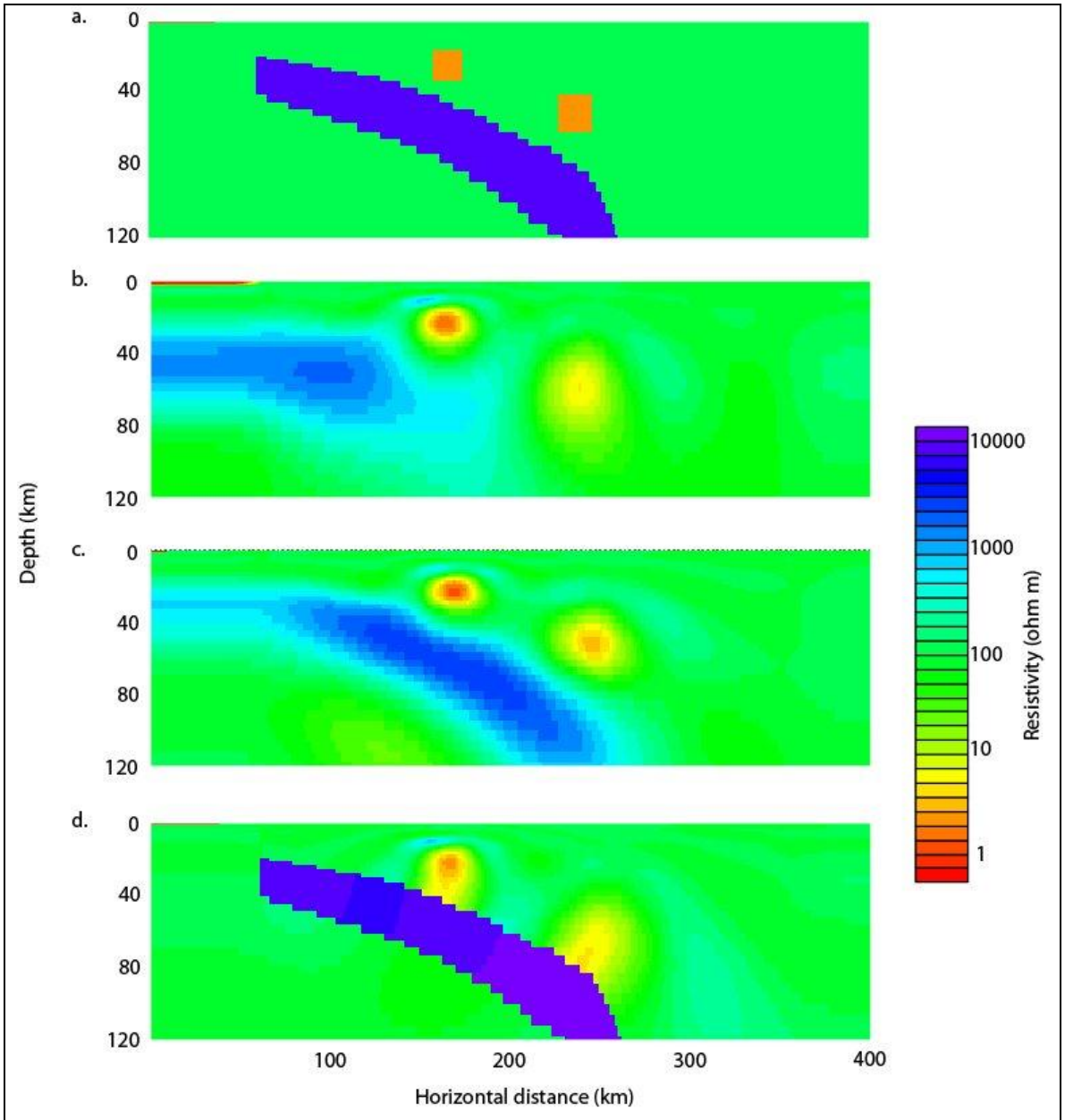

Figure 3: Inversion model for a subducting slab with conductors separated from the top of the slab. Fig. 3a shows the forward model. Fig. 3b shows the inversion model from a halfspace. Fig. 3c shows the inversion model with the resistive slab imposed into the starting model. Fig. 3d shows the inversion model with the imposed resistive slab and a tear zone incorporated into the slab.

The halfspace model (fig. 3b) does reasonably well recovering all of the features in the inversion. Both conductors are present and in the correct location, and while the deeper conductor has faded to 7 Ωm, the shallow one has maintained its original resistivity of 3 Ωm. Even the dipping resistor is resolved here to some degree, with resistivities of several hundred Ωm extending beyond depths of 80 km.

Figure 3c shows an inversion model in which the dipping resistor was imposed into the starting model. Both conductors are very well resolved, with the deeper of the two reaching a resistivity of 4 Ωm. The dipping resistive feature remains largely intact as well, with resistivities of more than 1000 Ωm extending to depths of more than 120 km. The resistor also shows very little sign of retreat due to smoothing out in the vicinity of a strong conductor. This is a good indication that the conductors do not share a boundary with the dipping resistive feature, and counter indicative to installing a tear zone at the top of the conductor.

Nevertheless, figure 3d shows an inversion model for which a tear zone was imposed over the dipping resistor. The shallow conductor maintains a low resistivity value of 3 Ωm in the correct location, but also appears to be connected to the slab feature, which we know not to be the case. The situation for the

deeper conductor is even more problematic, with resistivities as low as 6 Ωm that appear to be in direct contact with the dipping resistor.

The two examples shown are fairly clear cut, but it is obviously possible for intermediate cases to exist for which determining whether or not to use a tear zone would be more challenging. While the careful imposition of resistors in the starting model can simplify the task by constraining the location of the conductive features, there are other tools that we can use to evaluate the final inverted models. We will explore this more fully in section 5.

For the next set of inversion models (Fig. 4), we move on to another application of the tear zone. Figure 4a shows a forward model consisting of a 9000 Ωm resistive layer, and a conductive feature made up of two 1 Ωm blocks that overlap at one corner.

The halfspace inversion model is shown in fig. 4b. The detail in the original conductor has been lost to the smoothness constraints, replaced by a single conductor with a core of resistivity 1 Ωm in the upper right quadrant, surrounded by concentric elliptical shapes of increasing resistivity, with the whole occupying roughly the same area as the original conductor.

The inversion model in fig. 4c uses a starting model with a tear zone imposed over the area occupied by the conductor in the halfspace model, resulting in a partial recovery of the detail of the original feature. The conductor in this model

clearly exhibits the dual centers of the forward model, one in the upper right and the other in the lower left, both with resistivities in the 1-2 Ωm range.

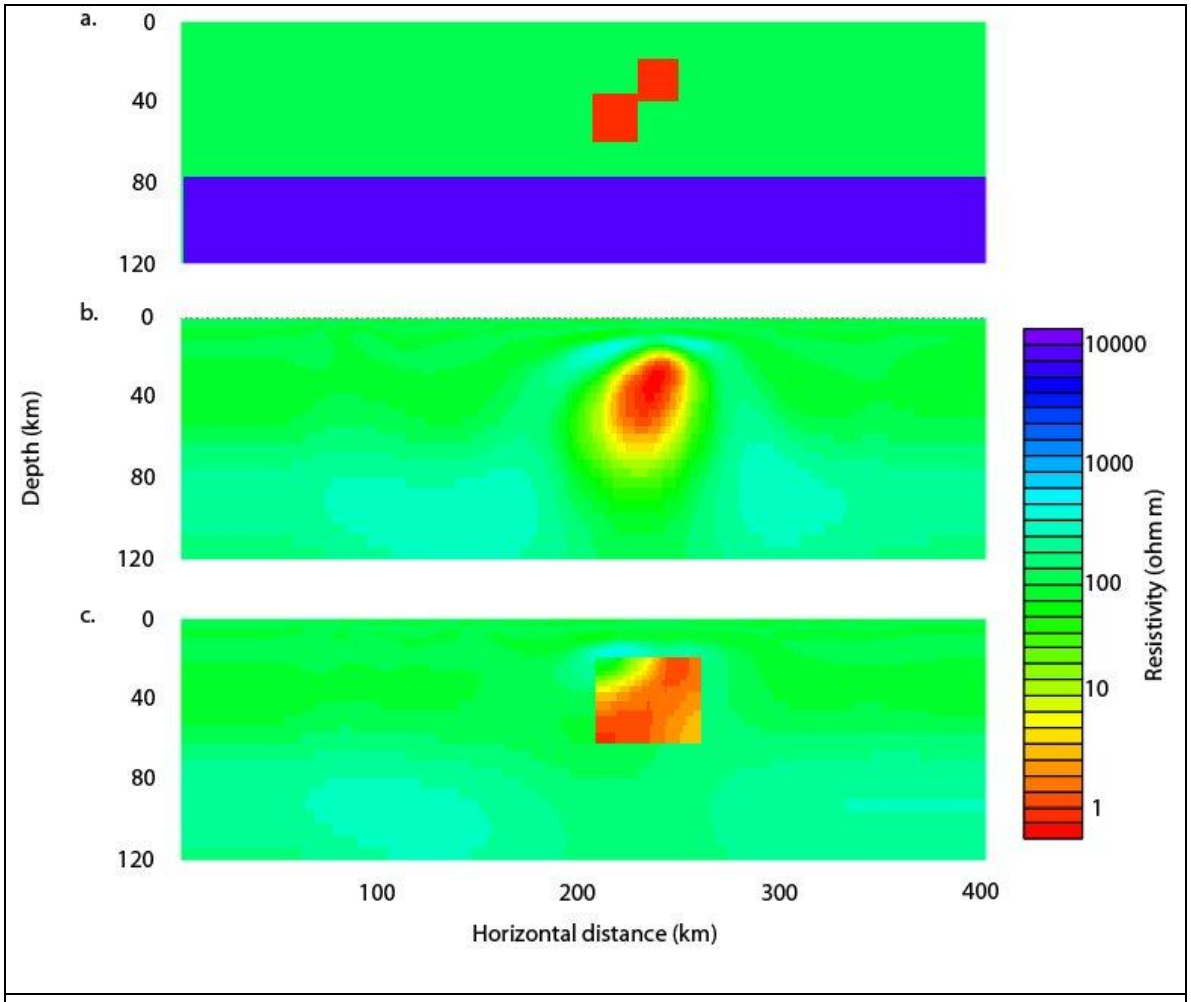

Figure 4: Inversion models demonstrating the loss of detail for a conductive feature due to the smoothness constraint, and the use of tear zones to recover some of the detail. Fig. 4a shows the forward model. Fig. 4b shows a halfspace inversion model. Fig. 4c shows an inversion model in which a tear zone has been imposed over the boundaries of the conductor.

While the smoothness constraints tend to affect most conductive features, it is not always possible to recover detail using tear zones. One set of inversions for which this strategy is ineffective is shown in figure 5. The forward model in fig.

5a shows a conductive column with conductivities that increase with depth. The bottom layer has a resistivity of 1 Ωm, with layers of 3 Ωm, 8 Ωm, and 14 Ωm

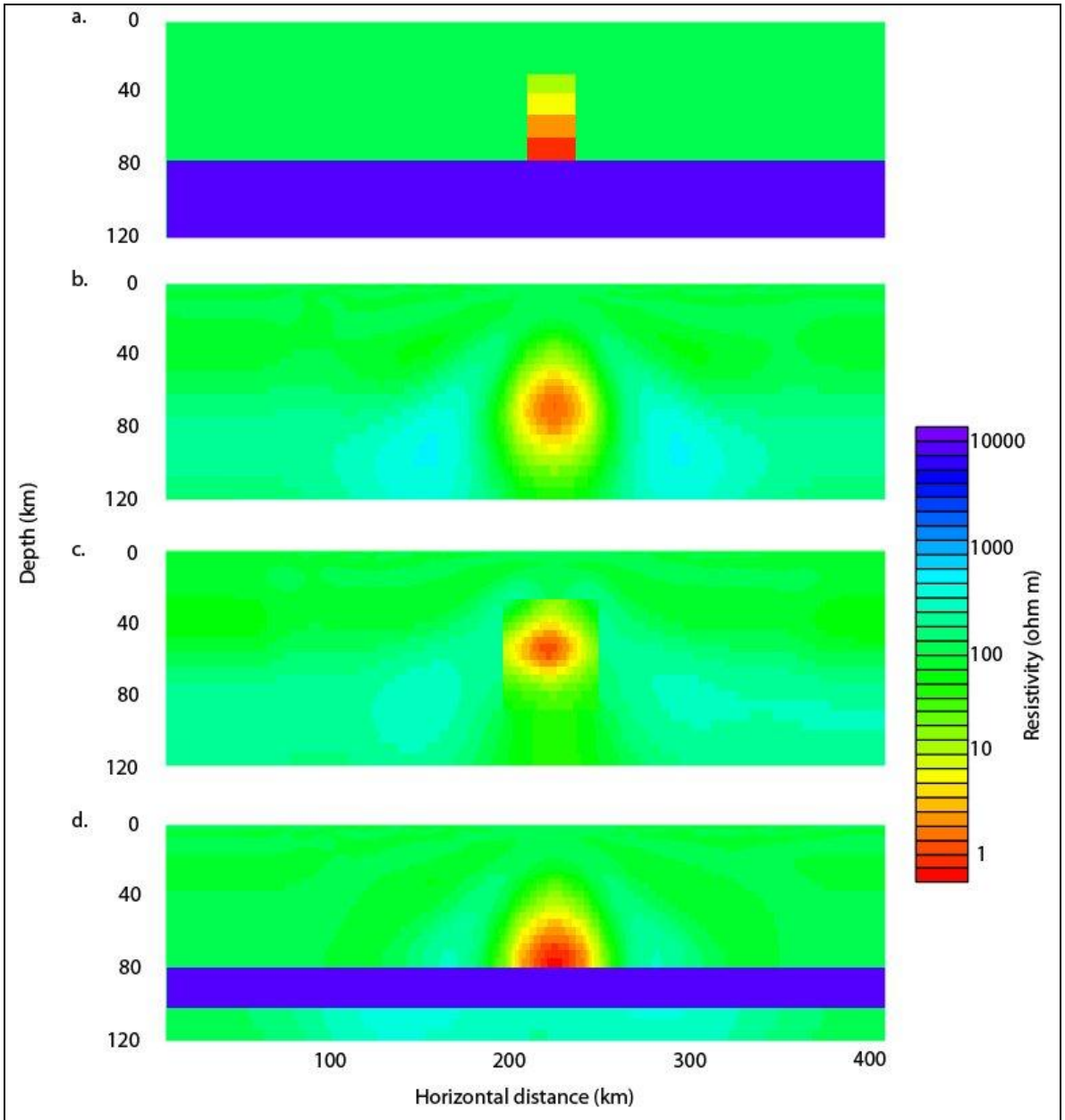

Figure 5: Inversion models demonstrating the loss of detail in a conductor with a gradient. Fig. 5a shows the forward model. Fig. 5b shows the halfspace inversion. Fig. 5c shows an inversion with a tear zone imposed over the region of the conductor, and Fig. 5d an inversion model with both an imposed resistive layer and tear zone over the resistive layer.

respectively. The base of the bottom layer is in contact with a thick resistive layer with a resistivity of 9000 Ωm.

We can see in the halfspace inversion (fig. 5b) that the conductive gradient in the forward model has been replaced by the characteristic conductive feature that we have now seen many times, a concentric series of conductivities that decrease outward from the center, this time with resistivities as low as 4 Ωm. The underlying resistive feature is weakly in evidence, with some suggestion of the retreating character that we have come to identify with a conductor in close proximity. This can be easily confirmed by running an inversion with the imposition of a resistive layer (which was conducted but the results are not shown here as they demonstrate nothing new).

Our attempt to recapture the detail of the original conductor by imposing a tear zone on the area of the conductor is shown in fig. 5c. In this case, we are unable to improve the image, as the influence of the nearby resistor is too strong. If the conductor were isolated in the halfspace, we would be able to improve the resolution to some degree, but with the resistive layer directly below, imposing the tear on the conductor simply allows it to contract in the upper region of the tear zone.

Since the imposed resistive layer retreats during the inversion, we expect that the conductive feature is very close, leading us to try imposing a tear zone over

the resistor. The results of this inversion are shown in fig. 5d. While this is the most accurate of our inversion models for this set, the details of the conductor are essentially the same as they would have been for a conductor of uniform resistivity in the forward model, so we cannot claim that any detail has been salvaged.

The preliminary models for the CAFE data set in Chapter 3 show a moderate conductor near the slab at a depth of ~40 km, and a strong conductor which appears to rise from near the slab at a depth of ~80 km. This is in contrast with the results of another study in Oregon along the EMSLAB line (Evans et al., submitted) which shows a strong conductor rising from the slab at the shallower depth, and extending horizontally at ~25 km depth across the profile at least as far as the volcanic arc. The deeper conductor near 80 km depth does not show up in the standard inversions of that model, but if such a conductor is imposed into the starting model, it is retained in the inversion and an acceptable fit to the data is achieved. Inversions of the tipper data (comparing only the vertical and horizontal magnetic fields) alone also suggest that such a conductor does exist. The question becomes whether the deeper conductor is much weaker in the Oregon line, or whether the presence of the extended shallower conductor renders it less detectable.

The inversion set in figure 6, while in keeping with our general theme, is part of a series of models that were generated specifically to address this difference

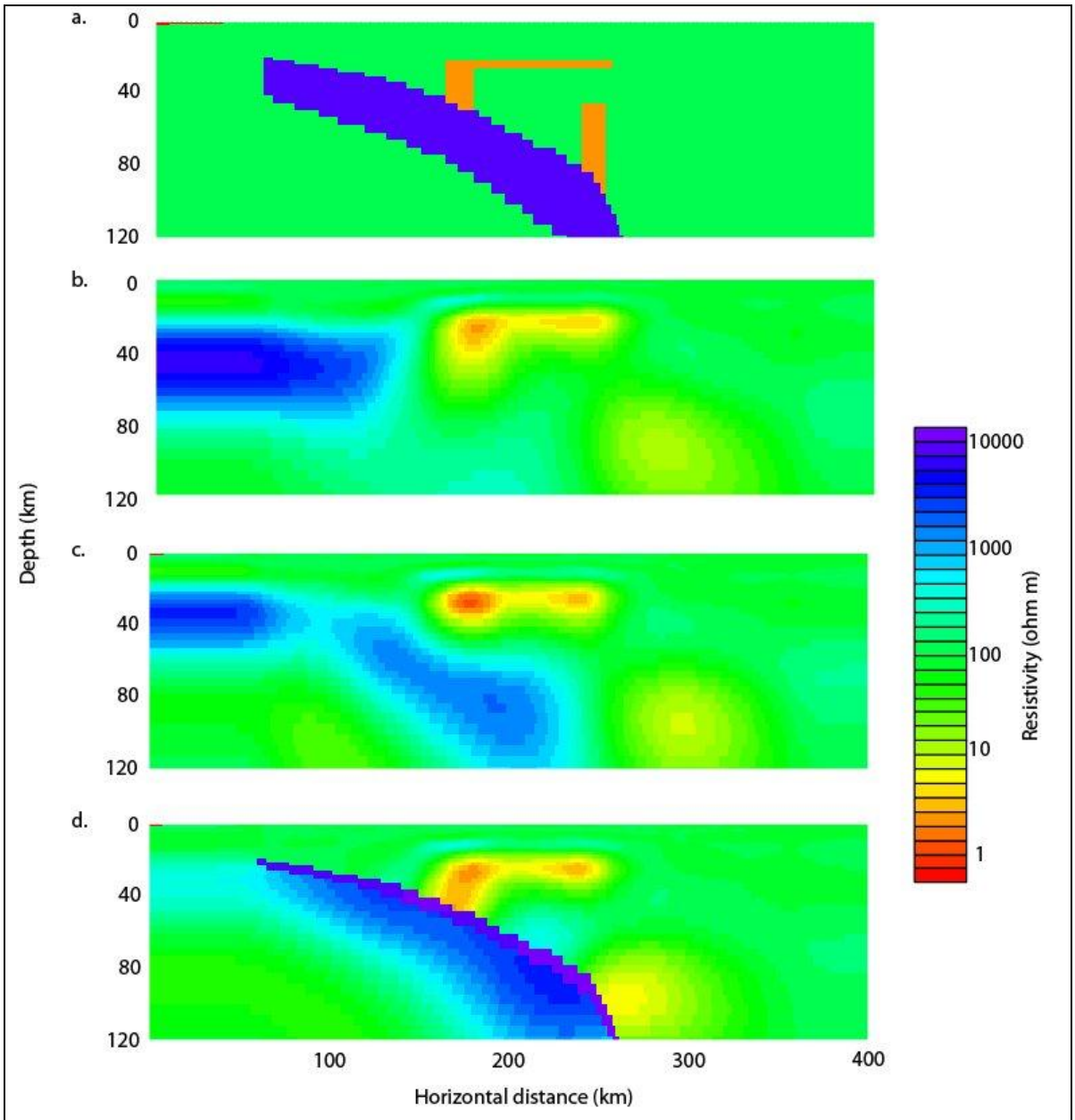

Figure 6: Inversion models demonstrating the effects of a strong shallow conductor that extends horizontally in the direction of the volcanic arc. Fig. 6a shows the forward model. Fig. 6b shows the inversion model from a halfspace. Fig. 6c shows the inversion model with a dipping resistor imposed on the starting model, and Fig. 6d includes both the dipping resistor and an imposed tear zone.

between the CAFE and EMSLAB lines. Figure 6a shows the forward model, with conductor is actually quite well resolved, and the telltale retreat of the resistive layer is in evidence as well. The deep conductor has resolved to the now familiar concentric shape, with a lowest resistivity of 14 Ωm.

Imposing the dipping resistor on the starting model does not improve the results very much, although it does provide some useful information. The shallow conductor loses some of its shape as the imposed smoothness causes the inversion to try to put distance between it and the resistor. The deeper conductor has a lowest resistivity now of 11 Ωm, but its impact on the imposed resistor should cause us to consider a more conductive value. Additionally, the retreat of the resistor from both conductors suggests that we might do well to impose a tear zone at the top of the dipping resistive feature.

The starting model for the inversion image in figure 6d included both a dipping resistor and a tear along the top layer of the resistor. The model is quite accurate with respect to the forward model. The shallow conductor is very well resolved, and the deeper conductor has resistivities as low as 6 Ωm, although the details of the shape of the conductor have not been captured. It is clear from this inversion series that if there is a deeper conductor for the EMSLAB transect, that it is not nearly as pronounced as the deep conductor in the CAFE line.

5. Application to the CAFE data set

The imposition of resistive features and tear zones into a starting model have been shown to be effective techniques to improve the quality and resolution of an inversion, but optimally require a priori data concerning the location of the top of the resistive feature. For the CAFE study, we analyzed data collected at dense arrays of roughly collocated passive seismic and magnetotelluric stations. Both sets of data were analyzed independently, employing Generalized Radon Transform (GRT) migration for the seismic data (see Chapter 2), and Non Linear Conjugate Gradient (NLCG) inversion for the MT (see Chapter 3).

There are a number of advantages in investigating collocated seismic and MT data. First of all, because the two techniques are sensitive to entirely different sets of rock properties (Hellfrich, 2003), each is likely to be able to provide information pertaining to the structure of the subsurface that the other cannot. Secondly, because velocity and conductivity are often in fact correlated (Stanley et al., 1990, Jones et al., 2009) either directly or simply in the fact that at distinct geological boundaries both parameters are likely to change (Gallardo, 2007, Moorkamp et al., 2007, Jones et al., 2009), the two studies will provide some independent confirmation of one another. Finally, the two

techniques can be used in conjunction to emphasize the strengths and mitigate the weaknesses of the other.

The teleseismic migration method, involving backpropagation of a scattered wavefield to identify the scattering points in the subsurface, is particularly suited to the illumination of sharp geological boundaries (Rondenay et al., 2009). Conversely, MT is highly sensitive to the presence of conductive fluid and melt phases, and we have shown that these can be even better constrained if we have a priori understanding of some of the resistive features in the profile. Figure 7 shows the primary inversion models from the teleseismic migration study from Chapter 2 as well as the MT study from Chapter 3. While both of these models have been discussed in detail in their respective chapters, we look at them now in a new light. Specifically, we want to consider the migrated model as a priori information that can be incorporated into a new MT inversion in order to better constrain the conductive features in the latter.

From the migrated image (fig. 7a), we are able to clearly identify the top of the descending slab, from a depth of ~20 km at the coastline (left margin) to depths of ~80 km or more. We can identify regions where serpentinization has occurred due to fluid release from the eclogitization of the hydrated basalts of the upper crust (A) (Rondenay et al., 2001, Bostock et al., 2002), the cool nose of the mantle wedge (B) (van Keken et al., 2010), and a fluid or melt phase near the top of the

slab at depth (C) consistent with the release of fluids from chlorite harzburgite in the upper mantle and subsequent conversion of metastable gabbros in the lower crust to eclogite (Hacker et al., 2003, John and Schenk, 2003). We can also clearly make out the continental Moho in the east.

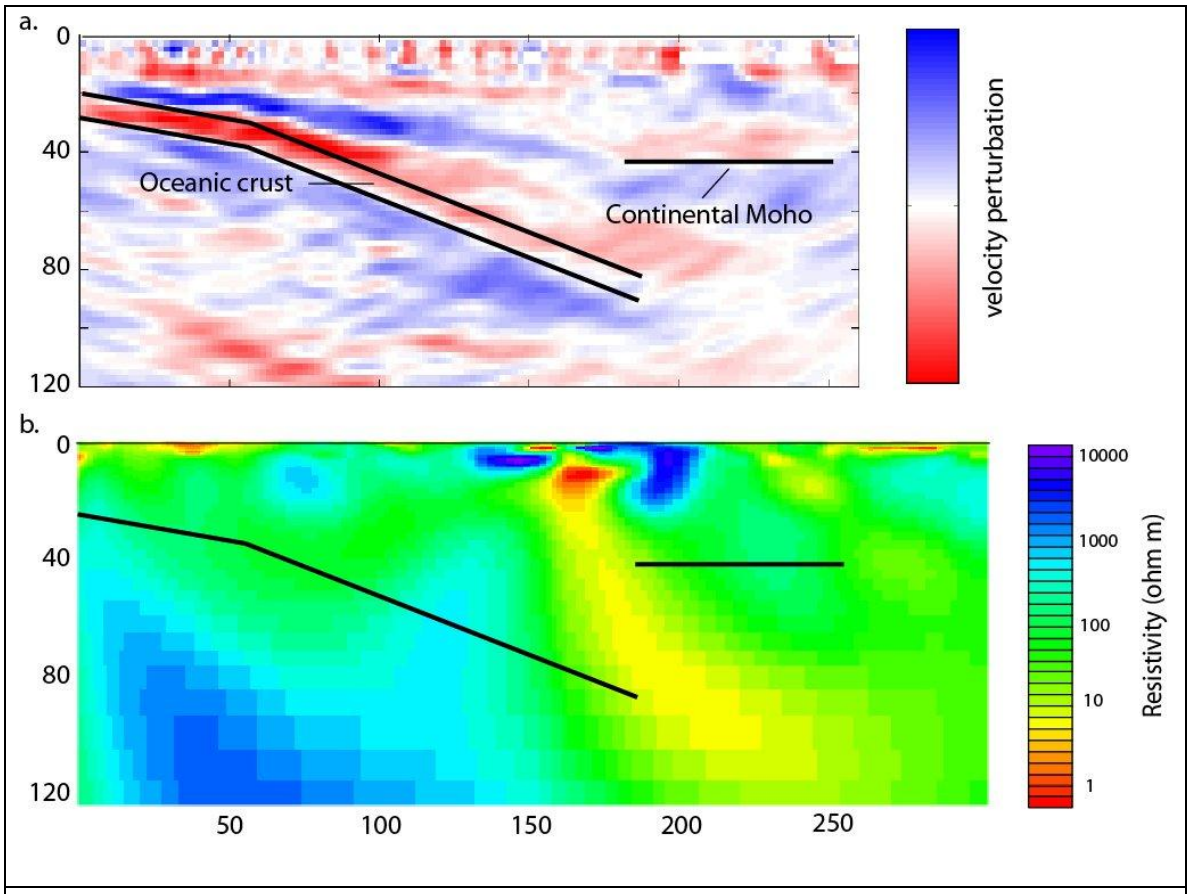

Figure 7: Primary images from the teleseismic migration (fig. 7a) and magnetotelluric (fig. 7b) studies from the previous chapters.

In the MT image (fig. 7b), we are not able to make out the contrast at the top of the slab, but based on our discussion in section 4, we recognize that the smoothness constraint would cause a resistive slab to retreat from the conductors

at A and C. These conductors serve to confirm our interpretation of the migrated image, as does the resistive feature at B. Additionally, the MT image shows quite clearly the connection between the conductive fluid melt at C and an intense conductor (D) that is consistent with a magma chamber feeding the nearby Mt. Rainier (Stockstill et al., 2002, Hildreth, 2007, Pommier and LeTrong, 2007). The conductive pathway between these two features also provides an explanation for the disruption of the continental Moho evident in the migration image.

While the two models are clearly consistent with one another, the objective is to improve the resolution of the conductors in the MT model using the techniques from section 4. Using the migration model to define the upper boundary of the descending slab, we impose a resistor into the starting model and a tear zone over the top few km of the imposed resistor. Additional inversions were run with a tear zone at the continental Moho as defined by the migration model, and over the conductor below Mt. Rainier, but these did not improve the images and were not incorporated into the final augmented model (fig. 8).

It is clear that the constraints on the conductors are somewhat different in the augmented model as compared to the original halfspace inversion, but we must recognize that we have traded one assumption for another and still bear the burden of demonstrating that the new model is more accurate. The traditional

way to accomplish this is to look at the rms misfit values associated with each model. The rms misfit value for the original halfspace model was 3.08, and for

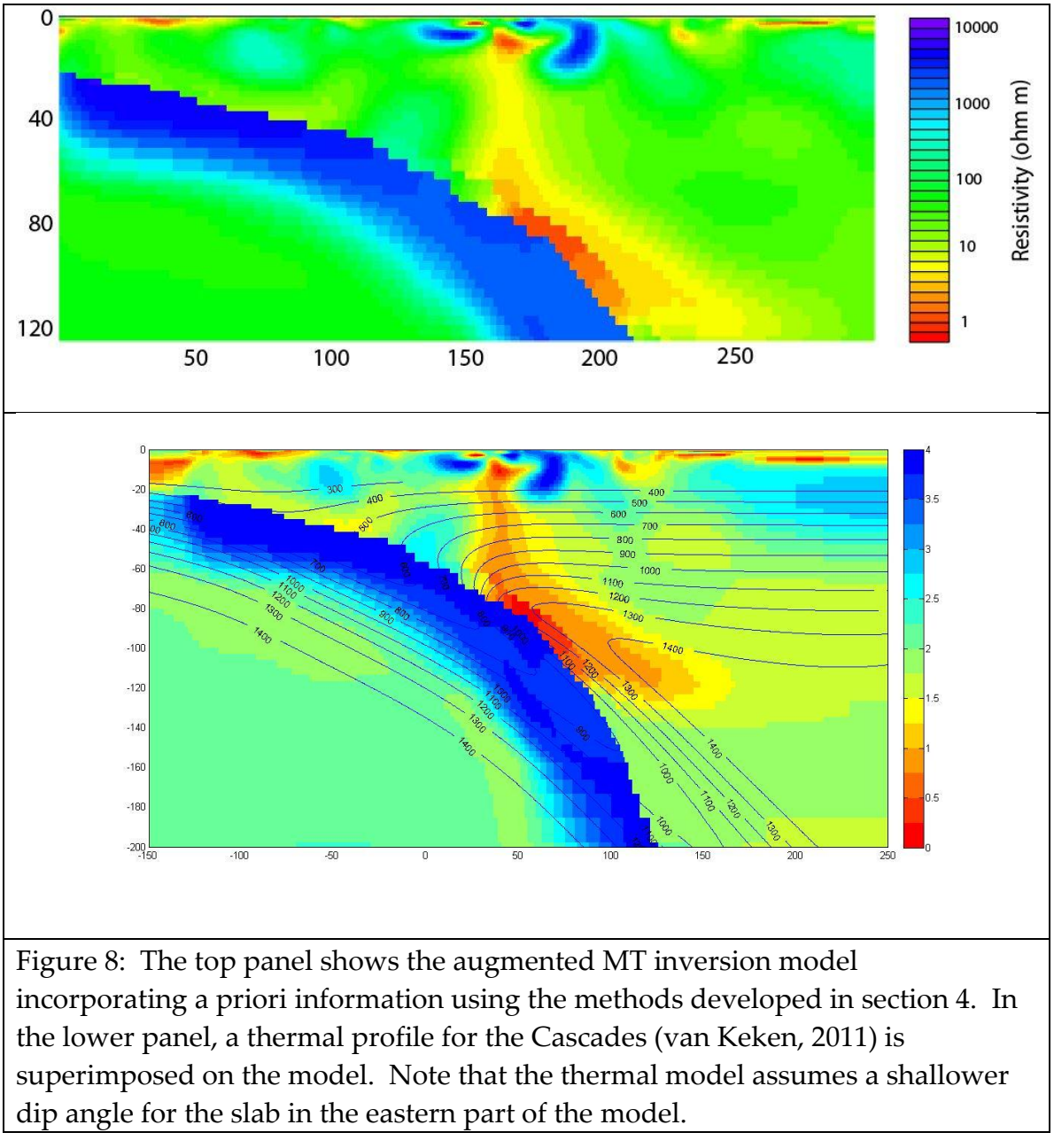

Figure 8: The top panel shows the augmented MT inversion model incorporating a priori information using the methods developed in section 4. In the lower panel, a thermal profile for the Cascades (van Keken, 2011) is superimposed on the model. Note that the thermal model assumes a shallower dip angle for the slab in the eastern part of the model.

the augmented model 1.89 which represents a significant improvement. The picture becomes even clearer when we look at a plot of rms values at different stations (fig. 9).

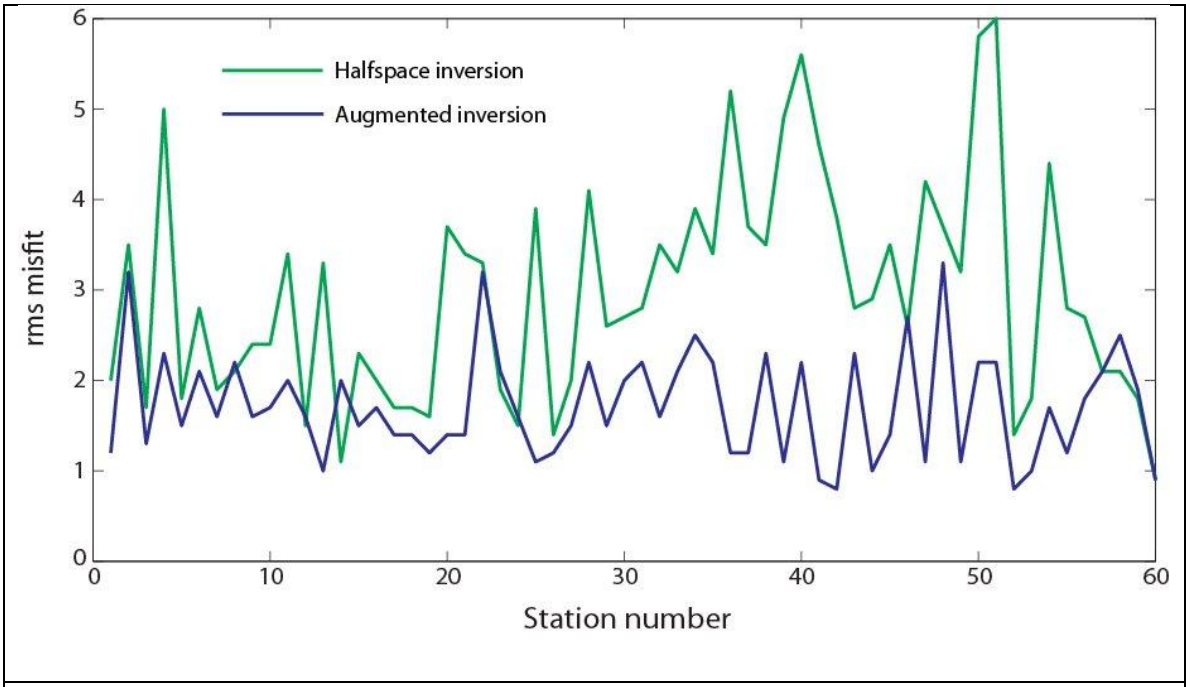

Figure 9: Plot of rms misfit at the 60 long period stations for the TM/TE/tipper models of the halfspace inversion from Chapter 3, and the augmented inversion incorporating the a priori information from the teleseismic migration using the methods developed throughout section 4 of this chapter. The overall rms values are 3.08 for the halfspace inversion, and 1.89 for the augmented inversion.

While the augmented model shows improvement in fit at almost every station, the effect is much more pronounced between stations 30 and 55, which correspond to horizontal distances of 150-275 km from the coast. By far the most striking differences between the two models between these markers is that in the augmented model the conductor is more intense and not separated from the resistive slab by any significant distance. Taken together, this strongly suggests

that the augmented model is more accurate, and that the imposed smoothness was largely responsible for the higher misfit in the halfspace model.

A second way to evaluate the accuracy of the models is by generating synthetic data from them, and inverting the synthetic data using the same parameters that were used for the original inversions. If a model is an accurate representation of the actual subsurface, then the synthetic data generated from the model should be a reasonable copy of the actual data, and inversions using the synthetic data should reasonably reproduce the results. Figure 10 shows the results of using the original halfspace model (fig. 10a) as the forward model. The synthetic data is then used to generate two new inversion models, one using the parameters from the original halfspace model, and the other using the parameters from the augmented model. These results are shown in fig. 10b and fig. 10c respectively.

The model generated from the halfspace reproduces many of the features of the original fairly well, but there are some significant differences as regards the conductor rising from depth. In the original model, the resistivity of the conductor rising from depths of 80-100 km is about 7 Ωm, a value that is maintained from depths of 35-100 km. For the reproduction, this resistivity is only found to depths of ~45 km, and at 100 km has risen to more than 20 Ωm.

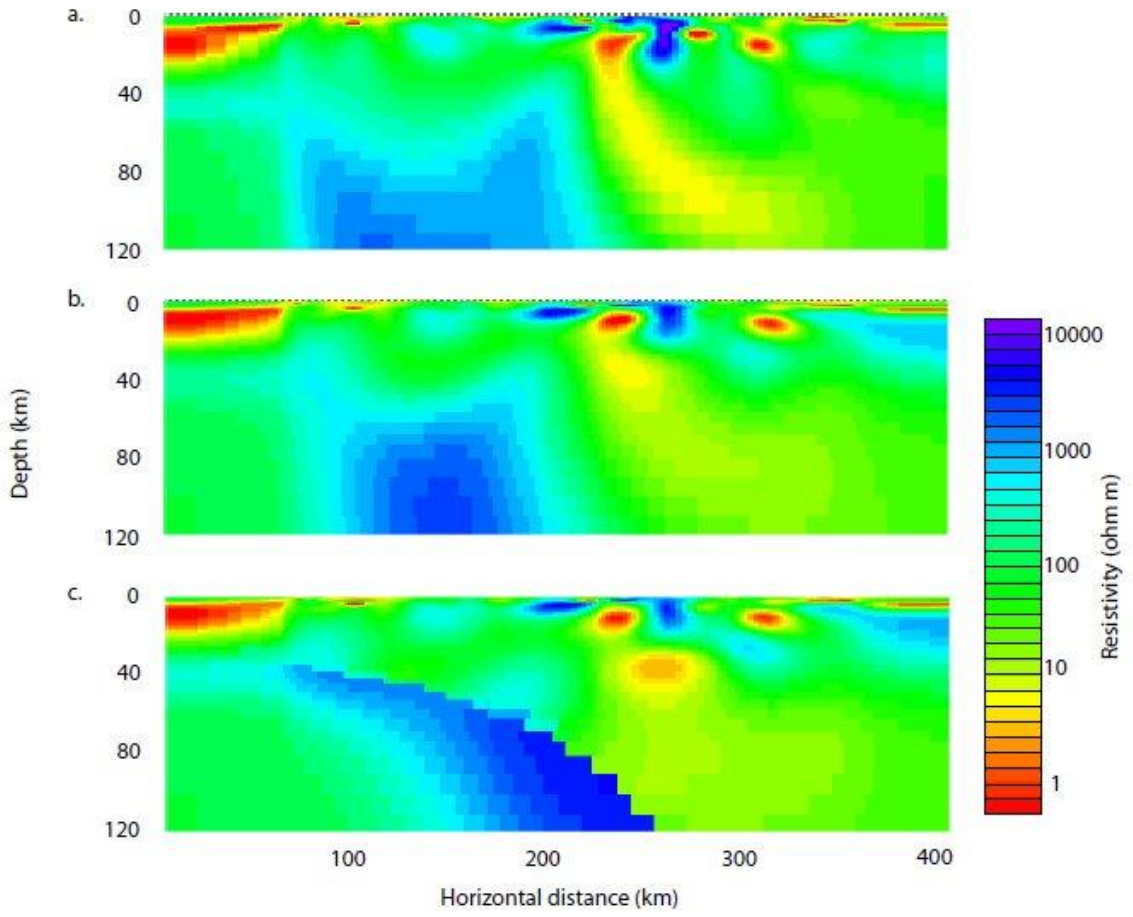

Figure 10: A series of models designed to test the accuracy of the halfspace model. Fig. 10a is used as the starting model to generate the synthetic data. Fig. 10b is the new inversion from a halfspace, and fig. 10c is the new inversion using the tools from the augmented inversion.

The dipping resistive feature has also retreated even further, suggesting a significant role for the imposed smoothness.

The augmented reproduction has even more difficulty. The resistivity at the top of the slab is ~20 Ωm compared to 2-3 Ωm in the original augmented model. A conductive (3 Ωm) artifact has appeared at a depth of 35 km within the column extending from the slab. If the original halfspace model had been accurate, then

imposition of the dipping resistor and tear zone would have concentrated the conductivity at the top of the slab.

Figure 11 shows the results of using the augmented model (fig. 11a) as the forward model for the synthetic data. The new reproduction models are then generated in the same way as before, with the first using parameters from the original halfspace model and the second from the augmented model. These results are shown in fig. 11b and fig. 11c respectively.

The reproduction in the halfspace model is quite good. Since we know what the forward model looked like, we can see the effect that the imposed smoothness has had on the deep conductor, and its appearance and resistivity values (7-8 Ωm) are very similar to what we see in the original halfspace model. The appearance of the resistive slab is also very similar, again suggesting that the imposed smoothness played a very similar role in this inversion as it did for the original halfspace. The other features of the model are also very similar, and we conclude that for this inversion, the reproduction is quite good.

Turning now to the augmented reproduction we see that the most conductive region of the column is at the top of the slab, with resistivities approaching 5 Ωm. While there is some concentration of conductivity at 35 km, the overall shape of the conductor is consistent with the original image. The other features in the

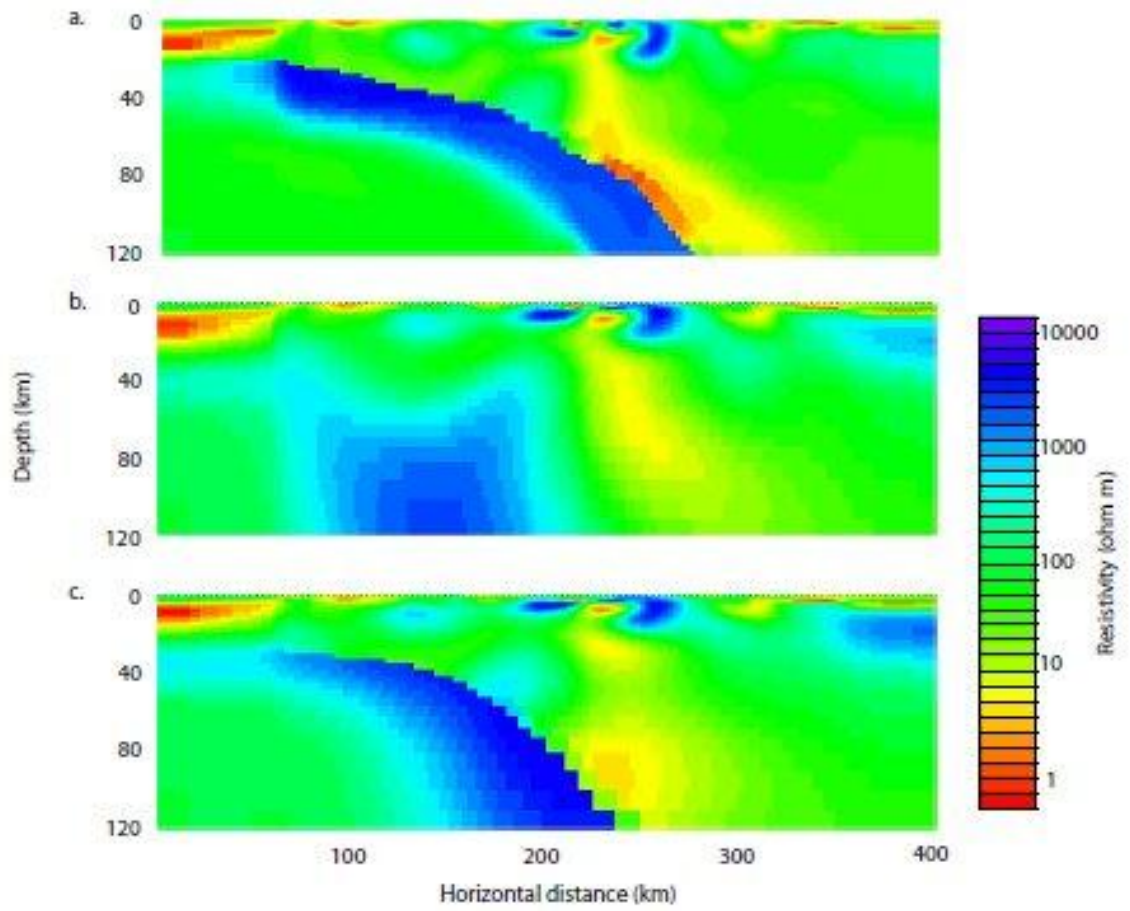

Figure 11: A series of models designed to test the accuracy of the augmented model. Fig. 11a is used as the starting model to generate the synthetic data. Fig. 11b is the new inversion from a halfspace, and fig. 11c is the new inversion using the tools from the augmented inversion.

model are also quite accurately reproduced. While the reproduction is certainly imperfect, the improvement relative to the models generated from the halfspace starting model provides a stark contrast, and we can only conclude that the augmented model is a superior representation of the conductivity structure of the subsurface.

6. Implications

Figure 12 shows the interpreted seismic migration image from the study conducted in Chapter 2, along with the augmented MT model from this chapter. The interpretation of both the seismic image and the original MT image was conducted in detail in the earlier chapters, so we will not repeat all of the previous analysis. The augmented MT image does however provide better constraints for some of the conductive features, and the implications pertaining to them needs to be addressed.

The conductor (A) that appears to be in contact with the slab at depths of 40 km which had a resistivity of 80 Ωm in the original value is now ~ 40 Ωm, more in line with what has been recorded in other subduction settings (Brasse et al., 2009, Evans et al., submitted), where it has been interpreted as migrating fluids that have been released from the subducting oceanic crust. This resistivity is consistent with a 0.5%wt of aqueous fluid given good connectivity; a tradeoff between higher fluid content and lower connectivity also produces an acceptable result (Pommier and LeTrong, 2007).

This conductor can also be seen to extend up-dip along the top of the slab, supporting an earlier interpretation of seismic results indicating the presence of pressurized channels related to episodic tremor and slip (ETS) (Abers et al., 2009,

Audet et al., 2010). This feature does not appear to be present along the EMSLAB transect (Evans et al., submitted), where ETS is also absent.

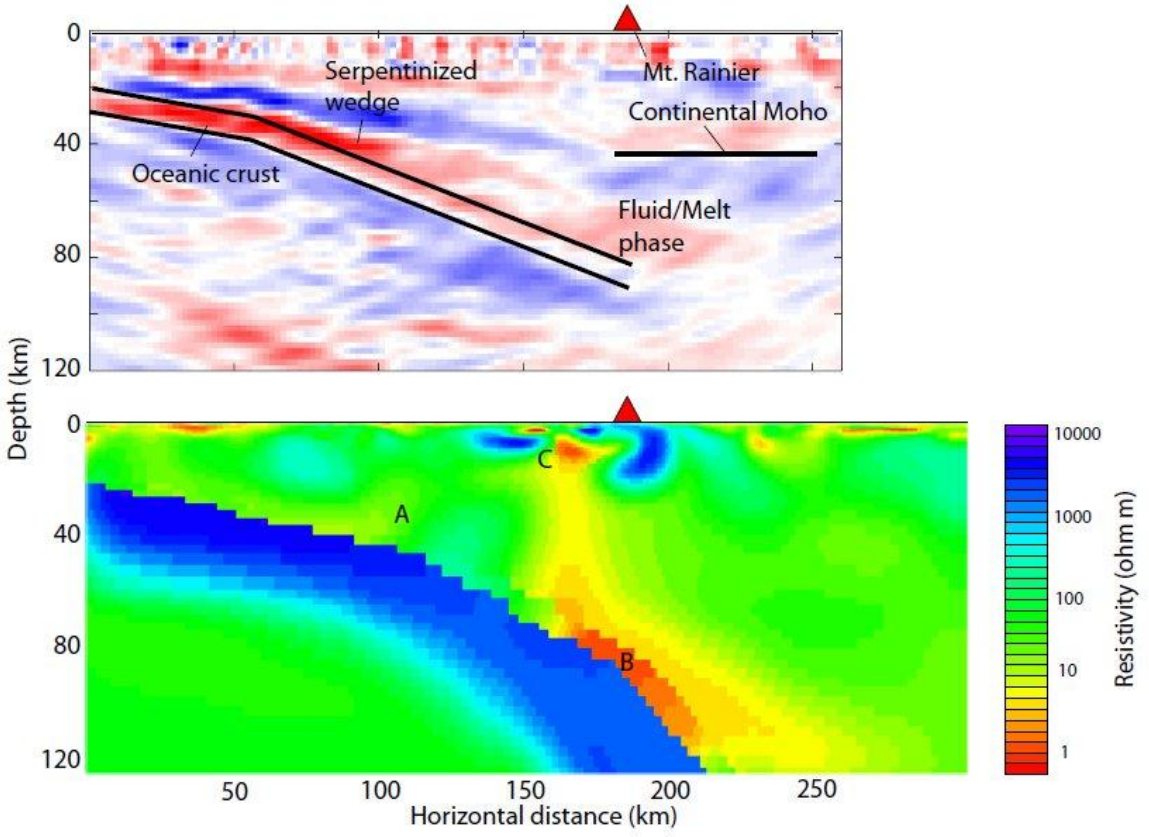

Figure 12: Final seismic migration and MT augmented inversion models for the CAFE experiment.

The deeper conductor (B) has low resistivities (~ 3 Ωm) along the top of the slab, but sensitivity tests on this feature suggest that the resistivity of this feature could be as high as 8 Ωm (see Appendix). In practice, at these depths even this higher value is not so easy to achieve. Based on an adaptation of the Vogel-Fulcher-Tammann equation (eq. 1) (Ni et al., 2011) and the HS+ bounds (eq. 2)

(Hashin and Shtrikman, 1962), we can calculate the bulk conductivity based on only temperature, weight percent water, and volume fraction of the melt.

$$\log \sigma = 2.172 - \frac{860.82 - 206.46\, W^{1/2}}{T - 1146.8} \quad (1)$$

W is the H_2O content in wt%, T is the temperature in K, and σ is the electrical conductivity in S/m.

$$\sigma = \sigma_2 \left[1 - \frac{3F_1(\sigma_2 - \sigma_1)}{3\sigma_2 - F_2(\sigma_2 - \sigma_1)}\right] \quad (2)$$

F_2 is the melt fraction, σ_2 is the conductivity in S/m of the more conductive phase, and σ is the bulk conductivity.

Table 1 shows the values of bulk resistivities calculated from equations 1 and 2 given a temperature of 1200 C, a background conductivity of .01 S/m, and varying wt% H_2O from 0-5%, and melt fraction from 1-4%.

The conductor appears to be in contact with the slab from depths of 75-105 km, corresponding to the range of dehydration for chlorite harzburgite in the mantle (Hacker et al., 2003) and the transition of metastable gabbro to eclogite (John and Schenk, 2003) for Cascadia (van Keken et al., 2011). This conductor

		Weight percent H_2O				
		0 wt.%	1 wt.%	2 wt.%	3 wt%	4 wt%
Melt fraction	1%	81	51	36	26	20
	2%	69	34	22	15	11
	3%	60	26	16	11	7
	4%	52	20	12	8	6
	5%	47	17	10	7	5

Table 1: Bulk resistivity (Ωm) of fluid/melt phase at the top of the slab for a selection of melt fraction and water content

extends upward with a resistivity of ~ 7-10 Ωm until it connects with the shallow conductor (C) of resistivities between 3-4 Ωm that we interpret to be a magma chamber that feeds Mt. Rainier.

While the smoothness imposed on standard MT inversions is a desirable feature that stabilizes the inversion and minimizes the introduction of structure that is not required by the data, the penalty it applies to abrupt transition can have a detrimental effect on resolving certain features. In this chapter, we examine how this assumption of smoothness can impact the final inversion model, methods such as the imposition of resistivities and tear zones that can be used to mitigate those effects, and ways to evaluate which set of assumptions provides a more accurate inversion model. Finally, we applied the lessons to the

CAFE dataset, resulting in a more accurate model, particularly with respect to the constraints for the conductive features in the model.

References for Chapter 4

Abers, G.A., MacKenzie, L.S., Rondenay, S., Zhang, Z., Wech, A.G., Creager, K.C., 2009. Imaging the source region of Cascadia tremor and intermediate-depth earthquakes. Geology 37, 1119-1122.

Audet, P., Bostock, M.G., Boyarko, D.C., Brudzinski, M.R., Allen, R.M., 2010. Slab morphology in the Cascadia fore arc and its relation to episodic tremor and slip. J. Geophys. Res. 115, B00A16.

Baba, K., Chave, A.D., Evans, R.L., Hirth, G., Mackie, R.L., 2006. Mantle dynamics beneath the East Pacific Rise at 17°S: Insights from the Mantle Electromagnetic and Tomography (MELT) experiment. J. Geophys. Res. 111, B02101, doi:10.1029/2004JB003598.

Bostock M.G., Hyndman, R.D., Rondenay, S., Peacock, S.M., 2002. An inverted continental Moho and serpentinization of the forearc mantle. Nature 417, 536-538.

Brasse, H., Kapinos, G., Mutschard, L., Alvarado, G.E., Worzewski, T., Jegen, M., 2009. Deep electrical resistivity structure of northwestern Costa Rica. Geophys. Res. Lett., v. 36, L02310, doi:10.1029/2008GL036397.

de Groot-Hedlin, C., and Constable, S., 1990. Occam's inversion to generate smooth, two-dimensional models from magnetotelluric data. Geophysics 55, 1613-1624.

de Groot-Hedlin, C. and Constable, S., 2004. Inversion of magnetotelluric data for 2D structure with sharp resistivity contrasts. Geophysics 69, 78-86.

Evans, R.L., Wannamaker, P., McGary, R.S., Elsenbeck, J., submitted 2012. Electrical structure of the Central Cascadia subduction zone: The EMSLAB Lincoln line revisited.

Gallardo L.A., and Meju, M.A., 2007. Joint two-dimensional cross-gradient imaging of magnetotelluric seismic traveltime data for structural and lithological classification. Geophys. J. Int, 169, 1261-1272.

Hacker, B.R., Abers, G.A., Peacock, S.M., 2003. Subduction factory 1. Theoretical mineralogy, densities, seismic wave speeds, and H_2O contents. J. Geophys. Res. 108(B1), 2029, doi:10.1029/2001JB001127.

Hashin, Z., Shtrikman, S., 1962. A variational approach to the theory of the effective magnetic permeability of multiphase materials. J. Appl. Phys. 33, 3125-3131.

Helffrich, G., 1996. Subducted lithospheric slab velocity structure: Observations and mineralogical inferences, in Bebout, G., et al., eds., Subduction top to bottom: American Geophysical Union Geophysical Monograph 96, 215-222.

Hildreth, W., 2007. Quaternary magmatism in the Cascades- Geologic perspectives, USGS professional paper 1744.

John T., Schenk, V., 2003. Partial eclogitization of gabbroic rocks in a late Precambrian subduction zone (Zambia): prograde metamorphism triggered by fluid infiltration. Contrib. Mineral Petrol. 146, 174-191.

Jones, A.G., et al., 2009. Velocity-conductivity relationshipes for mantle mineral assemblages in Archean cratonic lithosphere based on a review of laboratory data and Hashin-Shtrikman external bounds. Lithos 109, 131-143.

Li, S., Unsworth, M.J., Booker, J.R., Wei, W., Tan, H., Jones, A.G., 2003. Partial melt or aqueous fluid in the mid-crust of Southern Tibet? Constraints from INDEPTH magnetotelluric data. Geophys. J. Int. 153, 289-304.

Matsuno, T., et al., 2010. Upper mantle electrical resistivity structure beneath the central Mariana subduction system, Geochem. Geophys. Geosyst., 11, Q09003, doi:10.1029/2010GC003101.

Mehanee S. and Zhdanov, M., 2002. Two-dimensional magnetotelluric inversion of blocky geoelectrical structures. J. Geophys. Res. 107, B4.

Miensopust, M.P., Jones, A.G., Muller, M.R., Evans, R.L., 2010. Lithospheric structures and geometries in northeastern Botswana revealed through SAMTEX magnetotelluric profiling. J. Geophys. Res. - Solid Earth, **116**, B02401, doi:10.1029/2010JB007740.

Moorkamp, M., et al., 2007. Joint inversion of teleseismic receiver functions and magnetotelluric data using a genetic algorithm: Are seismic velocities and electrical conductivities compatible? Geophys. Res. Lett., 34, L16311.

Ni, H., Keppler, H., Behrens, H., 2011. Electrical conductivity of hydrous basaltic melts: implications for partial melting in the upper mantle. Contrib. Mineral Petrol. 162, 637-650.

Parker, R.L., 1994. Geophysical Inverse Theory (BOOK). Princeton University Press, Princeton, N.J.

Pommier A. and LeTrong E., 2011. "SIGMELTS": A web-portal for electrical conductivity calculations in geosciences. Computers and Geosciences, doi:10.1016/j.cageo.2011.01.002.

Rodi, W.L., and Mackie, R. L., 2001. Nonlinear conjugate gradients algorithm for 2-D magnetotelluric inversion. Geophysics, 66, 174-187.

Rodi, W.L, and Mackie, R.L., 2012. The inverse problem. From The Magnetotelluric Method (BOOK), edited by Chave, A.D., and Jones, A.D., Cambridge University Press, Cambride, U.K.

Rondenay, S., Bostock, M.G., Shragge, J., 2001. Multiparameter two-dimensional inversion of scattered teleseismic body waves. 3. Application to the Cascadia 1993 data set. J. Geophys. Res. 106, 30795-30807.

Simpson, F., and Bahr, K., 2005. Practical Magnetotellurics (BOOK). Cambridge University Press, Cambridge, U.K.

Schwalenburg, K., Rath, V., Haak, V., 2002. Sensitivity studies applied to a two-dimensional resistivity model from the central Andes. Geophys. J. Int., 150, 673-686.

Smith, J.T., et al., 1999. Sharp boundary inversion of 2D magnetotelluric data. Geophysical Prospecting, 47, 469-486.

Stanley, William D. et al., 1990. Deep Crustal Structure of the Cascade Range and Surrounding Regions from Seismic Refraction and Magnetotelluric Data. Journal of Geophysical Research, 95, B12, 19419-19438.

Stockstill, K.R., Vogel, T.A., Sisson, T.W., 2002. Origin and emplacement of the andesite of Burroughs Mountain, a zoned, large-volume lava flow at Mount Rainier, Washington, USA. J. Volcanology and Geothermal Res., 119, 275-296

van Keken, P.E., Hacker, B.R., Syracuse, E.M., and Abers, G.A., 2011. Subduction factory: 4. Depth-dependent flux of H_2O from subducting slabs worldwide. J. Geophys. Res. 116, B01401.

Worzewski, T., Jegen, M., Kopp, H., Brasse, H., Castillo, W.T., 2011. Magnetotelluric image of the fluid cycle in the Costa Rican subduction zone. Nature Geoscience, 4, 108-111.

Appendices

The appendices are presented as a series of figures designed to provide a deeper look into the mechanics of the work done while constructing this thesis. The first appendix supports the seismic work, presenting the steps involved in the preprocessing of the seismic data and the migrated images generated for each of the 64 events that were used in the final images. The second appendix supports the MT work, presenting pseudo-sections derived from the original (processed) data, difference pseudo-sections comparing the augmented model with the standard model, and an inversion model generated in the absence of a smoothing parameter to support the theory presented in Chapter 4. Additionally, some of the most important sensitivity tests are included, such as the test for robustness of the vertical conductive corridor that connects the two most prominent conductors and the allowable range test for the conductivities at the top of the slab. Finally, some synthetic models are included that explore the ramifications of imposing features and/or tear zones based on faulty a priori information.

5.1 Figures supporting seismic migration work

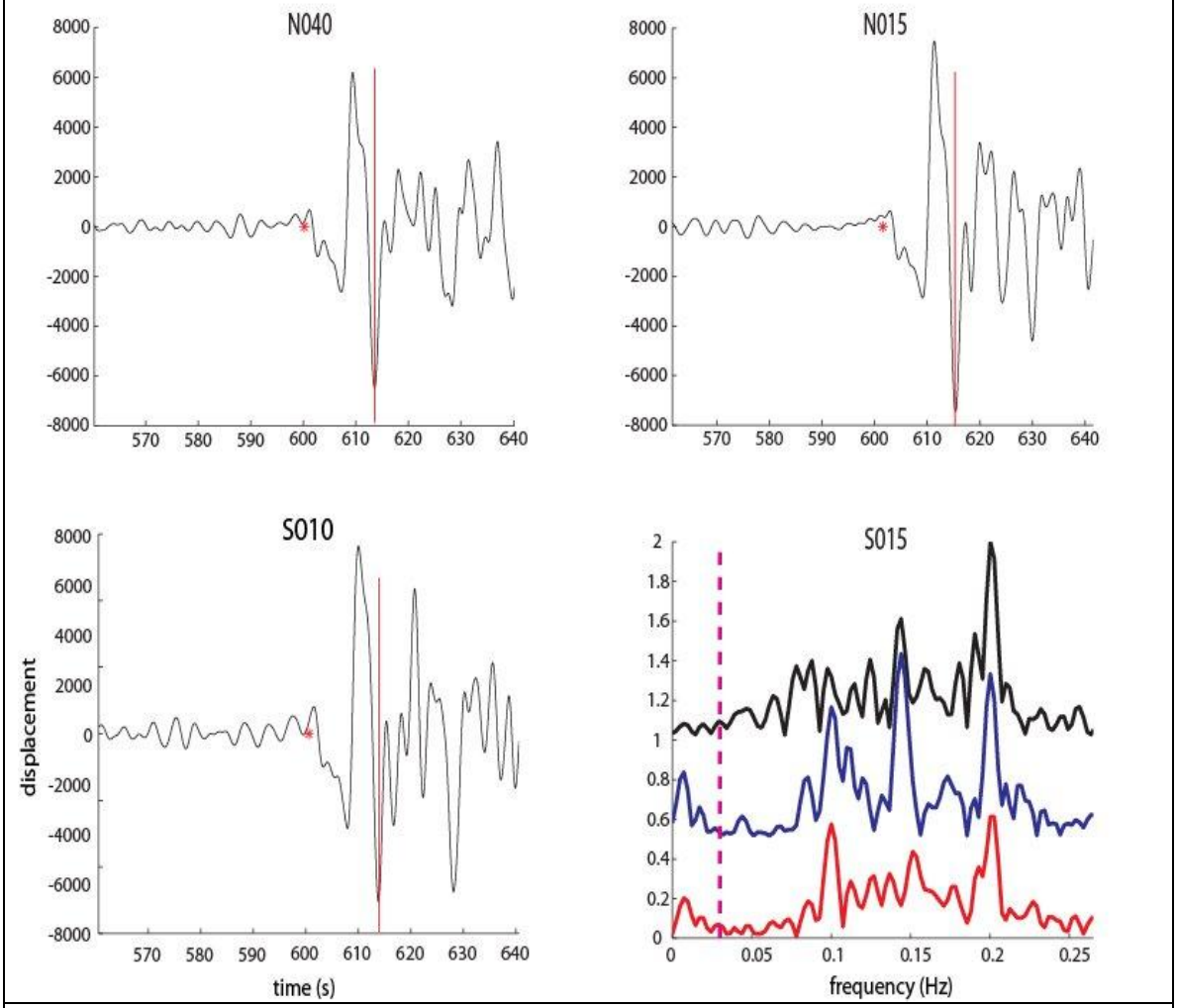

Figure 1: After rotation of the wavefield and application of the free surface transfer matrix, the next step in the pre-processing involved the manual inspection of the waveform for each of the 41 stations for approximately 250 prospective events. The first three panels of this figure show typical waveforms, taken from stations N040, N015, and S010 for event 20082541308 (the event designator consists of the year, Julian Date, hour, and minute of the event). A prominent peak was then selected that could be readily identified for each station (shown in the figure as the vertical red line). Manual inspection of the waveforms was also conducted in the frequency domain (the fourth panel shows station S015 for the same event). In general, the frequencies were filtered to pass those between 0.03 and 0.5 Hz, but some stations, particularly those with excessive low frequency noise, required additional filtering.

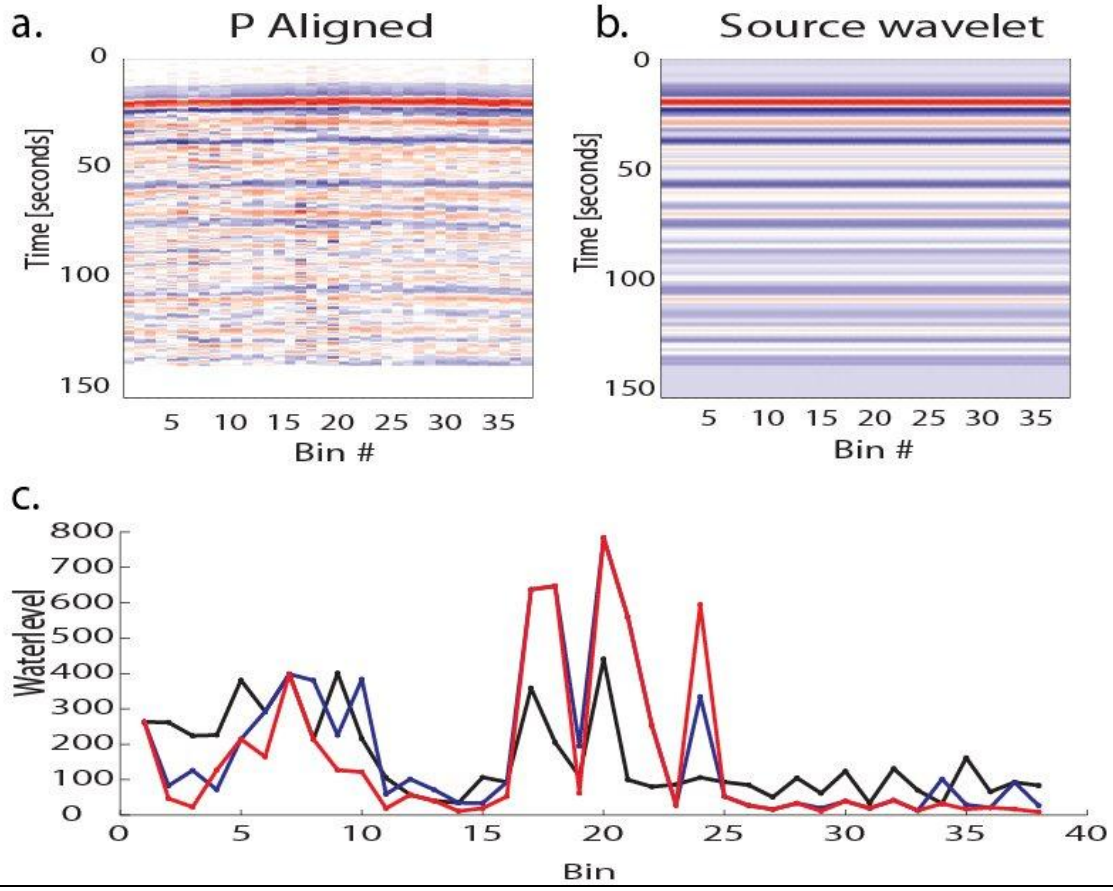

Figure 2: The initial picks of prominent peaks shown in figure 1 ensure that the start times for each event are reasonably well aligned between stations. This alignment is then refined using a multi-channel cross-correlation technique- figure 2a shows the aligned waveforms for 39 stations for event 20082541308. The next step in the pre-processing is the application of eigenimage decomposition to identify the correlated parts of these waveforms, under the assumption that these correlated parts provide a good estimate of the source waveform. The source waveform for event 20082541308 is shown in figure 2b. The next step is to deconvolve the estimated incident wavefield from the components of the scattered wavefield to obtain the normalized scattered wavefield (corresponding to a source impulse). In order to make this deconvolution stable, a "waterlevel" proportional to noise is used in the denominator of the deconvolution. For this experiment, we used a station specific waterlevel (developed by Fred Pearce at MIT) so that noisy stations would not cause loss of data for all of the stations for a given event. Figure 2c shows the waterlevel plot for event 20082541308.

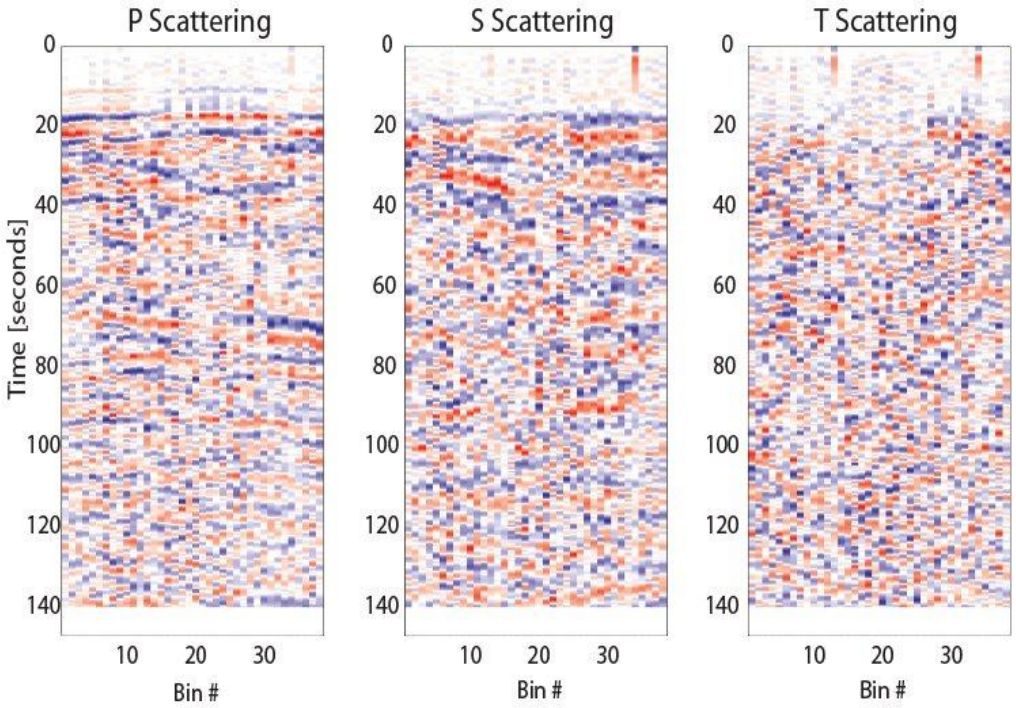

Figure 3: The deconvolution of the estimated source wavefield results in a three-component estimate of the scattered wavefield for a specific event. These scattered wavefields are then migrated back to find the scattering points in the subsurface. This figure shows the scattered wavefields for event 20082541308.

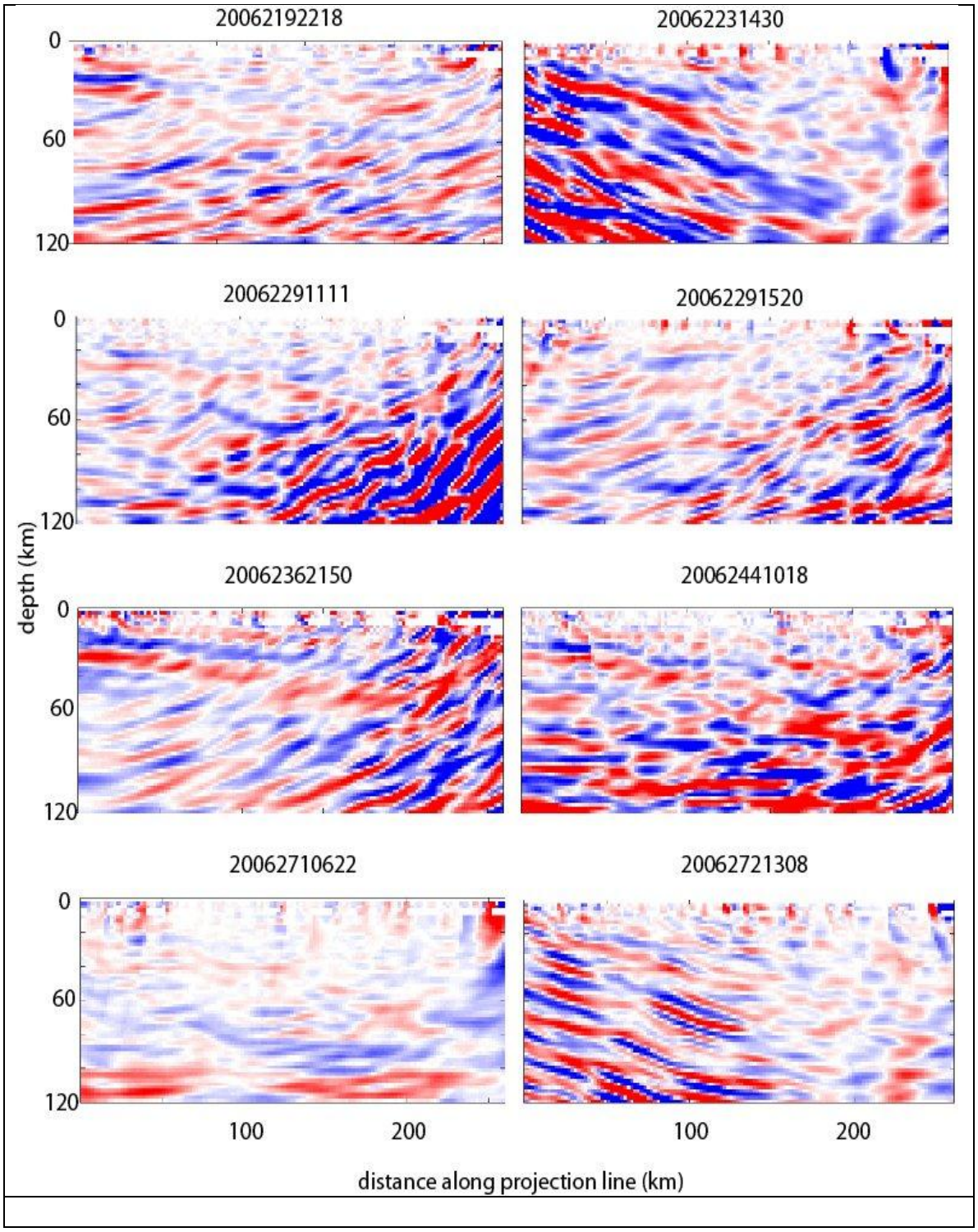
20062192218
20062231430
20062291111
20062291520
20062362150
20062441018
20062710622
20062721308
0
60
120
depth (km)
100
200
distance along projection line (km)

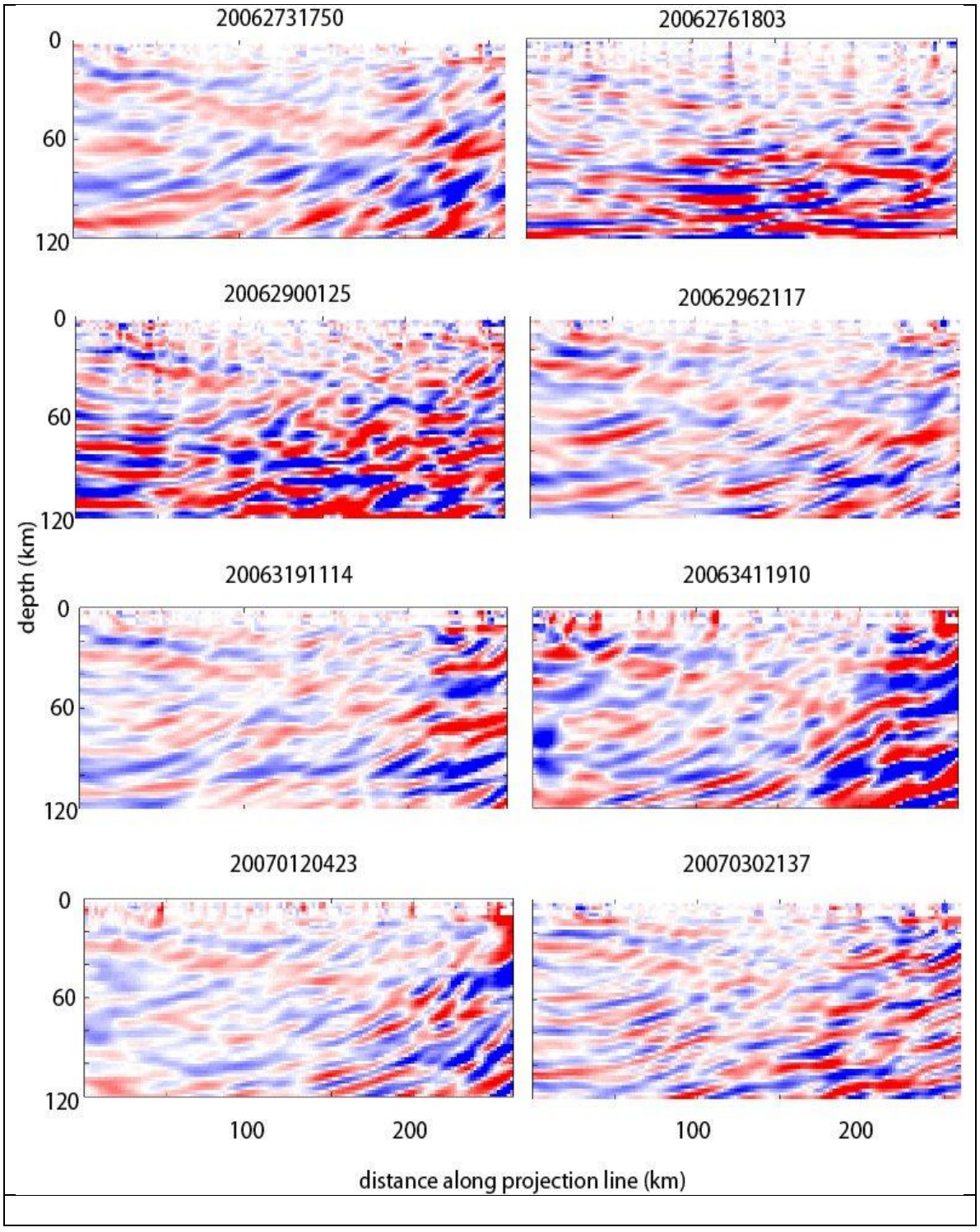
20062731750
20062761803
20062900125
20062962117
20063191114
20063411910
20070120423
20070302137
0
60
120
depth (km)
100
200
distance along projection line (km)

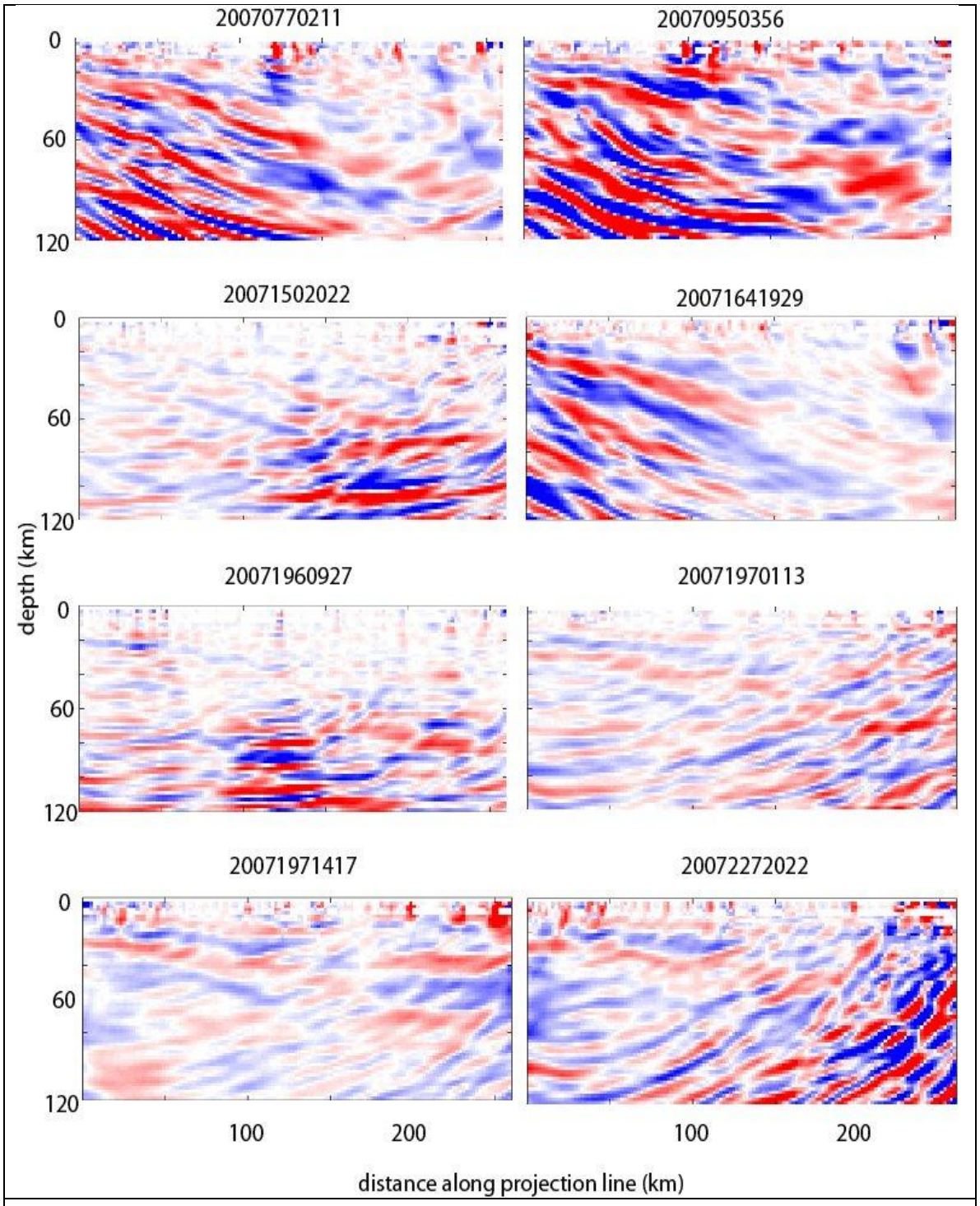
20070770211
20070950356
20071502022
20071641929
20071960927
20071970113
20071971417
20072272022
0
60
120
depth (km)
100
200
distance along projection line (km)

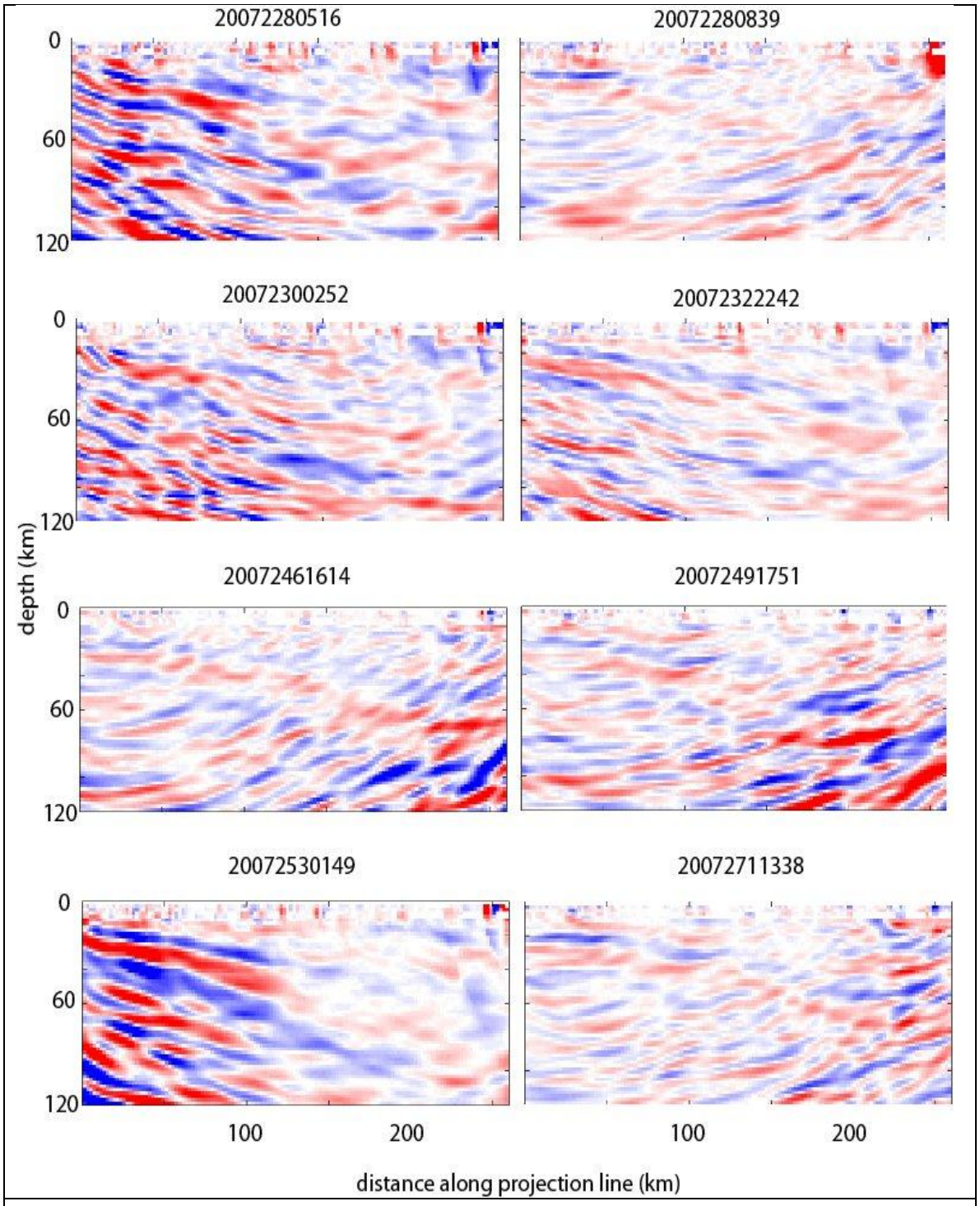
20072280516
20072280839
20072300252
20072322242
20072461614
20072491751
20072530149
20072711338
0
60
120
depth (km)
100
200
distance along projection line (km)

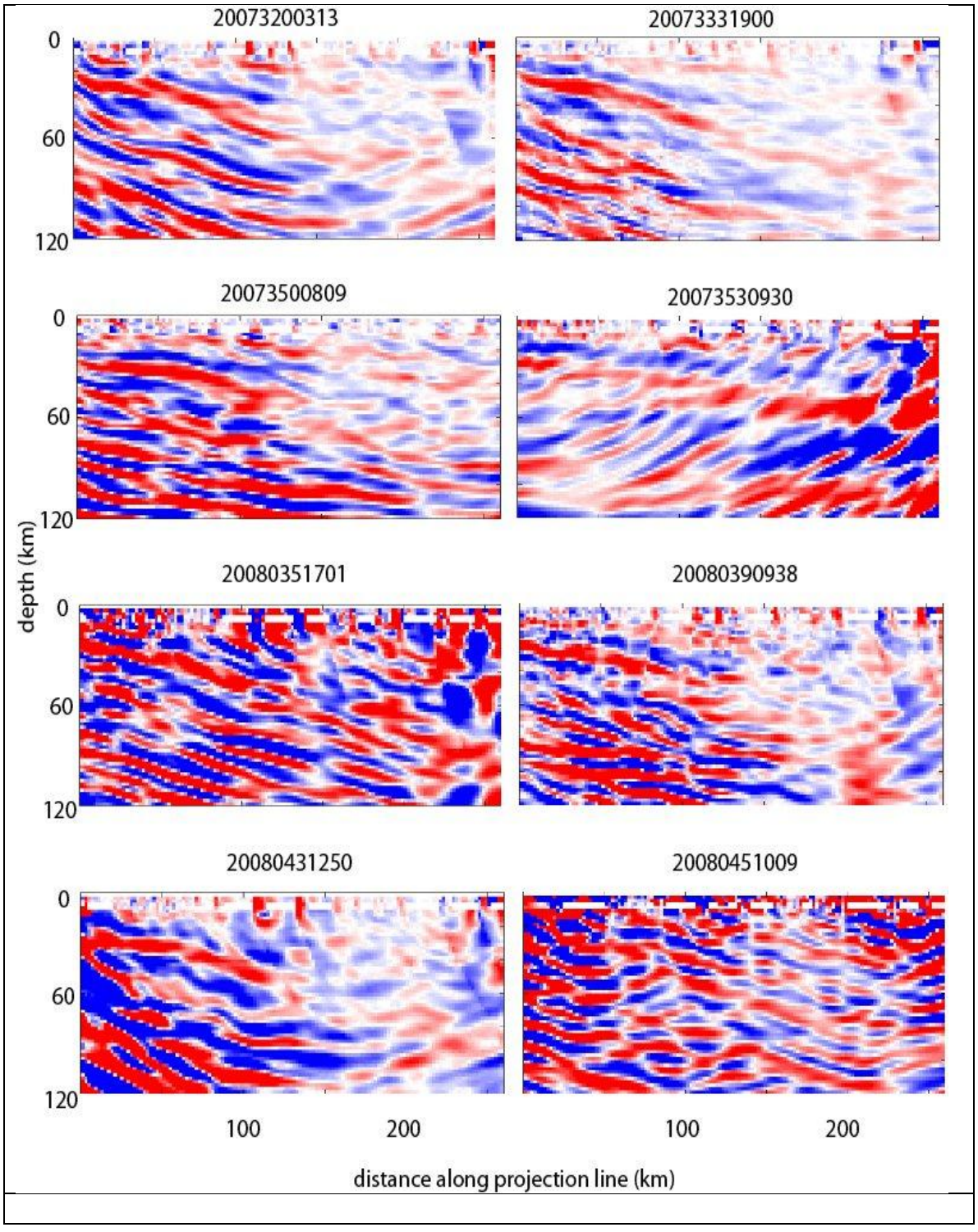
20073200313
20073331900
20073500809
20073530930
20080351701
20080390938
20080431250
20080451009
0
60
120
depth (km)
100
200
distance along projection line (km)

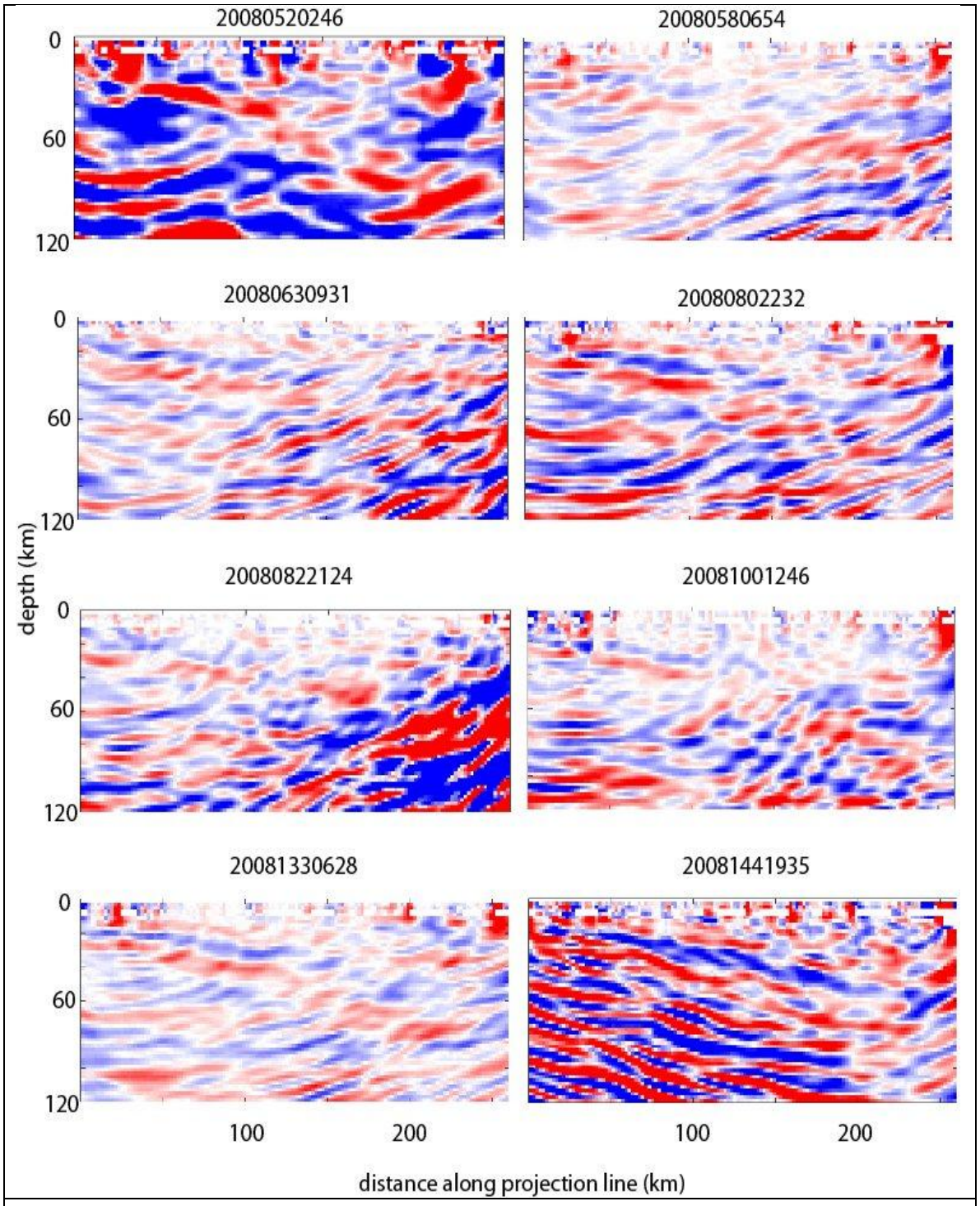
20080520246
20080580654
20080630931
20080802232
20080822124
20081001246
20081330628
20081441935
0
60
120
depth (km)
100
200
distance along projection line (km)

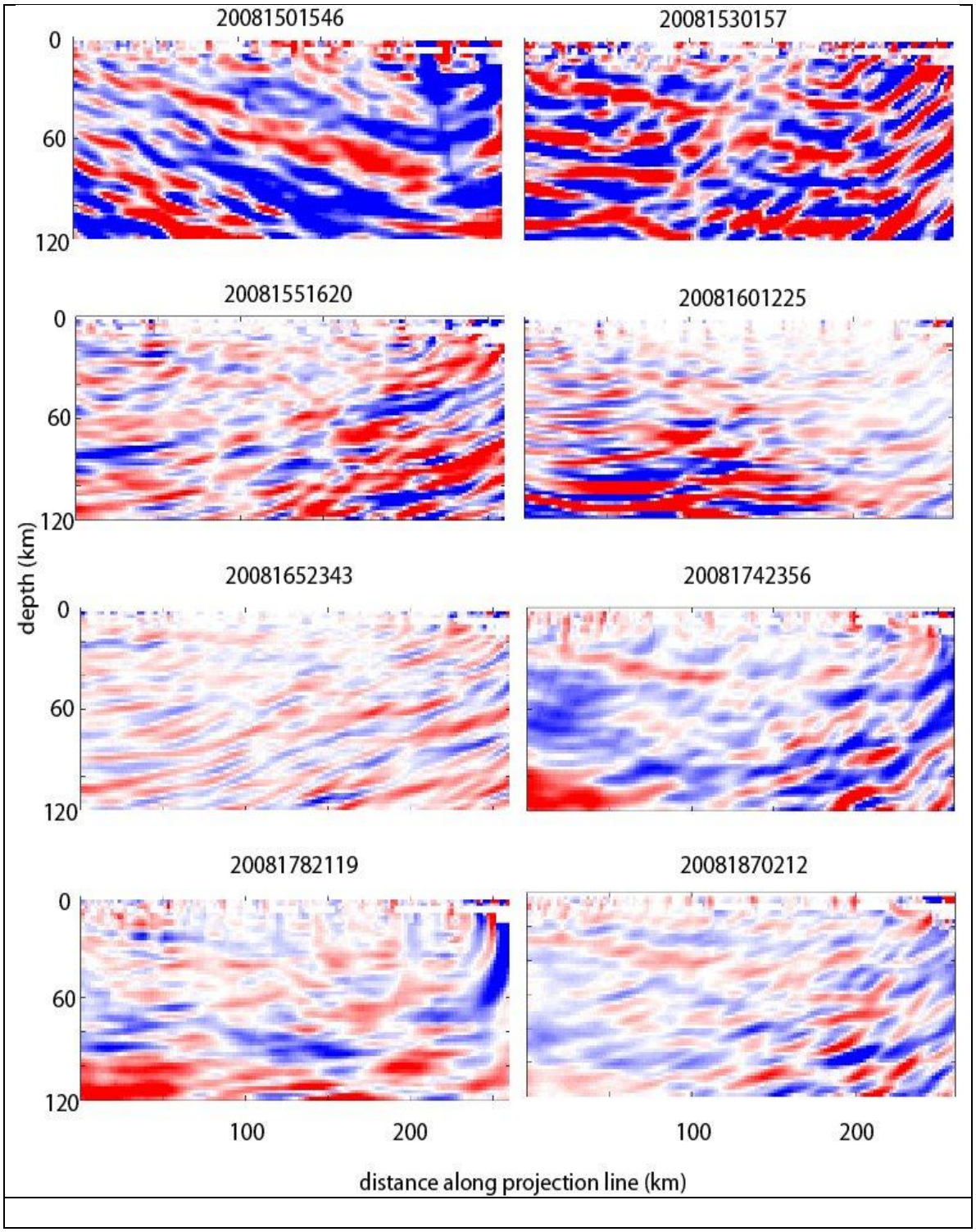
20081501546
20081530157
20081551620
20081601225
20081652343
20081742356
20081782119
20081870212
0
60
120
depth (km)
100
200
distance along projection line (km)

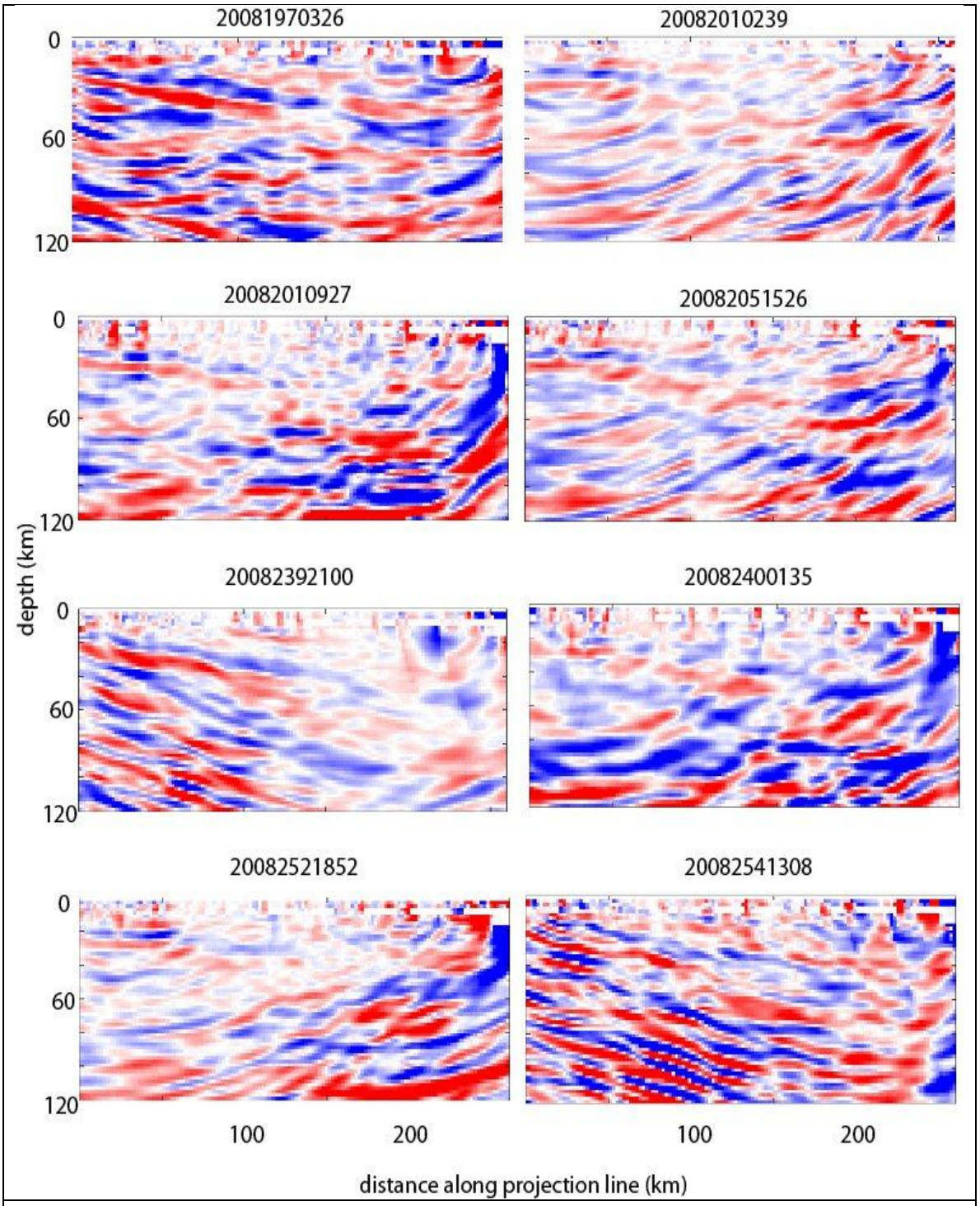

Figure 4: The individual composite images for each of the 64 events that were used to generate the primary composite image. The modes used for each of these images are given in the supplemental table to Chapter 2.

5.2 Additional figures supporting magnetotellurics work

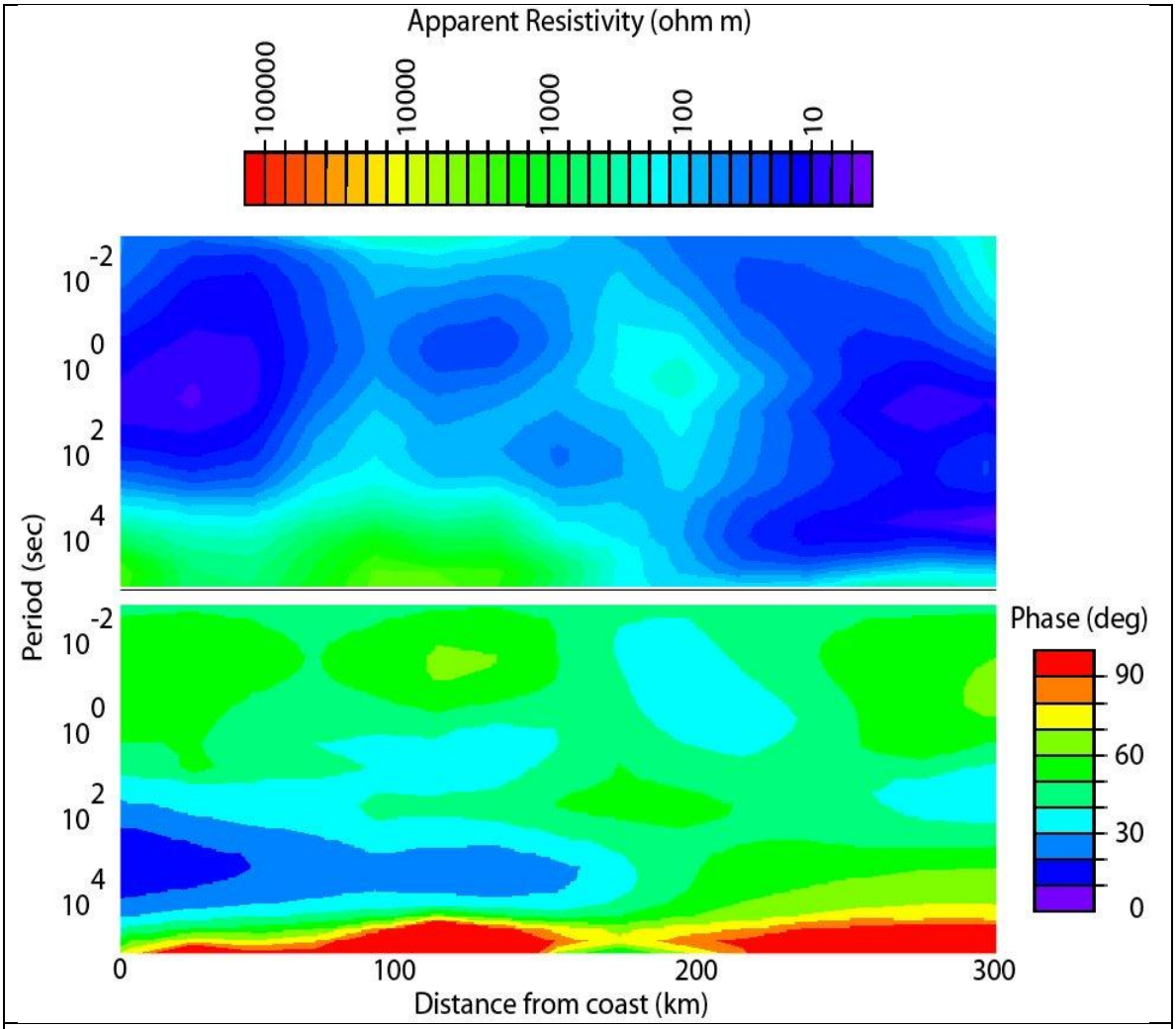

Figure 5: TM mode pseudo section for the CAFE MT data. The upper figure shows apparent resistivity and the lower figure shows phase. All of the pseudo section models (figures 5-8) are limited horizontally to correspond with the surface covered by the CAFE MT array.

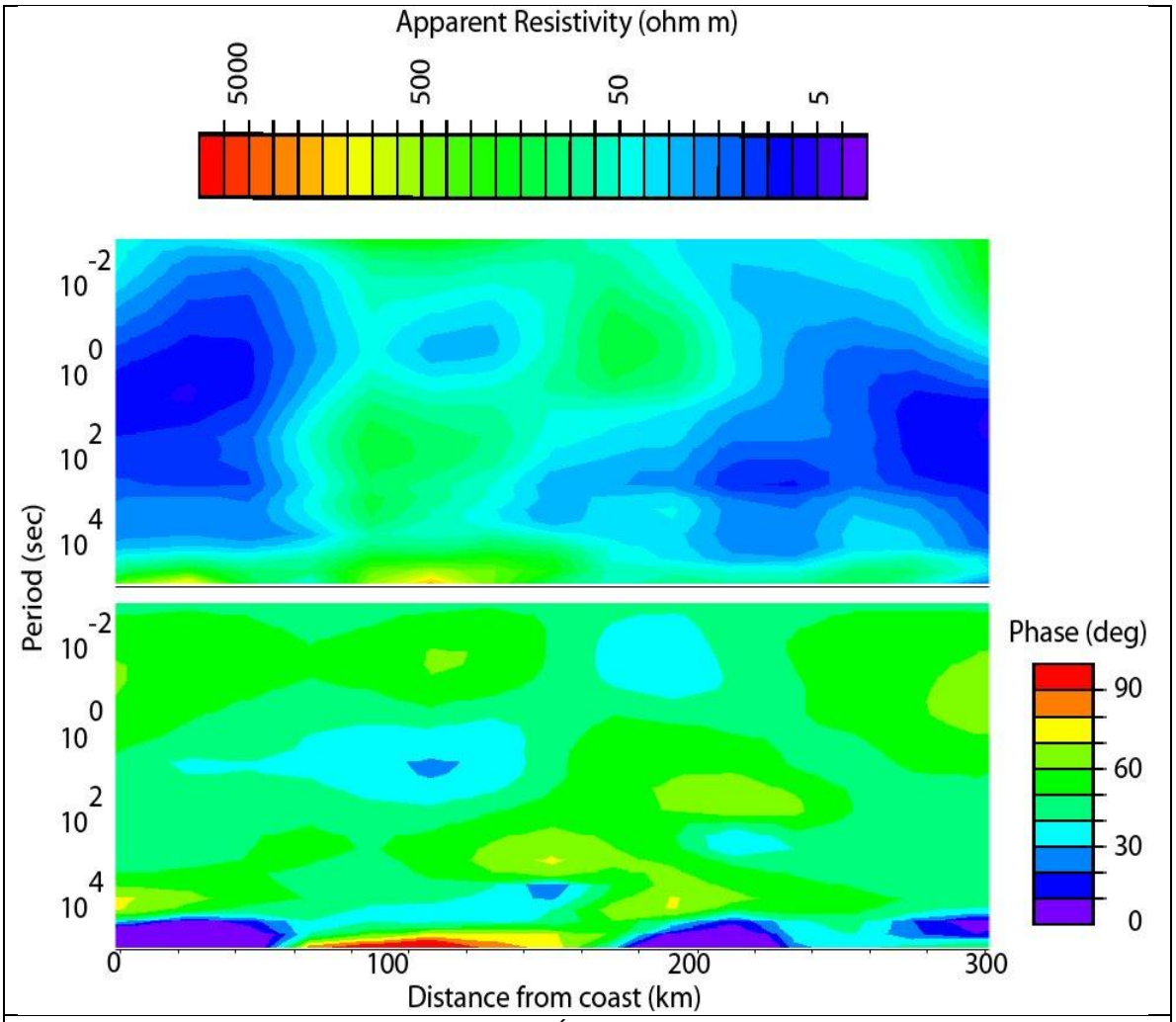

Figure 6: TE mode pseudo section for the CAFÉ MT data. The upper figure shows apparent resistivity and the lower figure shows phase.

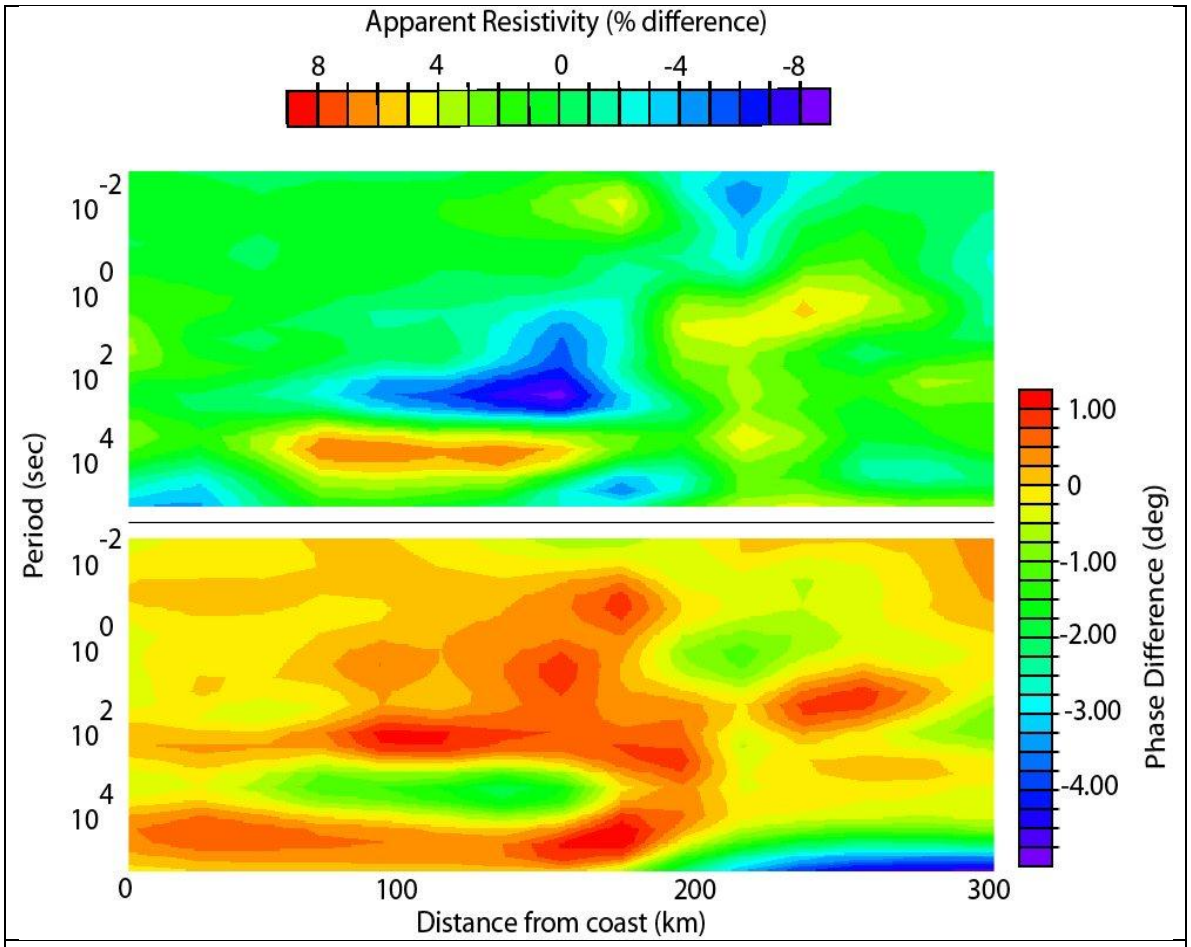

Figure 7: Pseudo sections can also be generated from model derived synthetic data, and models can be compared using difference pseudo sections. This figure shows the difference pseudo section for the TM mode between the augmented and standard models from Chapter 3. Both models fit the data very well in the TM, and the differences between them are quite small.

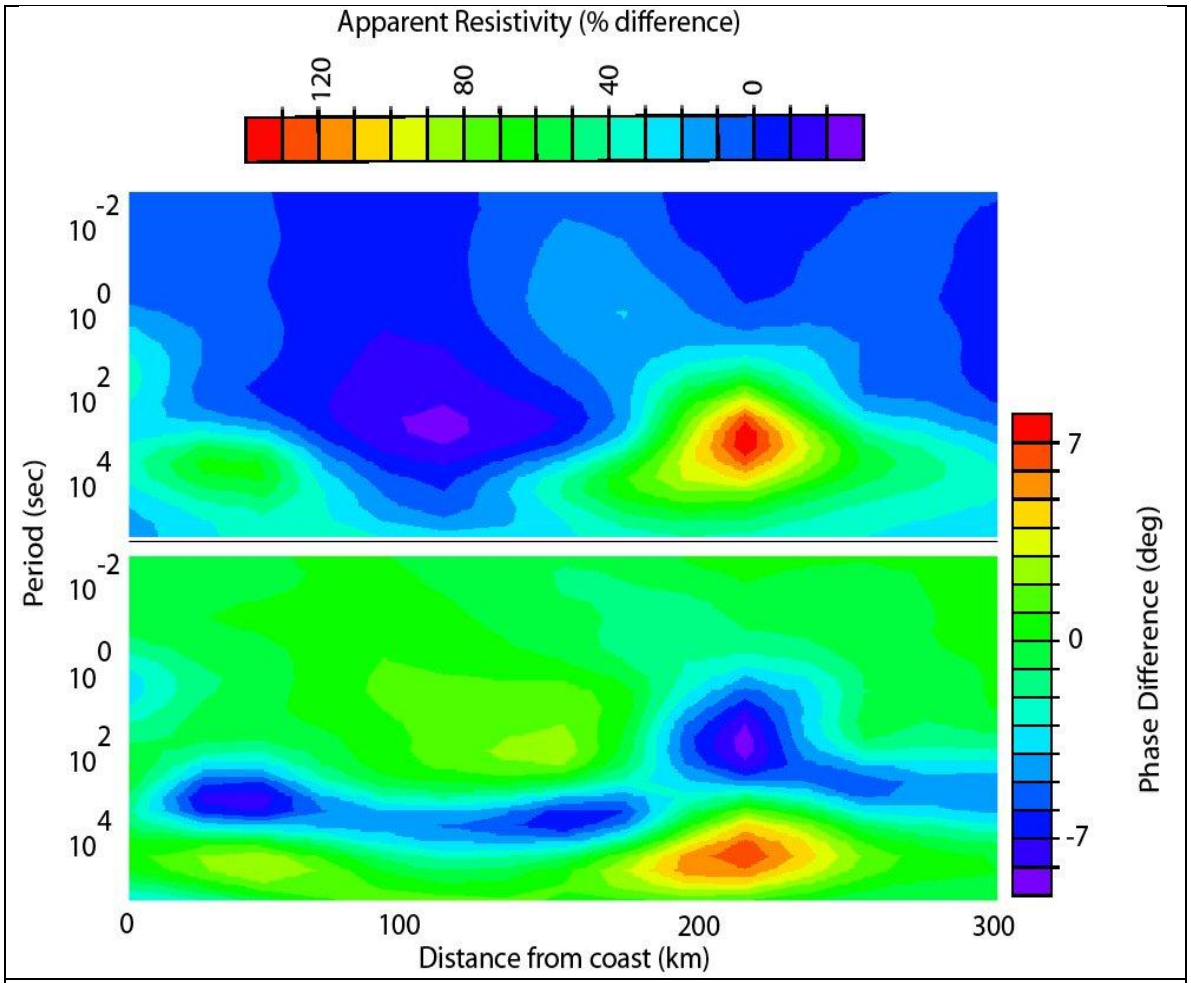

Figure 8: This figure shows the difference pseudo section for the TE mode between the augmented and standard models from Chapter 3. The differences here are significantly more pronounced that they were for the TM mode, which is not unexpected given the poor TE fit for the standard model. It is clear again here that the most important differences occur between 100-1000 seconds roughly 200 km from the coast, consistent with the fluid release from the slab at depth.

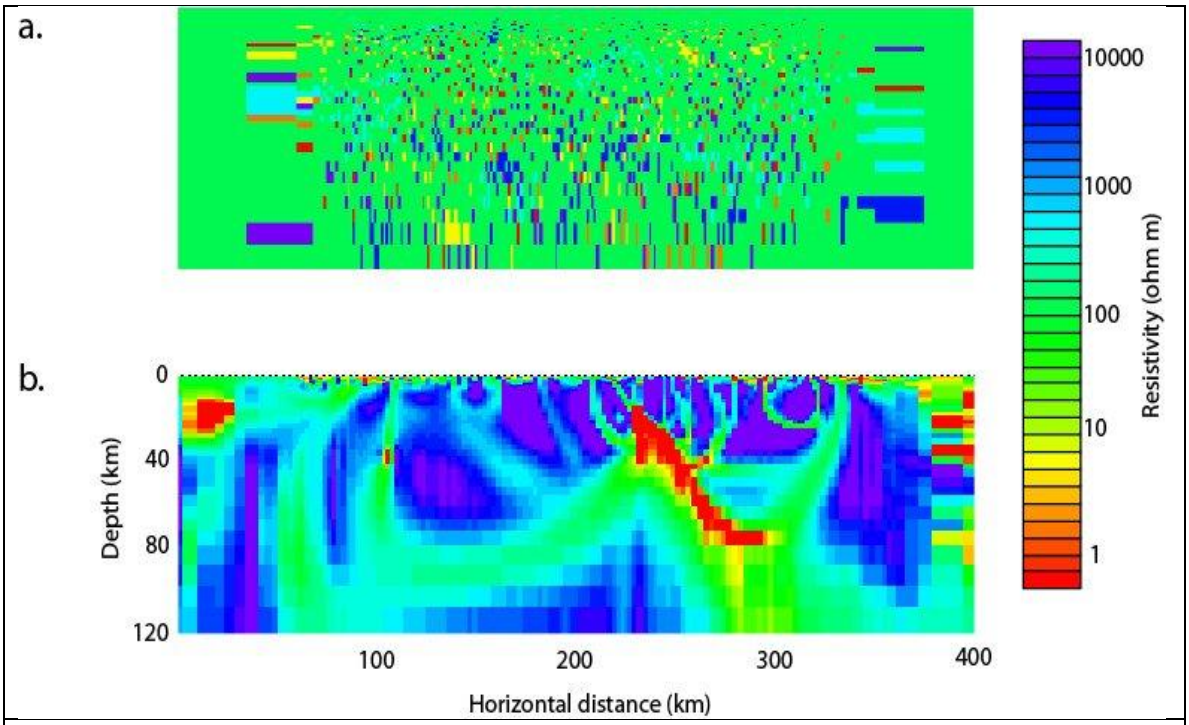

Figure 9: Figure 9a shows an example of the sort of model that is ruled out by the use of a smoothness driven stabilizing functional in an MT inversion. Figure 9b shows an inversion model generated from the CAFE MT data for which the stabilizing parameter has been collapsed by imposing a tear zone over the entire cross-section. The tau parameter was also set to the minimum 0.01 so as to have the smallest possible impact on the direction of the inversion.

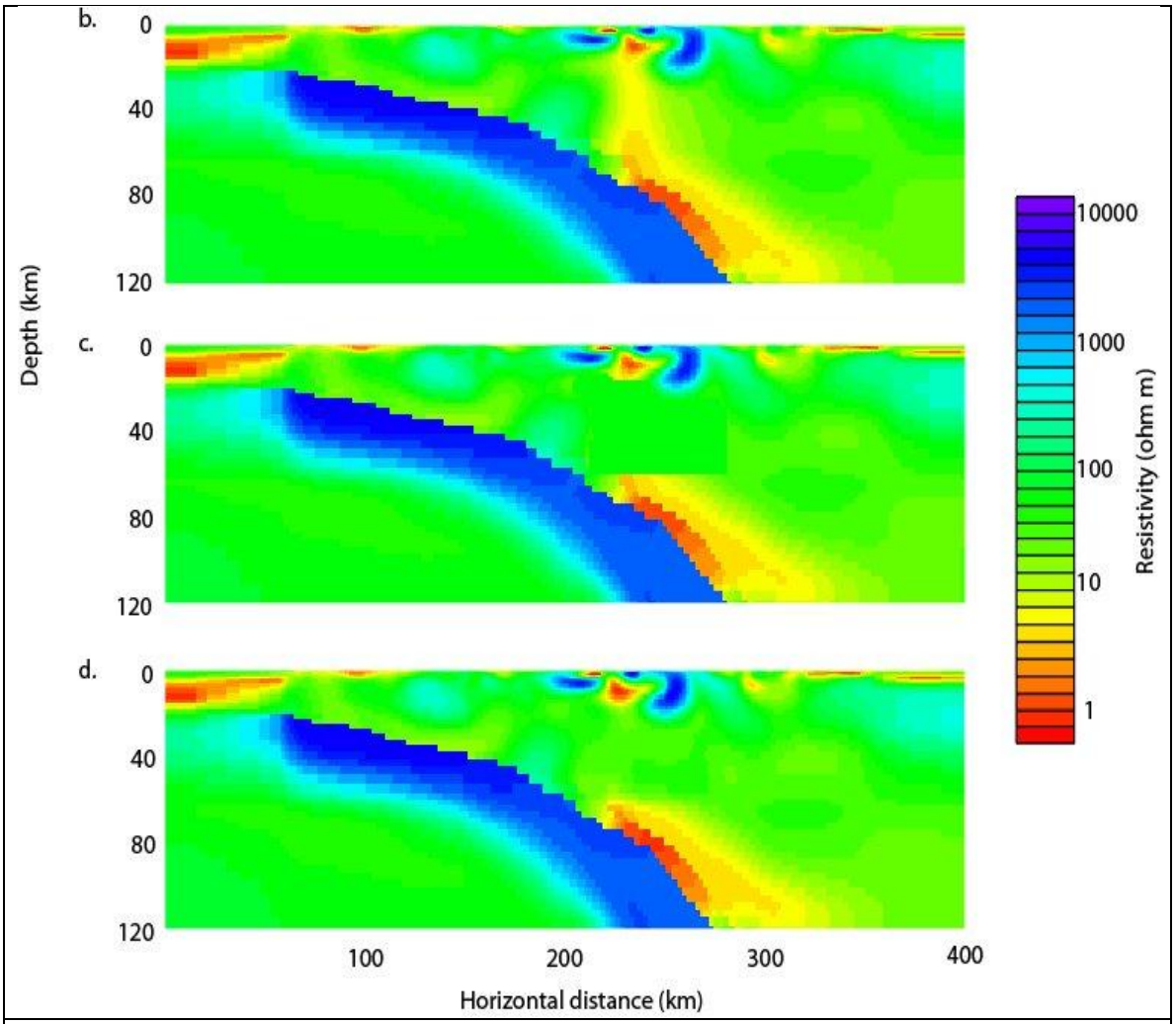

Figure 10: Sensitivity analysis is generally conducted on all of the primary features of the inversion models, as discussed in Chapters 3 and 4. This figure shows a typical example in which the robustness of the connecting corridor between the lower conductor associated with the slab and the upper conductor associated with Mt. Rainier. The primary augmented model from Chapter 4 is shown in figure 10a. In figure 10b, the vertical conductive corridor has been removed and replaced by a region with a conductivity of 100 Ωm. The inversion was restarted from this model, resulting in the model shown in figure 10c. It is clear that the conductive corridor is being regenerated in this model, suggesting that it is a robust feature.

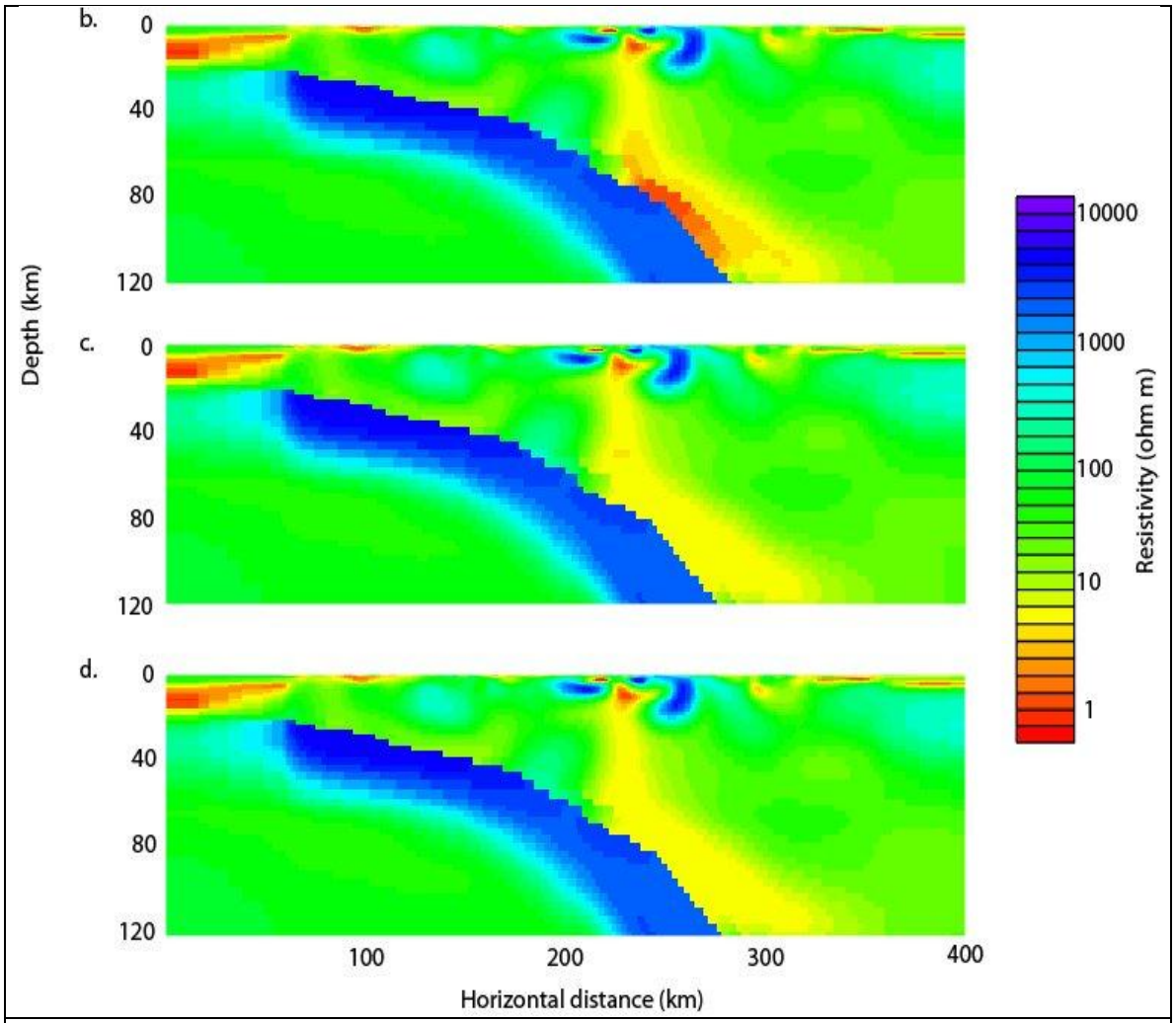

Figure 11: Another type of sensitivity analysis consists of varying the resistivity of a feature and evaluating the effect of the variations on misfit. This figure shows one of a series of tests conducted on the deep conductor in the augmented model to constrain its allowed conductivity. Figure 11a shows the primary augmented model from Chapter 4. Figure 11b shows the new starting model for which the minimum resistivity of the conductor is 10 Ωm. Figure 11c shows the inversion result: the inversion was able to better the original rms misfit value while the minimum resistivity of the conductor dropped to 8 Ωm. This series of sensitivity tests constrains the lowest resistivity of the conductor rising from the slab to be between 2 and 8 Ωm, with implications for its possible composition.

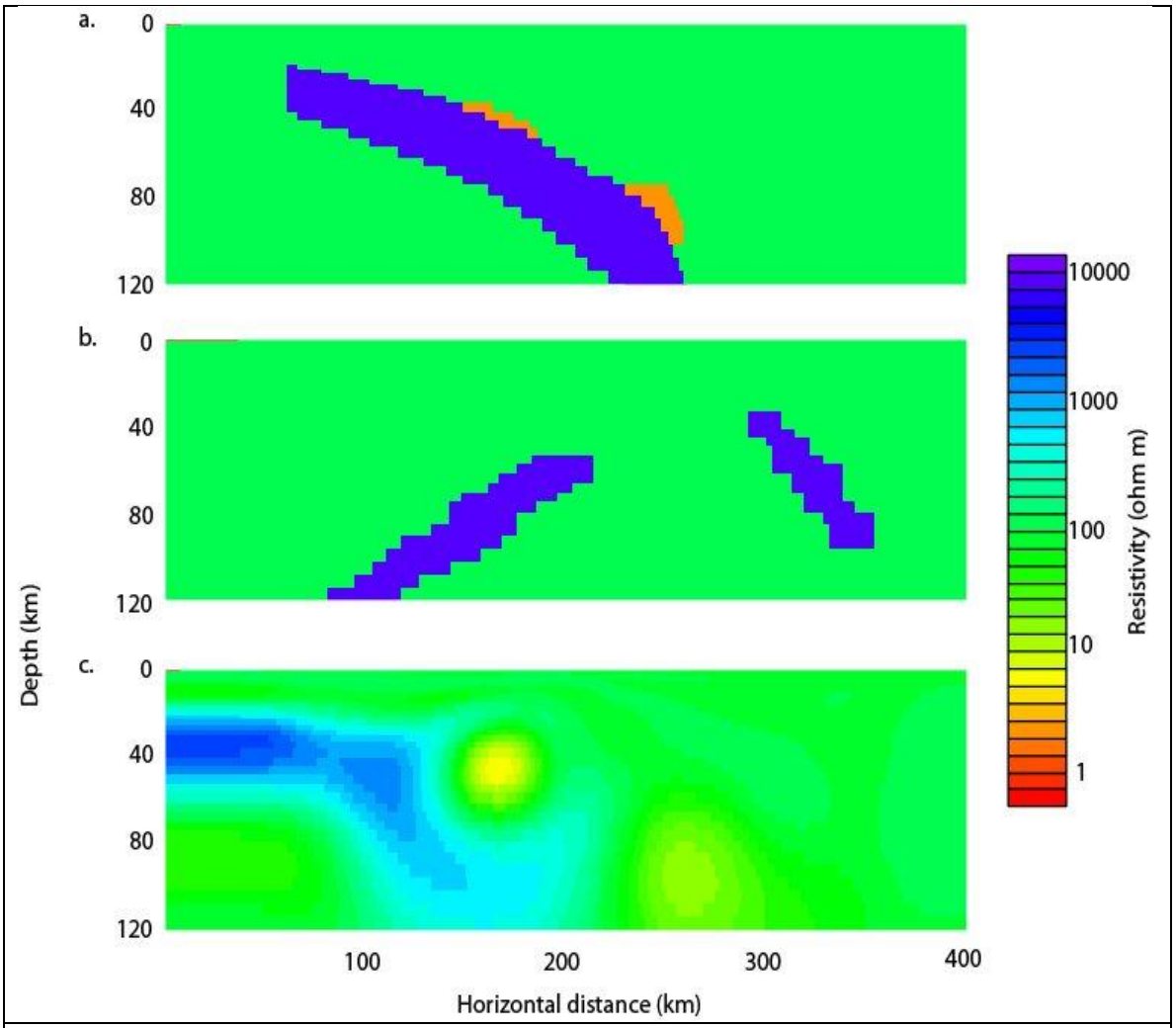

Figure 12: Part of the task of evaluating synthetic models is to investigate how incorrect assumptions can influence the results. Figure 12a shows the synthetic forward model from figure 2a in Chapter 4, where a dipping resistive (9000 Ωm) feature is in close proximity to two relatively thin conductors (3 Ωm). This model was used to generate a set of synthetic data. Figure 12b shows a starting model for an inversion series for which particularly poor assumptions were made regarding the location of the resistive feature. Figure 12c shows the inversion model generated from the poorly selected starting model. It is clear that the initial assumptions have been largely corrected by the inversion, an impression that is confirmed by comparing this model to the halfspace inversion model shown in figure 2c in Chapter 4.

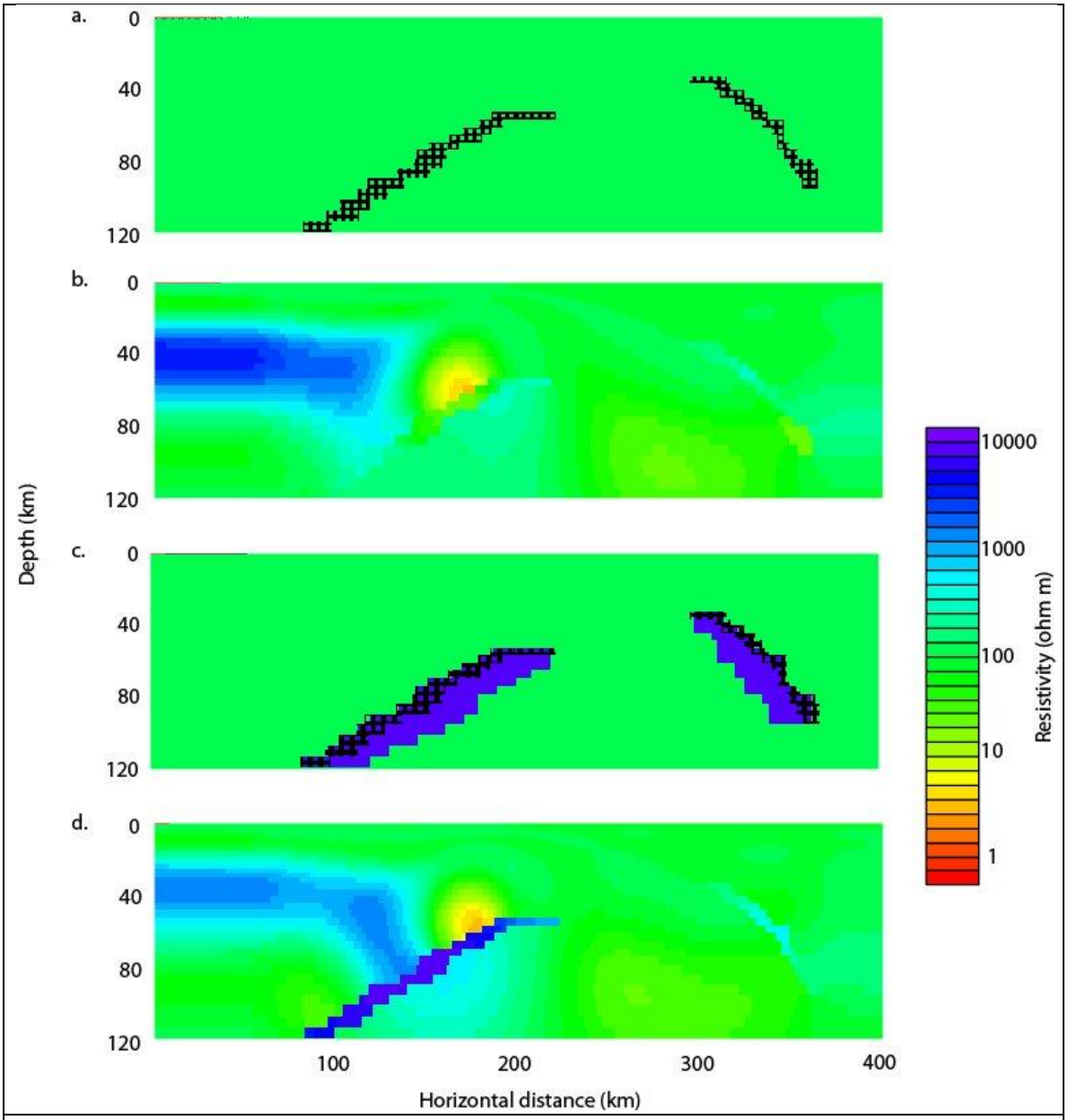

Figure 13: These models also use the synthetic data generated from the forward model in figure 12a, as well as the poor assumptions, but this time using tear zones. Figure 13a shows the starting model as a 100 Ωm half space with tear zones (but no resistive features). The inversion model associated with this starting model is shown in figure 13b. While the locations of the conductors are fairly accurately resolved, the interface between the shallow conductor and the resistive feature incorrectly follows the imposed tear zone. Figure 13c shows a starting model for which both the resistive features and their corresponding tear zones are included, and the associated inversion model is shown in figure 13d. In this case, the inversion model is reasonably accurate away from the tear zone, but retains the incorrect assumption implicit in the starting model within the tear zone. The eastern resistive feature is much less prominent in the inverted model, but still present as well. Figures 12 and 13 demonstrate the importance of using resistive features first without tears in order to evaluate the accuracy of the assumptions about location; this was a recurring theme in our analyses.

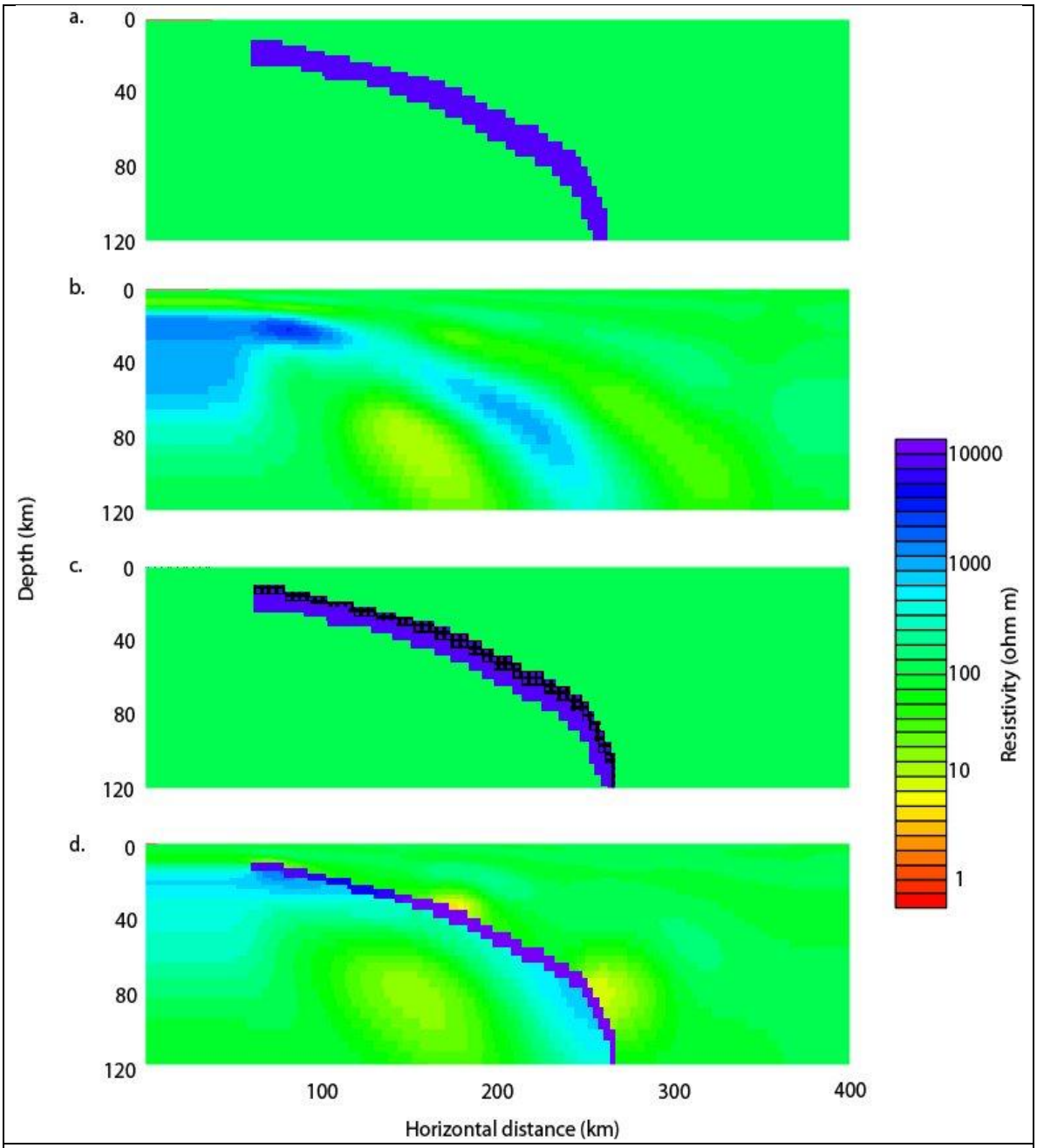

Figure 14: Figure 14 shows the impact of an assumption in which the top of the resistive dipping feature is placed approximately 10 km too high in the starting model (again based on synthetic data generated from the forward model in figure 12a). Figure 14a is the starting model showing the assumed location of the resistive feature. The associated inversion model in figure 14b does a nice job relocating the dipping resistor to its proper location, though for reasons explained in Chapter 4 does not constrain the conductors very well. Figure 14c shows a starting model with the same imposed resistive feature, but with the additional imposition of a tear zone along the top of the resistor. This causes the inversion (figure 14c) to incorrectly hold the resistor in the position of the tear.

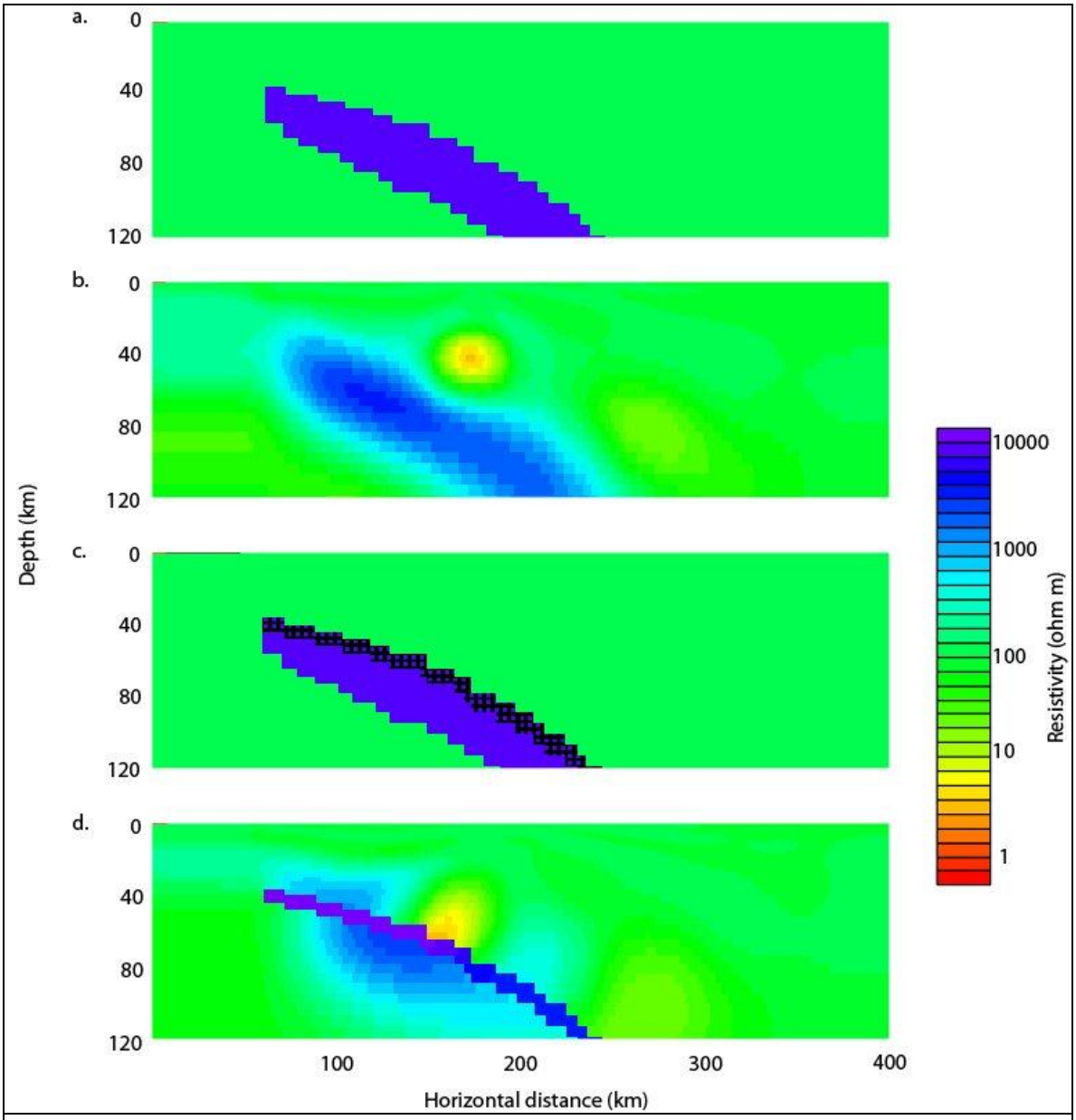

Figure 15: Figure 14 shows the impact of an assumption in which the top of the resistive dipping feature is placed approximately 10 km too low in the starting model (again based on synthetic data generated from the forward model in figure 12a). The inversion in figure 14b moves the resistive feature shallower, though it also exhibits "retreat" from the conductive feature as described in Chapter 4. The starting model in figure 14c includes an imposed tear zone, and the associated inverted model is shown in figure 14d. In this case, the resistive feature passes the tear zone boundary and extends upwards. These kinds of analyses show that examining starting models with combinations of imposed features and tear zones, we can determine with some confidence both the accuracy of our assumptions and the manner in which they might not be correct.